Development of a MR Hydraulic Bushing for Automotive Applications

by

Brad B. Schubert

A thesis
presented to the University of Waterloo
in fulfillment of the
thesis requirement for the degree of
Master of Applied Science
in
Mechanical Engineering

Waterloo, Ontario, Canada, 2005

I hereby declare that I am the sole author of this thesis. This is a true copy of the thesis, including any required final revisions, as accepted by my examiners.

I understand that my thesis may be made electronically available to the public.

Abstract

The purpose of this work is to design a semi-active magnetorheological (MR) hydraulic bushing. The semi-active bushing is intended to be used to isolate a cylinder deactivating engine. Cylinder deactivation causes high transient torsional loading in addition to changing the magnitude and mode of engine vibrations requiring an adaptive or controllable isolator.

Practical and simple semi-active control strategies are inspired by investigating the optimization of linear and slightly cubic nonlinear single degree of freedom isolators. Experimental verification of the optimization technique, which minimizes the root mean square (RMS) of engine acceleration frequency response and RMS of the force transmitted frequency response, shows that this method can be implemented on real linear systems to isolate the engine from harmonic inputs. This optimization technique is also applied to tune selected model parameters of existing two degree of freedom hydraulic bushings.

This thesis also details the development of a MR hydraulic bushing. The MR bushing design retrofits an existing bushing with a pressure driven flow mode valve on the inertia track. A new efficient valve design is selected and developed for the application. The MR hydraulic bushing is designed, mathematically modeled, and numerically simulated. The simulation results show that the MR bushing tends to increase the low frequency dynamic stiffness magnitude while simultaneously decreasing the phase. The next stage of the project is fabrication and testing of the semi-active bushing. The performance of the manufactured MR bushing is tested on a base excitation apparatus. Varying the current input to the MR valve was found to have a small effect on the response of the suspended mass. The results are in agreement with the effects demonstrated by the dynamic stiffness numerical simulation.

Acknowledgements

Firstly, I would like to acknowledge John Ulicny and Ping Lee of General Motors for their contributions to the project in the area of magnetorheological fluids and engine isolation technology.

A great deal of this research is inspired and made possible through the teamwork of past and present students of Dr. Farid Golnaraghi; and so, I would like to extend my thanks in no particular order to R. Alkhatib, A. Narimani, N. Eslaminasab, T. Gillespie, S. Arzanpour, and Y. Shen for their contributions to my experimental, theoretical and numerical work. In addition, I would like to thank my good friends and colleagues T. Arvajeh, R. Majlesi, O. Ansari, and A. Wolff for teaching about the graduate student lifestyle.

Special thanks to Robert Wagner for your hard work, design advice and for sharing machining know-how.

I would like to sincerely express my gratitude to Dr. Golnaraghi for providing me the opportunity and the freedom to apply engineering skills to explore and experiment with science, and most importantly giving me the chance to grow as an academic and an engineer.

Finally, thank you Kathryn, my beautiful wife, for your patience, understanding, encouragement, and your confidence in me. But most of all, thank you for your sacrifice – you know I'll make it up to you!

Dedication

For Mom and Dad, whom I can attribute all my success and happiness in life.

Table of Contents

Abstract iii
Acknowledgements iv
Dedication v
Table of Contents vi
List of Figures viii
List of Tables xiii
Nomenclature xiv
Chapter 1 Introduction 1
1.1 Root Mean Square Frequency Domain Optimization 2
1.2 Isolating Cylinder-on-Demand Engines 3
1.3 A New Solution: Semi-Active Isolators 5
1.4 Thesis Overview 7
Chapter 2 Literature Review 9
2.1 Optimization of Isolators 9
2.1.1 Linear Mount Optimization 10
2.1.2 Nonlinear Optimization 17
2.2 Engine Isolators 21
2.2.1 Hydraulic Mounts and Bushings 21
2.2.2 Semi-active Engine Isolators 24
2.3 Summary 28
Chapter 3 Model Development and Optimization 29
3.1 Forced Linear Isolator Optimization 29
3.1.1 Harmonic Forcing Excitation 32
3.1.2 Rotating Unbalance Excitation 36
3.1.3 Linear Optimization Summary 39
3.2 Force Nonlinear Isolator Optimization 41
3.2.1 Unforced Time Domain Solution of Cubic Nonlinear Isolator 41
3.2.2 Forced Solution of Cubic Nonlinear Isolator 45
3.2.3 RMS Optimization of the Cubic Nonlinear System 48
3.3 MR Hydraulic Bushing Modeling 52
3.3.1 MR Bushing Design 52
3.3.2 MR Bushing Dynamic Modeling 58

3.3.3 RMS Optimization of the Passive Bushing Parameters 62
3.3.4 MR Bushing Simulation 68
3.4 Summary 75
Chapter 4 Experiment Implementation 77
4.1 Linear RMS Optimization Experiment 77
4.2 Hydraulic Bushing Experiment 83
4.2.1 MR Valve Implementation 83
4.2.2 Fixture design 85
4.2.3 Sensors and Excitation 87
4.2.4 Experiment Issues 89
4.3 Summary 93
Chapter 5 Experimental Results and Evaluation 94
5.1 Linear RMS Optimization Experiments 94
5.1.1 RMS Optimization of the Base Excited Isolator 94
5.1.2 RMS Optimization of the Unbalance Excited Isolator 98
5.1.3 RMS Optimization of the Harmonic Force Excited Isolator 98
5.2 MR Hydraulic Bushing Experiment 101
5.2.1 Verification of Bushing Model Parameter Values 101
5.2.2 Dry MR Hydraulic Bushing Experiments 105
5.2.3 MR Hydraulic Bushing Experiments 108
5.3 Summary 114
Chapter 6 Conclusions and Future Work 115
6.1 RMS Optimization 115
6.2 MR Bushing 117
Bibliography 120

List of Figures

Figure 1-1: Photograph of a hydraulic engine bushing 5
Figure 2-1: Schematic of a linear 1 DoF isolator representing an engine mount. 10
Figure 2-2: The frequency response functions of the base excitation linear passive absorber. 12
Figure 2-3: The *R* versus η map illustrating the line of optimum design for a base excited linear passive vibration isolator (Jazar *et al.*, 2003). 14
Figure 2-4: The simulated relative displacement time response to a sine square bump input, for three systems identified in Figure 2-3 (Jazar *et al*., 2003). 16
Figure 2-5: The simulated transmitted force time response to a sine square bump input, for three systems shown in Figure 2-3 (Jazar *et al.*, 2003). 16
Figure 2-6: Base excitation response of non-dimensional amplitude illustrating the jump. 19
Figure 2-7: RMS patch illustrating the effect of varying nonlinear cubic stiffness and damping in a base excited system. Nominal linear system parameter values: ω_n = 10 Hz, ζ = 0.4. 20
Figure 2-8: RMS patch illustrating the effect of varying nonlinear cubic stiffness and damping in an base excited system relative to varying the linear system parameters (Narimani & Golnaraghi 2004). Nominal linear system parameter values: ω_n = 10 Hz, ζ = 0.4. 21
Figure 2-9: Typical hydraulic mount including the decoupler (Geisberger, 2000). 22
Figure 2-10: Mechanical model of a base/unbalance excited hydraulic bushing. 23
Figure 2-11: Illustration of a MR device consisting of an annular channel of pressure driven flow passing through the perpendicular magnetic field it two locations. (green – MRF, orange – magnetic coil) 26
Figure 2-12: Schematic of the valve presented in Gorodkin *et al*. (1998) and Kordonski *et al*. (1995) illustrating the two radial channels of pressure driven flow passing through the perpendicular magnetic field. (green – MRF, orange – magnetic coil) 27
Figure 2-13: Mechanical model of the hydraulic bushing presented by Ahn *et al*. (1999) and Ahmadian and Ahn (1999). 27
Figure 3-1: Illustration of the various simplified forms of isolator inputs. 30
Figure 3-2: Normalized amplitude with respect to static displacement under a harmonic force. 31
Figure 3-3: The RMS force transmissibility given a harmonic force input for a linear vibration isolator versus the damping ratio for various natural frequencies. 33
Figure 3-4: The RMS force transmissibility given a harmonic force input for a linear vibration isolator versus the natural frequency for various damping ratios. 33

Figure 3-5: The RMS absolute displacement given a harmonic force input for a linear vibration isolator versus damping ratio for various natural frequencies. 34
Figure 3-6: The RMS absolute displacement given a harmonic force input for a linear vibration absorber versus the natural frequency for various damping ratios. 35
Figure 3-7: The RMS force transmissibility versus the RMS absolute displacement illustrating the line of optimum design for a harmonic forced linear passive vibration isolator. 35
Figure 3-8: The RMS force transmitted given a rotating unbalance for a linear vibration isolator versus the damping ratio for various natural frequencies. 36
Figure 3-9: The RMS force transmitted given a rotating unbalance for a linear vibration isolator versus the natural frequency for various damping ratios. 37
Figure 3-10: The RMS absolute displacement given a rotating unbalance for a linear vibration isolator versus damping ratio for various natural frequencies. 37
Figure 3-11: The RMS absolute displacement given a rotating unbalance for a linear vibration absorber versus the natural frequency for various damping ratios. 38
Figure 3-12: The RMS force transmitted versus the RMS absolute displacement illustrating the line of optimum design for a rotating unbalance linear passive vibration isolator. 38
Figure 3-13: Illustrative summary of the various inputs and their corresponding RMS domain optimization design curves. 40
Figure 3-14: The line of optimum design for the base, rotating unbalance and harmonic forced excited linear passive vibration isolator in the $\zeta - f_n$ plane. 40
Figure 3-15: Amplitude versus time relative to the actual numerical simulation of the nonlinear system for various initial conditions. 44
Figure 3-16: Amplitude of the time domain solution of the cubic nonlinear system for various initial conditions illustrating the unstable limit cycle of the negative cubic damping system. 45
Figure 3-17: RMS patch illustrating the effect of varying nonlinear cubic stiffness and damping in an unbalance forced system. 49
Figure 3-18: RMS patch illustrating the effect of varying nonlinear cubic stiffness and damping in an unbalance forced system. 49
Figure 3-19: Effects of varying linear parameters on the dimensionless response to a step input. 51
Figure 3-20: MR valve schematic illustrating the radial fluid channels (green) as well as the flux path (blue), the coil (orange), core material (grey) and non-flux conducting material (brown). 52
Figure 3-21: Magnetic properties of 1020 steel. 53
Figure 3-22: Radial channel of MR fluid through the valve. 54
Figure 3-23: Magnetic properties of GM Corp. formulated MRF 13MAG098. 56

Figure 3-24: Valve gain K_{MR} versus input current I. 58
Figure 3-25: Dynamic stiffness of hydraulic bushing P/N 90576090 for 0.1 and 2.0 mm inputs (peak to peak). (solid – simulation, dotted – experimental) 60
Figure 3-26: Base excitation RMS optimization of the inertia track parameters (solid – constant d_h; dotted – constant l; circles - nominal mount and tuned inertia track, as indicated)..... 63
Figure 3-27: Harmonic forced RMS optimization of the inertia track parameters (solid – constant d_h, dotted – constant l, circle - nominal mount). 64
Figure 3-28: Dynamic stiffness given a 20% decrease in inertia track length. 64
Figure 3-29: Reduction in transferred force given a 20% decrease in inertia track length. 65
Figure 3-30: Increase in displacement given a 20% decrease in inertia track length. 65
Figure 3-31: Base excitation RMS optimization of the pumping chamber parameters (solid – constant C_1, dotted – constant A_p, circle - nominal mount). 67
Figure 3-32: Harmonic forced RMS optimization of the pumping chamber parameters (solid – constant C_1, dotted – constant A_p, circle - nominal mount). 68
Figure 3-33: Prototype MR bushing simulation and purchased bushing filled with MRF simulation compared to the purchase bushing experimentally measured dynamic stiffness. 70
Figure 3-34: Simulation time domain response of the chamber pressures, inertia track flow rate and hydraulic pressure drop versus the MR effect (dotted line in the top axes) for I = 0.1 A, Z = 1 mm (2 mm peak to peak). 71
Figure 3-35: Simulation time domain response of the chamber pressures, inertia track flow rate and hydraulic pressure drop versus the MR effect (dotted line in the top axes) for I = 0.4 A, Z = 1 mm (2 mm peak to peak). 72
Figure 3-36: MR Bushing dynamic stiffness simulation results for various current inputs and Z = 1 mm (2 mm peak to peak). 73
Figure 3-37: Effect of changing fluid inertia and compliance on the bushing dynamic stiffness. 74
Figure 3-38: Effect of increasing compliance the forced response. 75
Figure 4-1: Single degree of freedom isolator experiment apparatus mounted on the LDS V722 shaker..... 78
Figure 4-2: An inertial force can be applied to the suspended mass by accelerating the reference frame attached to the base of the isolator. 79
Figure 4-3: Friction causing jump phenomena during low energy frequency responses. 81
Figure 4-4: Piecewise nonlinearity as the dashpot reaches maximum displacement under high damping ratios 81

Figure 4-5: Preliminary results illustrating nearly linear experimental base excitation frequency responses. 82
Figure 4-6: Hydraulic bushing casing to house the rubber purchased mount, with ports to allow bypassing the inertia track and of pressure measurement (top left). Illustration of the various ports and chamber of the bushing and casing (top right), where the red curve represents the original inertia track. Exploded view of the bushing and casing (bottom). 84
Figure 4-7: Prototype MR valve exploded view (brown – 1020 steel core material, grey – 6061 aluminum). 85
Figure 4-8: Illustration of the setup to measure dynamic stiffness. 86
Figure 4-9: Dynamic stiffness fixture and bushing mounted on the LDS V722 shaker. 86
Figure 4-10: Illustration of the setup to measure transmissibility via a base excitation experiment. 87
Figure 4-11: Solid model of the base excitation setup mounted on the shaker. 88
Figure 4-12: The MR valve set up used to conduct base excitation experiments 88
Figure 4-13: Variation of relative displacement despite constant amplitude input during a dynamic stiffness test. 90
Figure 4-14: Variation of transferred force with peaks corresponding to the peaks in relative displacement during a dynamic stiffness test. 90
Figure 4-15: Modal analysis results illustrating the first mode of vibration of the shaker frame at approximately 19 Hz. 91
Figure 4-16: Modal analysis results illustrating the second mode of vibration of the shaker frame at approximately 47 Hz. 91
Figure 4-17: Initial hydraulic bushing acceleration results given base excitation input. Two main modes of vibration are present: linear mode (19 Hz) and a rotational mode (26 Hz) identified by the high edge acceleration with respect to the acceleration of the centre of mass. 92
Figure 4-18: Illustration of the undesirable rotational mode of vibration. 92
Figure 5-1: Base excitation frequency response (experiment – solid line, simulation – dotted line)... 95
Figure 5-2: Base excitation experiment RMS results compared to theoretical results. 97
Figure 5-3: Experiment base excitation results illustrated on the linear RMS optimization graph. Note that the experiment RMS values are computed from 5 to 20 Hz. 97
Figure 5-4: Forced frequency response (experiment– solid line, simulation – dotted line). 99
Figure 5-5: Experimental RMS Results compared to linear results. 100
Figure 5-6: Experiment harmonic forced results illustrated on the linear RMS optimization graph. Note that the experiment RMS values are computed from 5 to 20 Hz. 100
Figure 5-7: Photograph of the hydraulic bushing P/N 90575028 (similar to 90576090). 101

Figure 5-8: Response of the rubber and hydraulic bushing P/N 90575028 (*m = 19.3 kg)*. 103
Figure 5-9: Hydraulic bushing simulation illustrating the change in the response of the two degrees of freedom as the suspended mass increases to 80 kg. 104
Figure 5-10: Dynamic stiffness of bushing P/N 90576090 (preload 1050 N) and bushing P/N 90575028 (preload 1175 N) measured in the University of Waterloo laboratory. 104
Figure 5-11: Dry engine mount base excitation with a 19.3 kg suspended mass. 105
Figure 5-12: Base excitation of the dry engine mount with a 31 kg suspended mass. Base amplitudes are varied from 0.6 mm to 0.9. 106
Figure 5-13: Force transmissibility with respect to base acceleration for the dry mount with a 31 kg suspended mass. Experiments are conducted for base amplitudes from 0.4 to 1.8 mm peak to peak. (dashed - backward sweep, solid - forward sweep) 107
Figure 5-14: Original MR bushing base excitation ($|Y| = 0.4$ mm) results generated with the 19.3 kg mass and using the roller bearings (top – mass acceleration, bottom – relative displacement) . 109
Figure 5-15: MR bushing base excitation relative displacement results generated with the 31.3 kg mass and using the brass bearings (solid – forward sweep, dotted – backward sweep). 111
Figure 5-16: MR bushing base excitation mass acceleration results generated with the 31.3 kg mass and using the brass bearings (solid – forward sweep, dotted – backward sweep). 112
Figure 5-17: MR bushing base excitation transferred force results generated with the 31.3 kg mass and using the brass bearings (solid – forward sweep, dotted – backward sweep). 113
Figure 6-1: Increase of the off-state notch frequency to improve the bandwidth of the MR bushing 117
Figure 6-2: Potential implementation of MR valve in a production hydraulic bushing. 118

List of Tables

Table 3-1: Dimensionless peak step response data describing the effect of varying the nonlinear stiffness and damping. 50
Table 3-2: Dimensionless peak pulse response data describing the effect of varying the cubic nonlinear stiffness and damping. 51
Table 3-3: Properties of GM Corp. formulated MRF 13MAG098. 57
Table 3-4: MR valve design parameters. 57
Table 3-5: Simulation MR valve dynamic stiffness pole and zero properties. 69
Table 5-1: Base excitation test parameters and observations. 94
Table 5-2: Forced excitation test parameters and observations. 99

Nomenclature

$a = \left\| \ddot{X} / Y \right\|$	acceleration with respect to base excitation amplitude [1/s]
A_i	inertia track cross-sectional area [m^2]
A_f	pole real area
A'_f	magnetic pole effective area
A_p	effective pumping area [m^2]
B_r	rubber linear damping [N-s/m]
c	linear damping coefficient [N-s/m]
$C = 1/C_1 + 1/C_2$	lumped compliance [N/mm^5]
$C_1,\ C_2$	lower and upper chamber compliance, respectively [mm^5/N]
c_{MR}	constant of magnitude 2-3 depending on the controllability
d_h	inertia track hydraulic diameter
D_i	inner diameter of the MR valve coil
D_o	outer diameter of the MR valve coil
e	eccentricity of unbalance mass [m]
$f_n = \omega_n / 2\pi$	natural frequency [Hz]
f_o	harmonic force excitation amplitude per unit mass [N/kg]
$F(t)$	engine dynamic loading [N]
F_T	transmitted force [N]
FT	transmitted force per unit mass [N/kg]
g	height of the MR valve fluid channel
H_f	field intensity [At/m]
I	MR valve input current [A]
$i = \sqrt{-1}$	imaginary unit
k	linear stiffness coefficient [N/m]
K_r	rubber linear stiffness [N/m]
K_{MR}	MR valve gain [Pa/A]
l	total length of the of the MR valve fluid path in the flux (inertia track)
L	inertia track fluid inductance [$Pa\text{-}s^2/m^3$]
L_c	the length of the coil
L_i	inductance of the MR valve coil [H]
MR	magnetorheological
MRF	magnetorheological fluid
m	mass of engine [kg]
m_o	engine unbalance mass [kg]
N	number of wire turns in a magnetic coil
OPM	magnet wire resistance per unit length [Ω /m]
$P_1,\ P_2$	upper and lower chamber pressures [Pa]
Q	inertia track flowrate
Q_{in}	flow from pumping chamber to the MR valve
Q_{out}	flow from MR valve to the compliance chamber
$r = \omega/\omega_n$	excitation frequency ratio

R	base excitation RMS absolute acceleration
R_e	electrical resistance of the MR valve coil [Ω]
R_{eq}	equivalent flux resistance [At/Wb]
R_f	hydraulic resistance to flow [Pa-s/m^3]
t	MR valve wall thickness
V_{in}	input voltage [V]
w	width of the MR valve fluid channel
WPA	coil wires per square metre
x	engine (mass) displacement [m]
X	displacement amplitude [m]
X_{st}	static displacement amplitude due to step loading [m]
y	chassis or base displacement [m]
Y	base harmonic displacement excitation amplitude [m]
$z = x - y$	mass-base relative displacement [m]
Z	relative displacement amplitude [m]
z^*	perturbation solution non-dimensional displacement
$\zeta = c/2\sqrt{km}$	linear damping ratio
Δp_μ	viscous fluid pressure drop
Δp_τ	pressure drop due to MRF yielding
η	base excitation RMS relative displacement
κ	MR valve controllability ratio
$\kappa_1,\ \kappa_2$	length and hydraulic diameter scaling parameters, respectively
$\beta_1,\ \beta_2$	pumping area and compliance scaling parameters, respectively
$\lambda = \lvert (X - Y)/Y \rvert$	relative displacement transmissibility
λ_e	base excitation eigenvalue
γ	harmonic force excitation RMS displacement [(m-kg/N)^2]
ϕ	harmonic force excitation RMS force transmissibility
μ_f	MRF viscosity [Pa-s]
μ_{core}	magnetic permeability of the MR valve core material [H/m]
μ_{MR}	magnetic permeability of the MRF [H/m]
ω	frequency of oscillation [rad/s]
$\omega_1,\ \omega_2$	base excitation modes of vibration [rad/s]
ω_{dr}	forcing input frequency of oscillation [rad/s]
$\omega_n = \sqrt{k/m}$	natural frequency [rad/s]
ρ	cubic stiffness coefficient
ρ_f	MRF density
τ_e	rise time of the MR valve coil [s]
τ_y	MRF yield stress as a function of the field intensity
ξ	cubic damping coefficient
$\Phi = \lvert F_T/F \rvert$	harmonic force excitation force transmissibility
$\Lambda = \lvert X/f_o \rvert$	harmonic force excitation displacement with respect to input force [m-kg/N]

$\psi = \left\| F_T \middle/ m_o e \omega_n{}^2 \right\|$	unbalance excitation non-dimensional force transmitted
$\Omega = \left\| Xm \middle/ m_o e \right\|$	unbalance excitation non-dimensional displacement
χ	unbalance excitation RMS non-dimensional force transmitted
Γ	unbalance excitation RMS non-dimensional displacement
φ	magnetic flux [Wb]

Chapter 1
Introduction

In the automotive industry, there is a natural demand from the customer to decrease cost of the vehicle, while increasing comfort and fuel economy. These are usually highly conflicting design criteria, which are generally satisfied by decreasing the amount of material used to create the system, and thus decreasing the mass of the vehicle and replacing it with improved and sophisticated technology as the cost of this technology decreases.

An example of this on the forefront of automotive engineering is the advent of drive-by-wire technology. Steering-by-wire is becoming a reality in automobiles with the intent to replace the mechanical linkage between the steering wheel and the tire as well as the power steering system with a lightweight, efficient electromechanical system. Many decades ago, a similar fly-by-wire design was implemented in the aerospace industry initially on fighter jets (and the NASA space shuttles) where previously mechanical and hydro-mechanical systems were used to control aeroplanes, likely for a price higher than what most people would pay for an entire automobile.

One of the characteristics of vehicles that define their quality is the amount of noise, vibration and harshness (NVH) in the cabin. Muller, Weltin, Law, Roberts, and Siebler (1994) note that decreasing the mass of vehicles represents the ability for energy sources to more easily transfer through the structur; hence, increased NVH is the cost in comfort associated with an increase in fuel economy and decrease in price of the automobile.

An automobile engine, body and chassis system is susceptible to undesired vibrations due two sources of excitation: inherent unbalance and periodic combustion forces in the reciprocating engine as well as disturbances transmitted through the vehicle's suspension system from the road. The frequency range of these vibrations is typically in the range of 1-200 Hz (Jazar & Golnaraghi, 2002).

Engine mounts are vibration isolators which are used to minimize the effect of the disturbances described above on the system. In general, it is desirable to restrain the relative motion of the engine to satisfy mechanical constraints while minimizing the force transmitted to and from the engine itself (Singh, Kim, Ravindra, 1992). Minimizing the force transferred reduces the impact of the dynamics of the engine given a base (chassis or body) excitation source, thus improving ride and minimizing potentially damaging inertia forces on the engine. Moreover, minimizing transfer of unbalance forces through the engine to the chassis reduces cabin noise and thus improves rider comfort.

For several decades now, NVH has benefited from the implementation of hydraulic mounts (Flower, 1985). Hydraulic bushings, a variation of a hydraulic mount, are currently widely used in industry; however, the development of cost effective semi-active or active isolation solutions is the next frontier. Moreover, the introduction of cylinder-on-demand technology has intensified the pursuit of a controllable isolator due to the affect it has on engine vibration isolation.

The goal of this thesis is to investigate the optimization of isolators to comply with the transferred force criteria and displacement constraint with the intent to apply this optimization to the design of semi-active isolators. The semi-active bushing is to be designed to isolate a cylinder-on-demand engine.

1.1 Root Mean Square Frequency Domain Optimization

As mentioned above, engine isolators must be designed with the intent to minimise the force transferred through the mount, while maintaining the amplitude of vibration within a fixed range. The problem is: how can these criteria and constraints be met? Is there a relationship between them?

These questions have been partially answered by studying the root mean square (RMS) of the absolute acceleration and the relative displacement frequency responses of a single degree of freedom (DoF) isolator (Jazar, Narimani, Golnaraghi, & Swanson, 2003). It was concluded that a set of

optimal parameters could be found for a harmonic base excitation using a simple RMS cost function, to be detailed in Chapter 2 of this thesis.

Furthermore, Narimani and Golnaraghi (2004) present an optimal linear system and added slight nonlinearity to the stiffness and damping. These nonlinear parameters were again optimized in a similar manner to that applied to the linear system by Jazar *et al*. (2003) for a base excitation input.

One of the goals of this thesis is to build on the frequency domain optimization work on linear engine mounts presented by Jazar *et al*. (2003) as well as the nonlinear work presented by Narimani and Golnaraghi (2004). This extension of their work will include studies for different inputs as well as an examination of the change in the transient response when small amounts of nonlinear stiffness and damping are present.

An experiment will be conducted to verify the RMS optimization methods on a simple spring mass damper test bed. The purpose of this experiment is to verify that these optimization procedures can be applied to a real system. Inevitably, any real system will exhibit some degree of nonlinearity regardless of efforts to eliminate such complicating characteristics in the laboratory. Often, the degree of nonlinearity is so small that it is considered negligible; which, as this thesis will show, is a sound and practical assumption on the test bed used. It is also of interest to apply this optimization technique to the design of hydraulic bushings.

1.2 Isolating Cylinder-on-Demand Engines

The improvement of fuel economy has led automotive manufacturers to design engines which automatically switch between modes of operation. Each mode has a different number of cylinders firing depending on the requirements of the driver.

For example, when accelerating all six cylinders in a V6 engine should be firing to provide the maximum amount of power; however, once the target cruising speed is met and the load on the engine decreases the engine management unit (EMU) may take any given 3 cylinders out of the firing

sequence (Hardie *et al*., 2002). Jackson and Jones (1976) discovered over 25 years ago that this technique could save a quarter of the gas used in a V16 cylinder engine using 50% of the cylinders, also noting that they experience torsional vibrations when switching to 50% mode requiring a special torsional analysis. High energy savings are achievable largely due to the fact that steady state speed requires such a small amount of power (less than 30 HP) with respect to the maximum power of modern vehicles, as suggested by Ashely (2004), which can exceed 300 HP.

The change in the number of firing cylinders presents a unique vibration loading beyond the isolating capabilities of a regular hydraulic bushing (Figure 1-1). Although the mechanical unbalance vibrations occurring at the frequency of rotation of the crankshaft remain the same (first order vibrations), other orders are halved (with half of the cylinders deactivated). For example, the frequency of the combustion force produced by a four-stroke engine with *P* cylinders is as follows:

$$f_n = f_{crankshaft} n$$
$$f_n = N_{crankshaft} \left(\frac{1 \text{ min}}{60 \ s} \right) \left(\frac{1 \ cycle}{2 \ rev} \right) P \tag{1-1}$$

where the $N_{crankshaft}$ is the RPM of the crankshaft (or engine), f_n is the n^{th} order of vibration, n is the multiple of the crankshaft rotational frequency which is *P/2* in this case, and the cylinder fires once every two rotations of the crankshaft. Thus, for a 6 cylinder engine a 3^{rd} order torsional vibration is induced by the combustion and firing of the engine (Rao, 2004). When the system switches to 3 cylinders the torque produced by firing will occur at the 1.5^{th} order, as indicated by Matsuoka, Mikasa, Nemoto, and Gehm (2004).

As mentioned by Matsuoka *et al*. (2004), since the net produced crankshaft torque must be constant (to maintain the vehicle motion) between the two modes, the 3 cylinder combustion pressure must double since there are half as many cylinders; hence the piston forces which induce the torsional vibration double in magnitude. The result is that a suitable isolator should be half as stiff in the

operating frequency range of the 3 cylinder mode of the engine. This is likely around 1000-2200 RPM ($f_{1.5} = 25 - 55Hz$). The isolator must also maintain performance in 6 cylinder mode similar to current products.

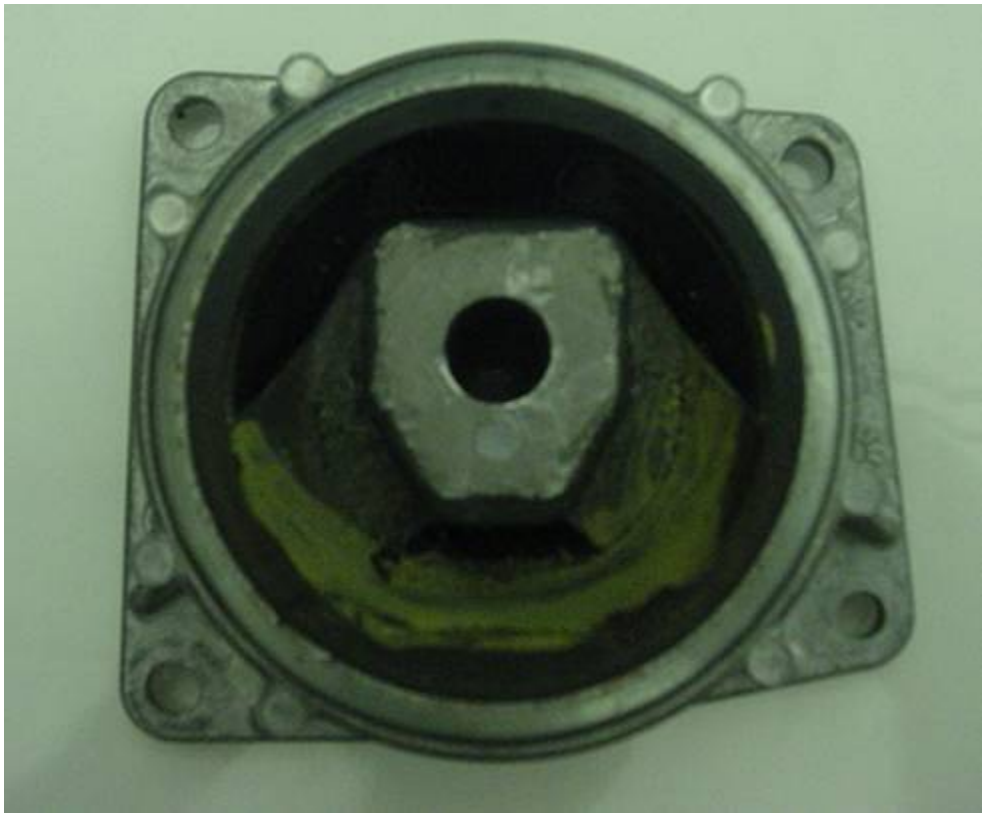

Figure 1-1: Photograph of a hydraulic engine bushing

1.3 A New Solution: Semi-Active Isolators

The true need for a new isolator spawns from the need to minimize fuel consumption which led to the implementation of cylinder-on-demand engines, also known as cylinder deactivation. Cylinder-on-demand produces changing load conditions, making it far too difficult to maintain the NVH performance of the vehicle with the current isolator design.

There are various mechanisms to influence the force produced by an isolator, in particular a hydraulic engine mount. For every mechanism, there are several proposed designs for active and semi-active mounts: Muller (1994); Kim and Singh (1995); Foumani, Khajepour, and Durali (2004);

Vahdati and Ahmadian (2003); Lee and Lee (2002), Matsuoka *et al*. (2004); and Jazar and Golnaraghi (2003). With the exception of the design proposed by Matsuoka *et al*. (2004), which is scheduled to be on the 2005 Honda Odyssey, none of the previous designs have been witnessed by the author to be implemented for the automotive market.

Producing a reliable active mounts is difficult since it requires an actuator, adequate sealing, moving parts, and possibly large amounts of energy for the actuator among other design issues. Similarly, semi-active isolators often require an actuator and moving parts; essentially having all the poor traits of an active mount with limited incremental performance. By comparison, magnetorheological (MR) semi-active systems represent a low cost, low energy consumption, and potentially very effective isolation solution with no moving parts.

It is the goal of this work is to develop a simple model of a hydraulic bushing, assuming that the nonlinearity in engine mounts can be attributed mostly to fluid damping, and simulate the response of the bushing to evaluate the performance in the frequency domain. The dynamic stiffness of current production bushings, supplied by General Motors Corporation (GMC), will be used to verify the mathematical model. This bushing will be used as a foundation to develop a semi-active MR bushing to isolate the cylinder deactivating engine vibrations on a GMC V6 vehicle platform. As will be discussed in greater detail in the following chapters, the MR bushing design will implement the flow mode (or valve mode) effect of MR fluids – a similar design which has led to the success of Lord Corporation's MR damper RD-1005.

The bushing design will be fabricated and tested. The industry standard for illustrating the performance of engine isolators is a plot of dynamic stiffness in the frequency domain. This data requires a specific test bed. From an isolation point of view, the performance of the mount is best measured by examining the transmissibility of displacement, velocity, and acceleration for given inputs to the isolator. For this reason, a base excitation experiment will also be conducted. This type

of experiment is rarely conducted and documented in the field and is considered by the author to be an improvement on the prior art.

1.4 Thesis Overview

In the previous sections, the need for semi-active engine bushings was presented. The objective of this thesis is to reduce the vibrations induced in a cylinder deactivating engine by using a MR bushing. The strategy for designing this bushing is to implement RMS optimization techniques to select appropriate parameters for the system and shed light on simple and practical control strategies to be further developed in future work.

In Chapter 2, a review of the prior work on RMS optimization is presented. This review of the literature covers both isolation of base excitations using a linear Voigt rubber model and isolators with slightly nonlinear elements. The advantage of adding nonlinearity via semi-active control is illustrated. Chapter 2 also details current engine isolator designs including a review of literature pertaining to controllable devices and how MR technology can be applied.

The core theoretical portion of the thesis follows Chapter 2. The linear and nonlinear RMS studies introduced in Chapter 2 are extended to various inputs in Chapter 3. This work provides the foundation for semi-active control strategies.

The prototype MR valve design is described in Chapter 3 and the input-output relationship of the valve is developed using numerical modeling. Dynamic equations of motion are developed for a MR bushing, similar to typical engine mount equations. This model is used to simulate the dynamic stiffness of the MR bushing.

Chapter 3 also applies the RMS optimization technique, which was originally used to optimize the parameters of the linear and nonlinear isolators, to hydraulic bushings. It is shown that this method can be used to improve the performance of hydraulic bushings.

Chapters 4 and 5 pertain to the experimental portion of the thesis. Chapter 4 describes the experimental apparatus used to verify the linear RMS optimization techniques, including the test bed used to conducts experiments on engine bushings. Chapter 5 discusses the results of the RMS and bushing experiments.

Finally, conclusion and recommendations for future work can be found in Chapter 6.

Chapter 2
Literature Review

2.1 Optimization of Isolators

As alluded to in the introduction, the fundamental requirement or function of an isolator is to minimize the force transmitted and maintain the relative displacement of the mount. This is the nature of the rubber isolators, according to the Kelvin (Voigt) model of rubber (otherwise referred to as a linear isolator, as illustrated in Figure 2-1), in that they can only produce force in response to changes in relative displacement and relative velocity.

The idea of designing a passive linear isolator which could both minimize the force transmitted and simultaneously minimize the relative displacement is unrealistic. Providing passive isolation from force cannot be achieved without the cost of deflection (Andrews, 2002).

The art of optimization can be taken to any level. Modern computing power permits optimization on an unimaginable computational scale. Lin, Luo, and Zhang (1990) developed an optimization strategy for an n-degree of freedom (DoF) system. Their method uses a relatively complex cost function and produces good response results at the cost of being computationally intensive and highly sophisticated.

Madjlesi, Schubert, Khajepour, and Ismail (2003) present another sophisticated optimization method whereby the optimum mount stiffness is derived by experimentally determining the frequency response functions (FRFs) which describe the noise transfer paths through the engine mounts to objective points in the cabin. Steady-state engine mount optimization is conducted by tweaking the frequency response of the mount and minimizing the objective point outputs using experimentally obtained engine loading and the FRFs. This method is very effective; however, it too is computationally intensive, sophisticated, and most importantly the result of optimisation may not be

manufacturable due to the limits of the isolator material properties and mechanical design constraints. A more detailed review of optimization literature is included in the work of Narimani (2004).

The RMS optimization method presented by Jazar *et al*. (2003) uses a very practical and mechanically intuitive cost function, has a closed form solution, and is extremely simple. This method is the basis for a large portion of the work in this thesis, and will be detailed in the following section.

2.1.1 Linear Mount Optimization

Traditionally, the fundamental vibration isolation problem is approached by separating the system from the source of vibration with a linear spring and damper, as illustrated in Figure 2-1.

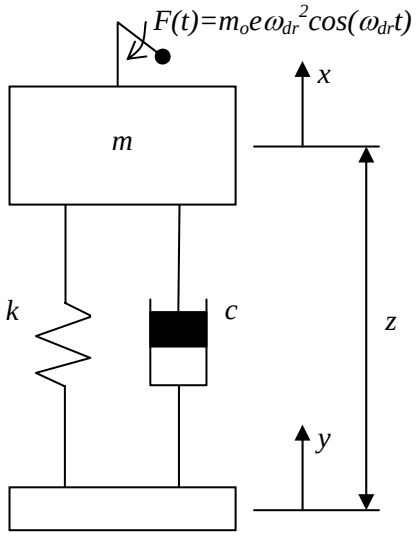

Figure 2-1: Schematic of a linear 1 DoF isolator representing an engine mount.

Reviewing the work presented by Jazar *et al*. (2003), the equation of motion of the above system is

$$m\ddot{x} + c(\dot{x} - \dot{y}) + k(x - y) = m_o e \omega_{dr} \cos(\omega_{dr} t) \tag{2-1}$$

where m is the total suspended mass [kg], c is the damping coefficient [N-s/m], k is the stiffness [N/m], m_o is an eccentric mass of eccentricity e [m] and driving frequency ω_{dr} [rad/s]. The displacement of the base and mass are y [m] and x [m], respectively. Equation (2-1) can be rearranged to the following form:

$$m\ddot{x} + c\dot{x} + kx = m_o e\omega_{dr}{}^2 \cos(\omega_{dr} t) + c\dot{y} + ky \tag{2-2}$$

The force transferred through the spring and damper, F_T [N], is

$$F_T(t) = m\ddot{x} - m_o e\omega_{dr}{}^2 \cos(\omega_{dr} t) = c(\dot{y} - \dot{x}) + k(y - x) \tag{2-3}$$

Thus, the design objectives can now be restated specifically in terms of the system parameters: the challenge is to find an optimal linear stiffness and damping, *k* and *c* respectively, which constrain the displacement of the mass *m*, measured by the coordinate *z* or *x* and which minimize the transferred force, $F_T(t)$, criteria due to the base excitation measured by the coordinate *y* or due to an input force generated by the engine, *F(t)*.

Considering the base excitation disturbance, equation (2-2) can be non-dimensionalized and rearranged to yield

$$\ddot{z} + 2\zeta\omega_n \dot{z} + \omega_n{}^2 z = -\ddot{y} \tag{2-4}$$

where the parameters in the above equation are damping ratio, natural frequency, and relative displacement denoted as follows, respectively:

$$\zeta = \frac{c}{2\sqrt{km}} \quad \omega_n = \sqrt{\frac{k}{m}} = 2\pi f_n \quad z(t)=x(t)-y(t) \tag{2-5}$$

Note that in the absence of a forcing input on the mass, the transferred force becomes

$$F_T(t) = m\ddot{x} = c(\dot{y} - \dot{x}) + k(y - x) \tag{2-6}$$

and thus is directly proportional to the absolute acceleration of the mass; hence if acceleration were to be minimized so too would the transferred force.

The steady state solution to equation (2-4) gives the transfer function of the system relating the absolute acceleration and relative displacement to the input are (where $r = \omega / \omega_n$)

$$a = \left|\frac{\ddot{X}}{Y}\right| = \frac{\omega^2\sqrt{1+(2\zeta r)^2}}{\sqrt{(1-r^2)^2+(2\zeta r)^2}} \tag{2-7}$$

and

$$\lambda = \left|\frac{X-Y}{Y}\right| = \frac{r^2}{\sqrt{(1-r^2)^2+(2\zeta r)^2}} \tag{2-8}$$

respectively, and are illustrated in Figure 2-2. Since it is preferable to minimize the amplitude of all of the transmissibility functions, Figure 2-2 illustrates the effect of the damping ratio and the cost of increased acceleration transmissibility as the frequency ratio $r > \sqrt{2}$ (Inman, 2001).

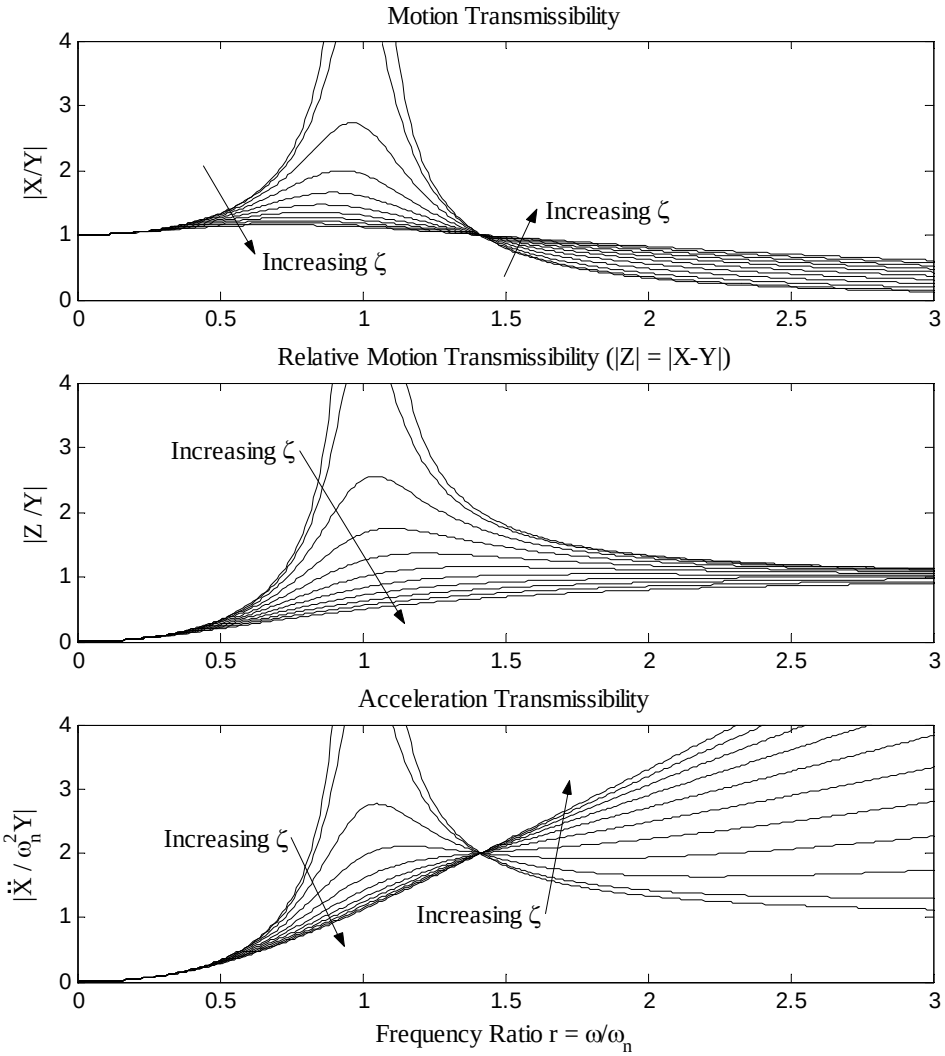

Figure 2-2: The frequency response functions of the base excitation linear passive absorber.

Optimum stiffness and damping ratio should be found by examining the response of the system in the frequency range of 0-20 Hz, a critical range for typical mechanical systems (Alkhatib, Jazar, & Golnaraghi, 2004). Given a certain damping ratio and stiffness, the performance of the system can be characterized by computing the RMS of the frequency response over a certain bandwidth. According to Inman (2001), RMS is a common method of representing a response in the field of vibration. In this case, it is representative of the variance of magnitude of relative motion or acceleration transmissibility – analogous to a weighted average amplitude.

The definition of the root mean square (RMS) of a function *h(ω)* from $\omega =$ 0-20 Hz is as follows

$$RMS(h(\omega)) = \sqrt{\frac{1}{40\pi}\int_0^{40\pi} h(\omega)^2 d\omega} \tag{2-9}$$

The above formulation is the foundation for the work of Jazar *et al*. (2003) and Narimani and Golnaraghi (2004). Applying equation (2-9) to the base excitation, we define

$$R = RMS(a)\text{, RMS absolute acceleration} \tag{2-10}$$

$$\eta = RMS(\lambda)\text{, RMS relative displacement} \tag{2-11}$$

Jazar *et al*. (2003) obtained a closed form relation for the local minimum RMS acceleration given by (2-12).

$$\frac{\partial}{\partial\zeta} R(\zeta, \omega_n) = 0 \tag{2-12}$$

Although this minimum is limited to the case when $\omega_n <$ 12 Hz, ultimately this minimum describes an optimal damping ratio for a system with a given stiffness. The result of the study is illustrated in Figure 2-3. Using Figure 2-3 as a design tool, an effective isolator can be designed quickly for a mechanical system operating in the frequency range of 0-20 Hz. Alkhatib *et al.* (2004) arrived at the same result using sophisticated genetic optimization algorithm.

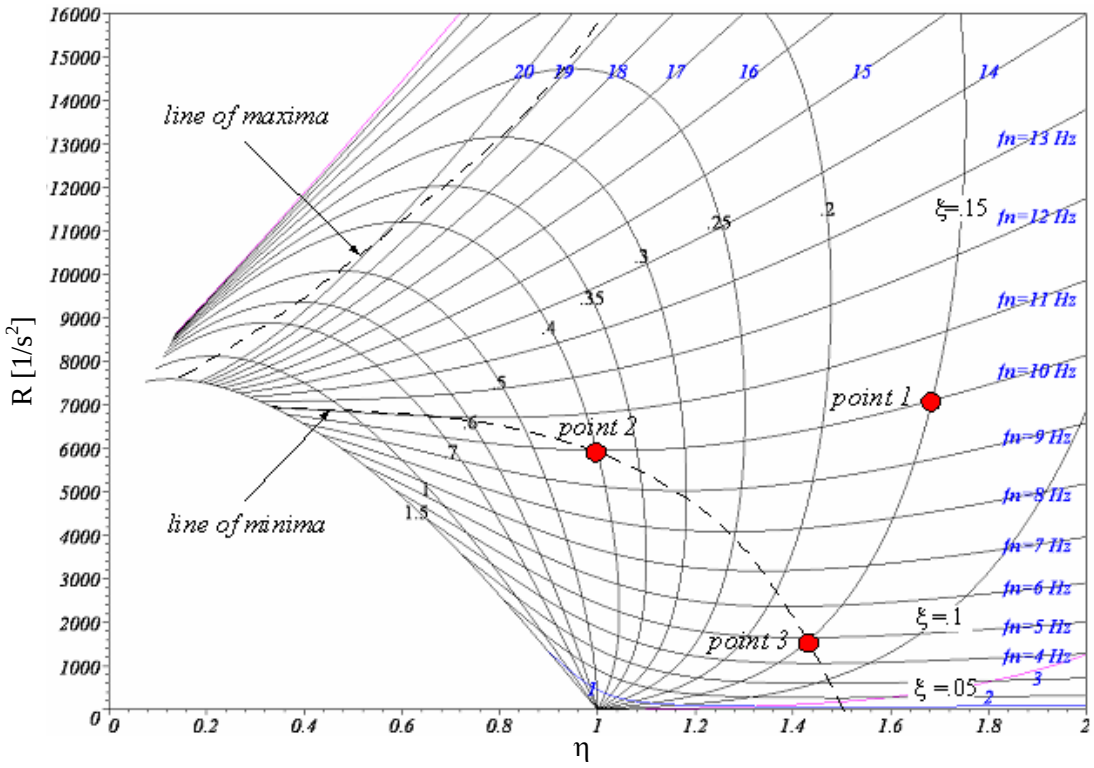

Figure 2-3: The *R* versus η map illustrating the line of optimum design for a base excited linear passive vibration isolator (Jazar *et al.*, 2003).

If the designer has the liberty of full control over the damping, the natural frequency could be selected base on time domain criteria, then damping ratio picked off Figure 2-3 to satisfy the relative motion constraint or to satisfy both relative motion and minimum acceleration, keeping in mind that, for a given base excitation, the mass acceleration is proportional to the force transmitted as per equation (2-6). However, having control over the damping is often difficult to do practically. Therefore, if the damping ratio is fixed and selected based on time domain criteria, the natural frequency is more practically tuneable in a mechanical system by varying the stiffness to yield the appropriate frequency response according to Figure 2-3.

Jazar *et al.* (2003) illustrate the performance of this method by comparing the pulse response of three systems with different damping and stiffness. In Figure 2-4 and Figure 2-5 the relative performance in the time domain of points 1 and 2, which are also mapped to the frequency domain in Figure 2-3, illustrates the improvement when using the optimal damping to minimize the transferred

force (since force transferred and acceleration are proportional) for a 10 Hz natural frequency system. Furthermore, point 3 is the optimum system for a natural frequency of 5 Hz illustrating further minimizing of the transferred force at the cost of increased relative motion as expect from Figure 2-3.

As previously mentioned, the above work is specifically geared towards the optimization of the base excitation frequency response. The work of this thesis will continue apply this optimisation to the response of forced oscillations. In addition, this technique will be used in Chapter 3 to evaluate hydraulic bushing design.

It is also worthy of noting the impact of this study on the control of semi-active actuators. The implementation of semi-active isolators represents an opportunity to tune the damping of the system to correspond with optimal performance based on Figure 2-3.

In addition, noting that the optimal frequency response does not necessarily mean that it will yield the optimum time response, low energy consuming semi-active systems could be designed with the optimal steady state nominal damping while using feedback control to change the damping real-time to suppress transients. This represents a realistic design strategy for the automotive industry since the passive mode of the mount may be sufficient to isolate both 3 and 6 cylinder modes and the semi-active mode may be used to control the transient response induced by cylinder deactivation with the entire isolation system causing a minimal increase in electrical energy consumption.

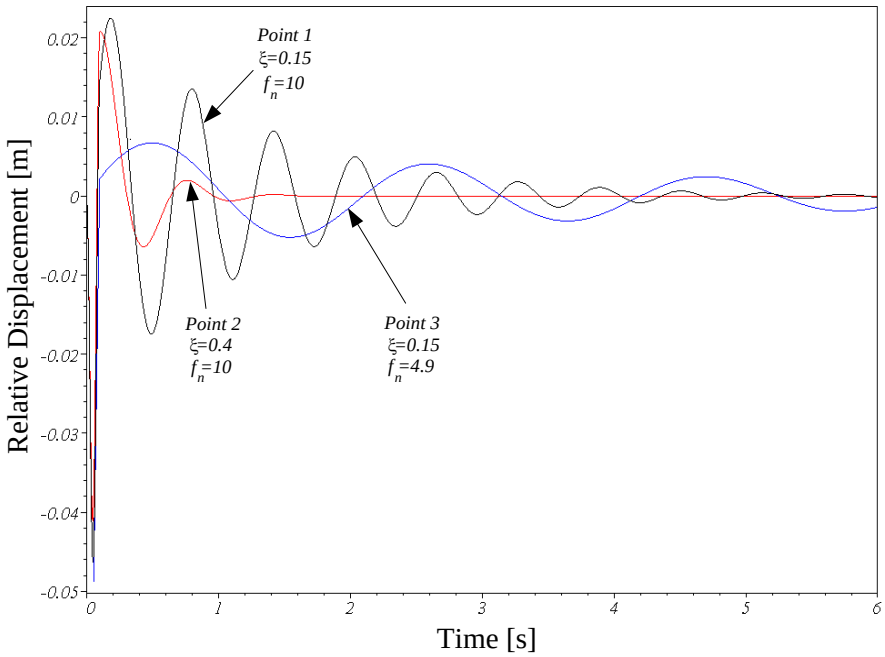

Figure 2-4: The simulated relative displacement time response to a sine square bump input, for three systems identified in Figure 2-3 (Jazar *et al*., 2003).

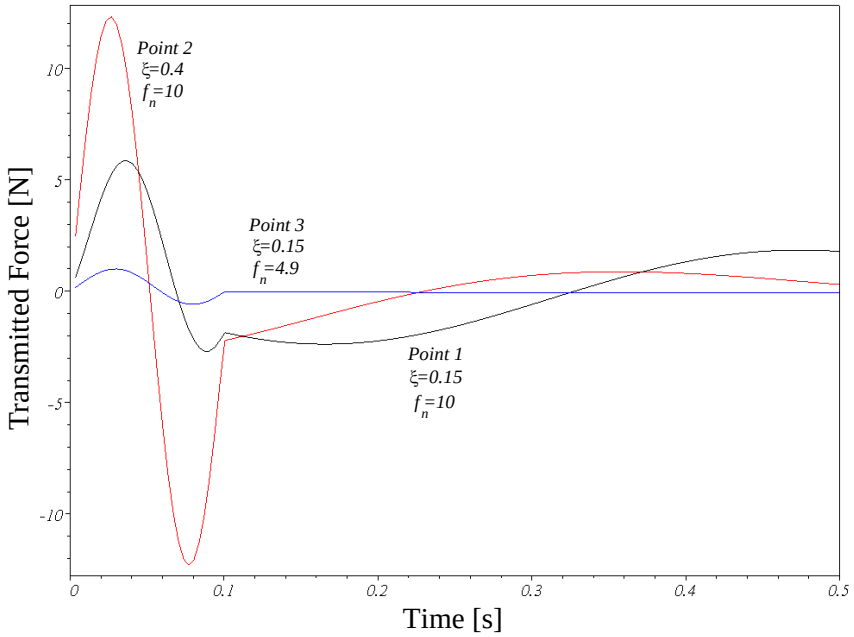

Figure 2-5: The simulated transmitted force time response to a sine square bump input, for three systems shown in Figure 2-3 (Jazar *et al*., 2003).

2.1.2 Nonlinear Optimization

No real mechanical system can be truly linear; however, most can be modeled as linear within a certain range of operation. Clearly linear approximations can yield very useful analytical results although some stability behaviour cannot be examined properly with a linear analysis. Hence, in addition to standard linear analysis of isolators, it is very common to conduct nonlinear studies.

This area of research is of great interest because of the potential to discover stability behaviour, such as bifurcations, in the case of cubic systems as shown by Oueini, Chin, and Nayfeh, (1999). Golnaraghi and Jazar (2002) found that the nonlinearity in hydraulic engine mounts could cause high frequency instabilities. Narimani, Golnaraghi, and Jazar (2004) also analytically investigated the frequency response of the piecewise linear isolator and showed the occurrence of frequency islands; this phenomena was confirmed with numerical simulation. However, a vigorous stability study is not the main focus of the nonlinear research in this thesis. Instead, the potential to use nonlinearity to manipulate steady state vibration will be examined, of course with the intent to optimize a simple passive isolator. Nayfeh, Emaci, and Vakakis (1997) used various orders of damping and stiffness nonlinearity in a three DoF vibration isolator. Nayfeh et al. (1997) essentially transferred the vibration energy to a bounded nonlinear mode of vibration known as nonlinear normal modes (NNMs). More recently, Vakakis, McFarland, Bergman, Manevitch, and Gendelman (2003) have implemented NNMs in a technique called energy pumping, using cubic nonlinearity. Vakakis et al. (2003) claim that over 80% of the input energy can be absorbed by the NNMs.

Again, the difficulty in these types of systems is that it can be challenging to mechanically create this type of nonlinearity and utilize these methods to improve performance. One option is to optimize inherent nonlinearity in mechanisms, as proposed by Golnaraghi and Jazar (2001) for the hydraulic engine mount mechanical decoupler. The other is to create and optimize a specific nonlinearity with a semi-active actuator.

The exact focus of the nonlinear portion of this thesis is again to build upon the work presented by Narimani (2004) and Narimani and Golnaraghi (204) in a similar fashion to the work that was described in section 2.1.2. Narimani (2004) and Narimani and Golnaraghi (2004) extended the research on the previous linear RMS optimization of the base excitation isolator to include nonlinear elements. Their work included a variation of equation (2-4) which incorporated cubic nonlinear stiffness and damping as follows:

$$m\ddot{z} + c_1\dot{z} + c_3\dot{z}^3 + k_1 z + k_3 z^3 = -m\ddot{y} \tag{2-13}$$

where c_1 is the linear damping coefficient, c_3 is cubic damping coefficient, k_1 is the linear stiffness, and k_3 is the cubic stiffness. Once non-dimensionalized, the equation of motion is the following:

$$\ddot{z}^* + 2\zeta\dot{z}^* + 2\xi\dot{z}^{*3} + z^* + \rho z^{*3} = \omega^2\cos(\omega\tau) \tag{2-14}$$

where z^* is a scaled displacement, ζ is the linear and ξ is the cubic nonlinear damping ratios and ρ is the cubic stiffness. Equation (2-14) also assumes that the base excitation is sinusoidal and the non-dimensional rotational frequency is ω. The process of creating non-dimensional equations of motion is detail by Nayfeh (1981).

Solving the system using perturbation methods (Nayfeh, 1981) results in a 6th order amplitude-frequency relationship as follows:

$$\begin{aligned}\frac{9}{4}\xi^2A^6\omega^6 + \left(6\zeta\xi A^4 + A^2 - 1\right)\omega^4 + \left(-\frac{3}{2}\rho A^2 + 4\zeta^2 - 2\right)A^2\omega^2 \\ + \frac{9}{16}\rho^2A^6 + \frac{3}{2}\rho A^4 + A^2 = 0\end{aligned} \tag{2-15}$$

where A is the non-dimensional amplitude of vibration. Some of the roots of equation (2-15) are complex, some are unstable equilibrium points causing a jump phenomena (as illustrated in Figure 2-6), and others correspond to frequency islands. These are generally undesirable properties;

however, the amount of nonlinearity added to the linear system is very small and these effects are avoided (Narimani & Golnaraghi, 2004).

Figure 2-6 illustrates the modified method of averaging solution (Modified MoAVG) of equation (2-14), given by equation (2-15), and the corresponding numerical solution which was generated by the author. The numerical solution to the non-dimensional amplitude-frequency response was generated using the following algorithm:

1. set zero initial conditions (ICs) and initial frequency of vibration,
2. run numerical solver with the current ICs and frequency until steady state,
3. measure steady state displacement and velocity amplitude of vibration,
4. reset the initial conditions to the steady state displacement and velocity amplitude, and increment the frequency of vibration, and
5. repeat steps 2-5 stepping across the frequency range of interest.

This method produces more accurate results that those achieved by sweeping the frequency in a solver, as illustrated by Narimani and Golnaraghi (2004). The effect of adding nonlinear damping and stiffness to the linear isolator with ω_n = 10 Hz and ζ = 0.4 on the parameters R and η illustrate the performance of the system (Figure 2-7).

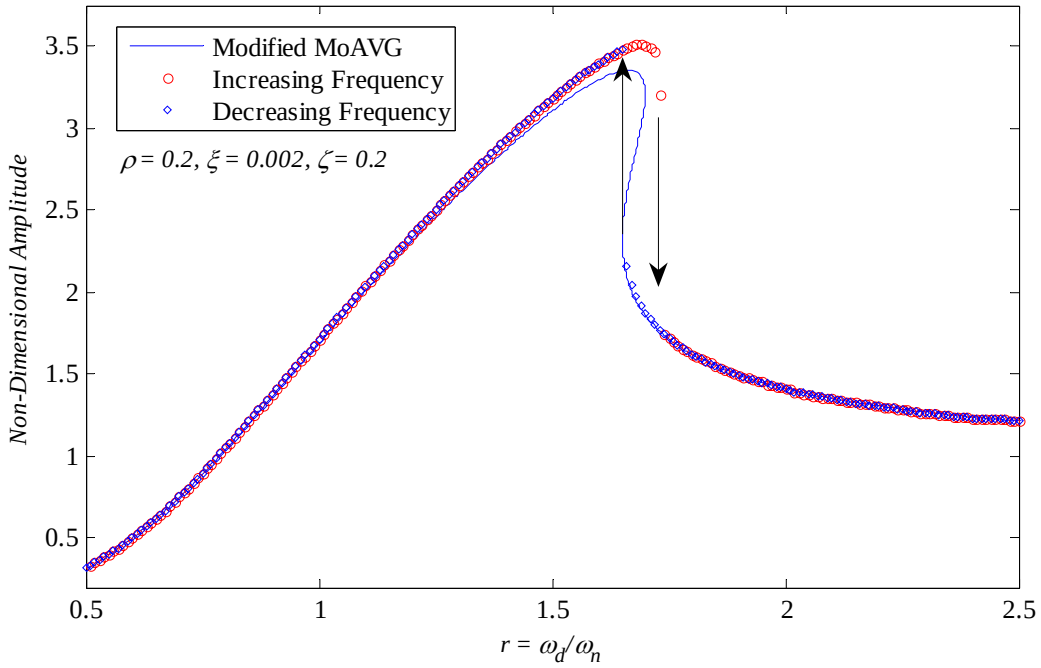

Figure 2-6: Base excitation response of non-dimensional amplitude illustrating the jump.

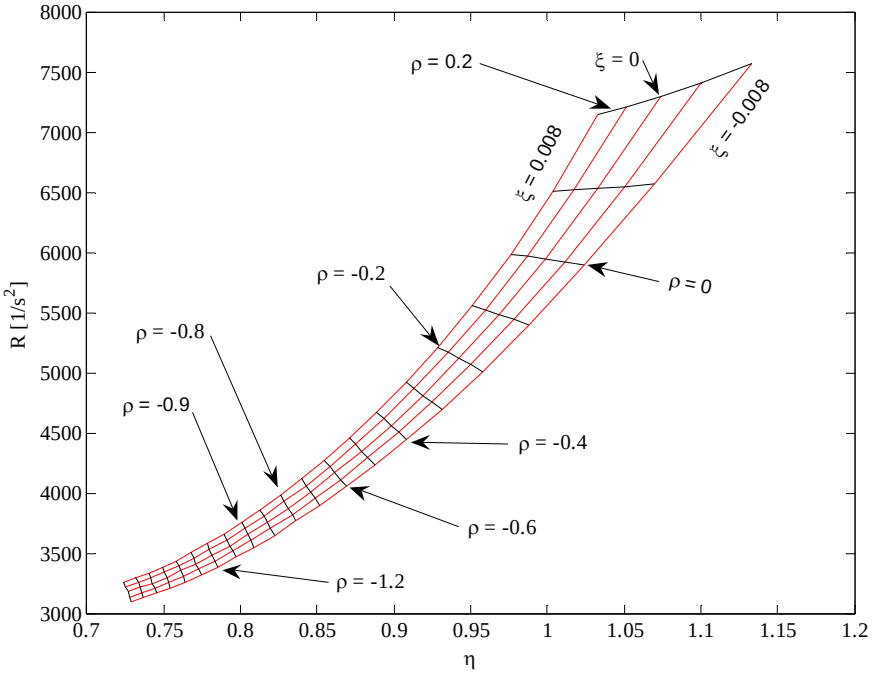

Figure 2-7: RMS patch illustrating the effect of varying nonlinear cubic stiffness and damping in a base excited system. Nominal linear system parameter values: ω_n = 10 Hz, ζ = 0.4.

It is clear that increasing negative cubic stiffness decreases the RMS values of both acceleration and displacement. Relative to the performance of the linear system shown in Figure 2-8, a small amount of negative cubic nonlinear stiffness can yield low *R* without the cost of increasing η. Note that the when the nonlinear damping and stiffness coefficients are zero the RMS values correspond to the dotted line of optimum values in Figure 2-8. Furthermore, Figure 2-8 incorporates the nonlinear RMS contours with the linear result similar to that illustrated in Figure 2-3.

It is desirable to study the RMS optimization of the nonlinear system for forced excitation, similar to the objectives of the linear study, since the cubic parameters also have the potential to improve the RMS of force and displacement transmitted for this type of input. In addition, this thesis will also investigate the effect of the nonlinear elements on the transient response.

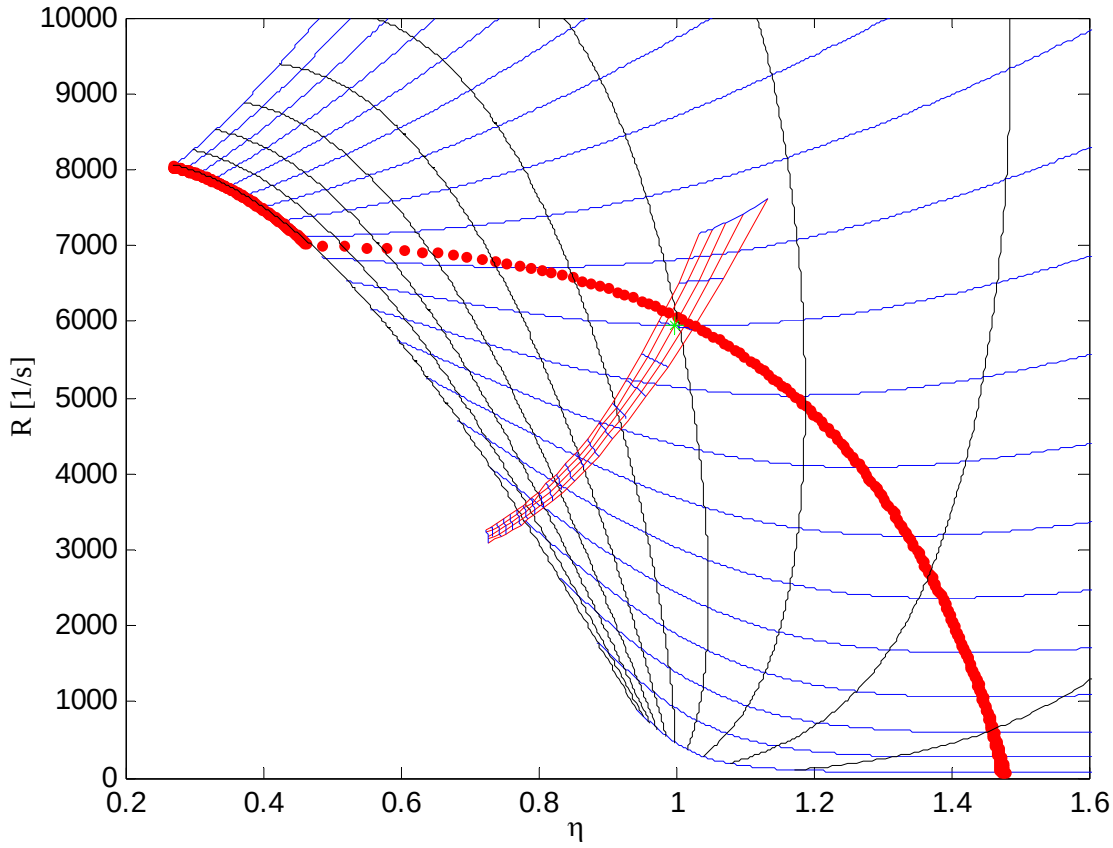

Figure 2-8: RMS patch illustrating the effect of varying nonlinear cubic stiffness and damping in an base excited system relative to varying the linear system parameters (Narimani & Golnaraghi 2004). Nominal linear system parameter values: ω_n = 10 Hz, ζ = 0.4.

2.2 Engine Isolators

2.2.1 Hydraulic Mounts and Bushings

Hydraulic mounts, such as those illustrated in Figure 1-1 and Figure 2-9, are vibration isolators used to isolate the engine from the chassis. In general, most hydraulic isolators consist of a cast rubber structure encased in metal. The rubber casting has vacancies which are two or more rubber chambers interconnected via a channel called the inertia track. These chambers are filled with a fluid, as the frame or engine vibrates, the rubber deflects causing fluid to be pumped back and forth from the pumping chamber to a more compliant chamber through the inertia track. The mass of fluid being

forced through the inertia track has a liquid column resonance and dissipates energy through fluid flow losses, causing a damping effect.

Hydraulic mounts also often incorporate a mechanical decoupler of some sort, often taking the form of a plate suspended in the fluid, constrained by a fixed cage (Figure 2-9). This decoupler acts as an amplitude-sensitive valve. At low amplitudes there is a small amount of pumping and the decoupler permits flow from the pumping chamber to the compliance chamber by-passing the inertia track; however, at high vibration amplitudes a large amount of pumping forces the decoupler against the displacement limiting cage, thus arresting decoupler flow and forcing the fluid through the inertia track. This type of hydraulic mount has soft and low damping properties at low amplitude and hard with high damping at high amplitude of vibration (Geisberger, 2000).

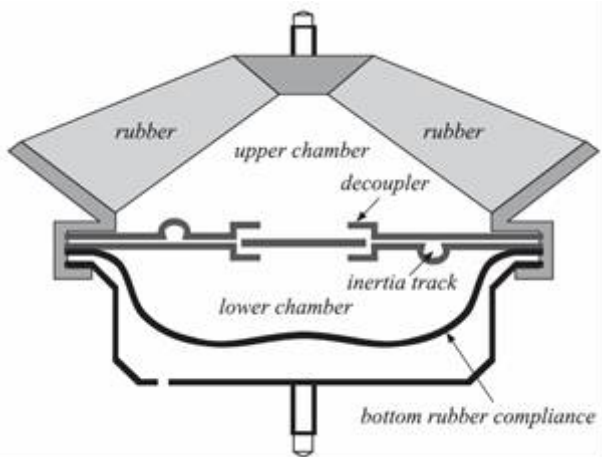

Figure 2-9: Typical hydraulic mount including the decoupler (Geisberger, 2000).

Recently, with the advent of hydraulic mounts, there has been a great deal of research on the incorporation of fluid elements in rubber engine mounts. Fortunately, this prior work paves the way for research on hydraulic bushings as the models are very similar. Figure 2-10 illustrates a simplified hydraulic bushing model of the bushing shown in Figure 1-1. The bushing is mechanically identical to the mount shown in Figure 2-9; however, it does not have a decoupler connecting the two compliance chambers.

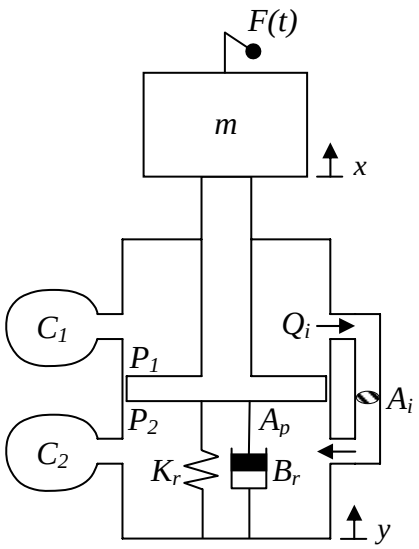

Figure 2-10: Mechanical model of a base/unbalance excited hydraulic bushing.

A simple second order model was created by Singh *et al*. (1992), ignoring the inertia of fluid volumes in the upper and lower chambers of a mount similar to that illustrated in Figure 2-9. Singh *et al*. (1992) confirmed experimentally that a simple model of a hydraulic mount can be used to model the system at low frequencies since the contributions of higher modes of vibration are negligible. Singh *et al*. (1992) also points out that the compliance of the mount is dominated by the rubber, and the effects of fluid compressibility are insignificant. Kim and Singh (1993) experimentally studied the nonlinearity in the various components of a hydraulic mount without a decoupler, thus behaving similar to a hydraulic bushing. From this study, it was found that the inertia track produces quadratic fluid damping and that the nonlinearity of the rubber compliance could be neglected.

Colgate, Chang, Chiou, Liu, and Keer (1995) studied the dynamic stiffness response of a hydraulic engine mount to composite displacement sine inputs, roughly simulating simultaneous engine and chassis vibrations – although this is not an accurate model since the true engine input is force not displacement, indicating the benefits of a base excitation experiment (the displacement is a result of the force).

Using experimental methods pioneered by many works in the early 1990s such as that of Kim and Singh (1993), Geisberger, Khajepour, and Golnaraghi (2002) developed an experimental apparatus used to extract the dynamic response of all the engine mount subsystems. From this experimental investigation, Geisberger *et al*. (2002) created an extensive analytical model including several accurate models of the nonlinearities such as decoupler flow resistance to yield accurate results over a large range of frequency and various amplitudes.

Golnaraghi and Jazar (2001, 2002) also developed a simple model of hydraulic mounts with only a decoupler and demonstrated the validity of the model experimentally for both low and high frequencies, as well as a nonlinear study of decoupler dynamics using perturbation methods. This verifies that a simple model is sufficient to study the bushing dynamics.

The design of a semi-active mount will require the development of a simple model of a hydraulic bushing. Prior research by Golnaraghi and Jazar (2001, 2002), Geisberger *et al*. (2002), Singh *et al*. (1992) and others details the nonlinearity associated with the decoupler as well as the inertia track, pumping area, and rubber compliance. Since the bushing in this study does not have a decoupler, it is proposed that a simple two degree of freedom linear model can be used to model the isolator, with the realization that the fluid damping is highly nonlinear and will require tuning for different amplitudes of vibration.

2.2.2 Semi-active Engine Isolators

In essence, a MR hydraulic bushing is a vibration isolator which is controlled by a microchip. The microchip, in conjunction with sensors to quantify the vibrations and provide feedback, controls an input electric current to the hydraulic bushing. This current creates a magnetic field in the inertia track connecting to chambers of the bushing filled with MR fluid – a solution of solid iron particles in a typically hydrocarbon based fluid medium. As the hydraulic bushing begins to vibrate it pumps MR fluid through the inertia track from one chamber to the other and vice versa. Thus, the magnetic

field induced by the microchip controller can be used to control the flow of fluid (by changing the yield stress of the fluid via the magnetic field) through the inertia track and thus change the characteristics of the hydraulic bushing.

Recently, there have been several applications of electrorheological (ER) fluids to mounts and isolators and some similar applications of MR fluids (MRFs). Williams, Rigby, Sproston, and Stanway (1993) built a simple model of an automotive engine mount using ER fluids. They were able to mathematically simulate the steady state behaviour and experimentally generate promising results with their scaled model. This design utilized the squeeze flow mode properties of the engine mount. A full scale prototype of a flow mode ER engine mount was built by Hong, Choi, Jung, Ham, and Kim (2001). They also demonstrated that using the fluid could reduce transmissibility of acceleration and displacement using skyhook controllers.

There exists very little prior work on MR engine isolators. Of the few documented experiments, Choi, Lee, Song, and Park (2002) and Choi, Song, Lee, Lim, and Kim (2003) designed and manufactured a mixed mode MR engine mount and conducted base excitation experiments to complete a hardware-in-the-loop full car model to demonstrate the effectiveness of their design, also with a skyhook controller. Shtarkmen (1993) has patented a similar design.

However, to date, there exists little evidence that there has been a great deal of research conducted on the application of MRF engine mounts in the operating in the flow mode or valve mode. One patent does exist, implementing MRF in an engine mount with a decoupler (Baudendistel *et al*., 2002). Many MR damper designs exist which utilize the flow mode characteristics and many of them are patented by Carlson, Chrzan, and James (1994). It is shown by Kuzhir, Bossis, and Bashtovoi (2003) as well as Kuzhir, Bossis, Bashtovoi, and Volkova (2003) that MR fluids perform best in pressure driven flow when the orientation of the magnetic field is perpendicular to the direction of flow. Many of the designs of Carlson *et al*. (1994) are similar to the cross-section illustration in Figure 2-11. Although this arrangement does work and is commonly used, it is not necessarily the

most efficient design. A more efficient design is presented by Gorodkin, Lukianovich, and Kordonski (1998) and patented by Kordonski *et al*. (1995). This design is similar to that of Figure 2-11 except that the fluid entering the device flows in a radial channel (Figure 2-12). The length of the flow path which is in contact with the flux is much longer in this design. This is because the entire length of the channel passes through the flux, rather than passing through only a short distance as in the previous design. The length of the path of flow in the flux is directly proportional to the pressure drop in the presence of a perpendicular flux, thus increasing the path length increases the performance of the device.

A theoretical study of the effectiveness of a MR bushing was conducted by Ahn, Ahmadian, and Morishita (1999) and Ahmadian and Ahn (1999); however, the bushing presented by Ahn *et al*. (1999) and Ahmadian and Ahn (1999) has a slightly different, model illustrated in Figure 2-13, than the mount referred to in this thesis (Figure 2-10). Moreover, Ahn *et al*. (1999) and Ahmadian and Ahn (1999) only considered increasing the damping and did not consider that the MR fluid may be useful in allowing the damping in an otherwise ordinary mount to be very small and increasing it significantly via MR effects around resonance.

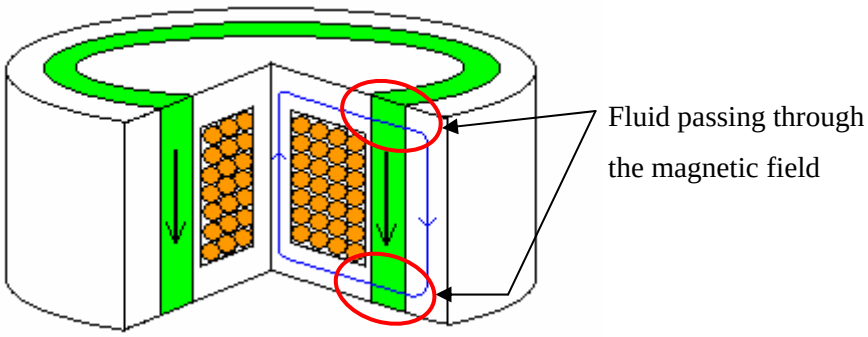

Figure 2-11: Illustration of a MR device consisting of an annular channel of pressure driven flow passing through the perpendicular magnetic field it two locations. (green – MRF, orange – magnetic coil)

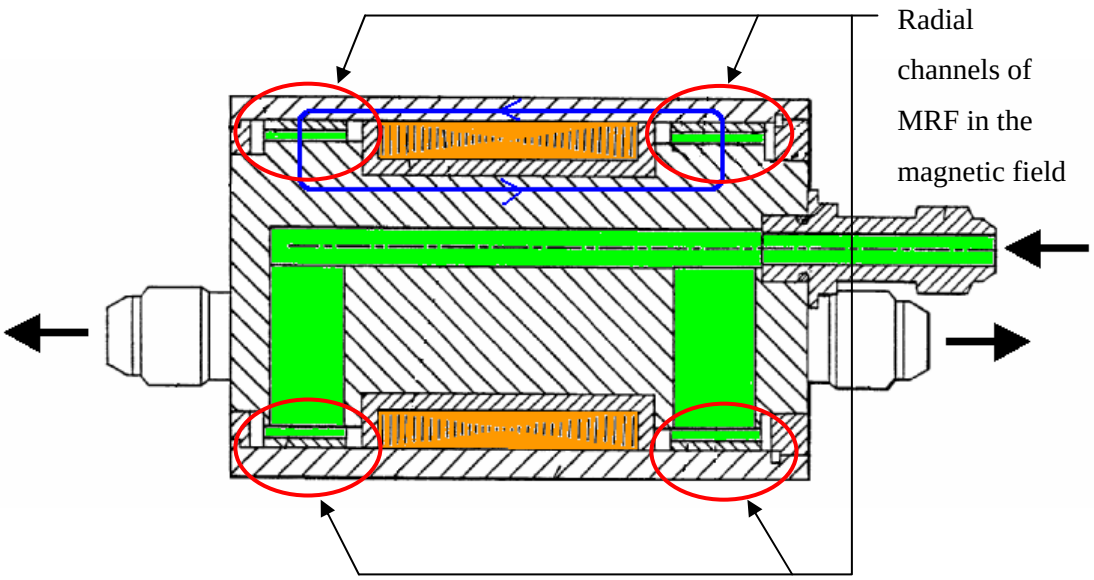

Figure 2-12: Schematic of the valve presented in Gorodkin *et al.* (1998) and Kordonski *et al.* (1995) illustrating the two radial channels of pressure driven flow passing through the perpendicular magnetic field. (green – MRF, orange – magnetic coil)

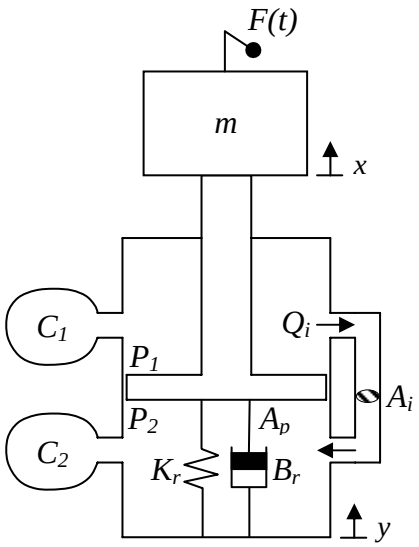

Figure 2-13: Mechanical model of the hydraulic bushing presented by Ahn *et al.* (1999) and Ahmadian and Ahn (1999).

2.3 Summary

The minimization of absolute acceleration with respect to relative displacement transmissibility for a given stiffness of a single DoF isolator is illustrated in section 2.1.1. This method will be applied in this thesis to select parameters for the transient operation of the cylinder deactivation bushing, while using feedback control during transients. Section 2.1.2 reviews the RMS response of a linear isolator with small amounts cubic stiffness and cubic damping. Previous work has found that negative cubic stiffness provides a great improvement in isolating base excitation. Cubic stiffness and damping may be induced via feedback control of a semi-active device such as the MR bushing to be developed. The RMS optimization techniques used in the base excitation linear and nonlinear results presented in this chapter will be applied in Chapter 3 to determine the optimal stiffness and damping under forced excitations.

Section 2.2.1 reviews work on the well documented hydraulic engine mount. The relationship between prior work and the bushing which is the subject of this thesis is established to be similar. Several semi-active and active engine isolators are discussed in section 2.2.2. This section introduces the reader to MR fluids and the fundamental design concepts. A valve designed by Gorodkin *et al.* (1998) and Kordonski *et al.* (1995) is illustrated. This thesis will implement this efficient flow mode MR valve in the inertia track of a hydraulic bushing.

Chapter 3
Model Development and Optimization

This chapter of the thesis includes the development of RMS optimization procedures for a forced linear and cubic nonlinear isolator. Also, the effect of the nonlinear parameters on the time response is examined briefly via numerical simulation. The optimization results are presented and discussed.

The model of the prototype MR valve that was manufactured is presented and the optimization of its performance described. Moreover, the hydraulic bushing dynamic equations are introduced, and the dynamic stiffness equation is presented. It is shown how the dynamic stiffness equation can be fit to experimental data assuming that the fluid resistance varies nonlinearly.

The RMS optimization method is applied to the hydraulic bushing model to illustrate its ability to improve the performance of the bushing inertia track and pumping chamber design.

The hydraulic bushing model is modified to model the MR bushing. Time and frequency domain simulation results are presented, illustrating the performance of the semi-active bushing. Finally, an alternative approach to changing the dynamic stiffness to perhaps better accommodate the cylinder-on-demand requirements is briefly presented.

3.1 Forced Linear Isolator Optimization

The previous work discussed in Section 2.1.1 optimized the linear isolator, shown in Figure 2-1, for base excitation inputs (Jazar *et al*., 2003). This section of the thesis develops the appropriate equations for optimizing the rotating unbalance and harmonic forcing input problems. These various inputs, illustrated for clarity in Figure 3-1, are equally important since isolators often experience more than one type of input loading, such as the case in the application of isolating engines from vehicle chassis or bodies.

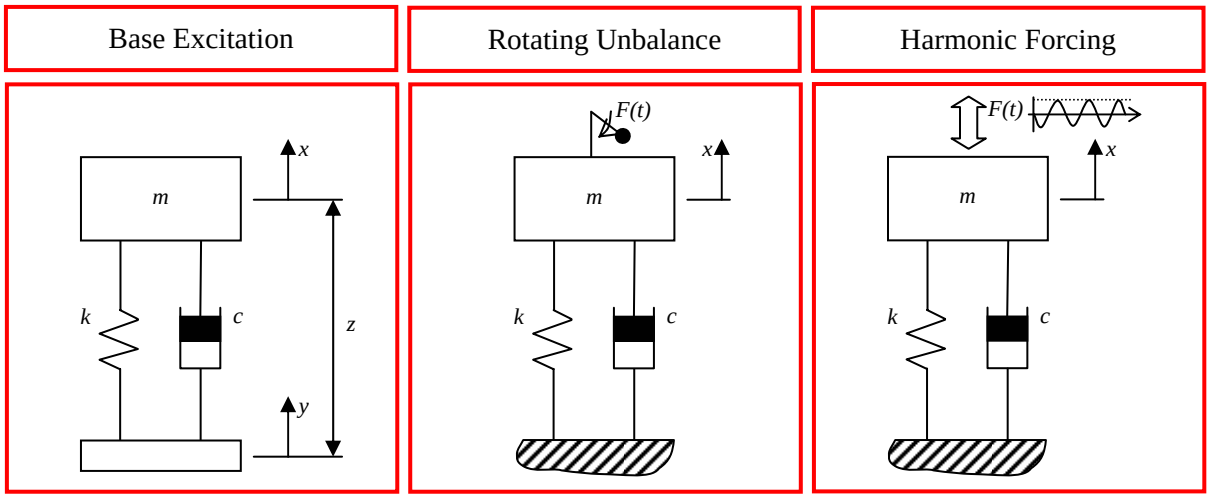

Figure 3-1: Illustration of the various simplified forms of isolator inputs.

In the previous chapter, the equation of motion of the linear isolator was presented as follows:

$$m\ddot{x} + c\dot{x} + kx = m_o e\omega_{dr}^{\ 2}\cos(\omega_{dr}t) + c\dot{y} + ky \tag{3.1}$$

Given a forced disturbance in the form of engine unbalance ($\dot{y} = y = 0$), equation (3.1) can be non-dimensionalized to the form

$$\ddot{x} + 2\zeta\omega_n\dot{x} + \omega_n^{\ 2}x = f_o(t) \tag{3.2}$$

where the input force is

$$f_o(t) = \frac{F(t)}{m} = \frac{m_o e}{m}\omega_{dr}^{\ 2}\cos(\omega_{dr}t) \tag{3.3}$$

Writing the mass normalized transferred force

$$FT(t) = \frac{F_T(t)}{m} = 2\zeta\omega_n\dot{x} + \omega_n^{\ 2}x \tag{3.4}$$

and assuming the magnitude of the input force is not a function of the driving frequency as in (3.3), thus creating the harmonic forcing input, the following transfer functions can be written relating transferred force, F_T, and displacement of the mass, X, to the input magnitude, respectively:

$$\Phi = \left|\frac{FT}{f_o}\right| = \left|\frac{F_T}{F}\right| = \sqrt{\frac{1+(2\zeta r)^2}{(1-r^2)^2+(2\zeta r)^2}} \tag{3.5}$$

$$\Lambda = \left|\frac{X}{f_o}\right| = \frac{1}{\omega_n{}^2\sqrt{(1-r^2)^2+(2\zeta r)^2}} \tag{3.6}$$

where $r=\omega_{dr}/\omega_n$. Equation (3.6) represents the scaled absolute displacement of the mass (illustrated in Figure 3-2). Equation (3.5) represents the transmitted force. This frequency response of the transmitted force is similar to that of the motion transmissibility illustrated in the previous chapter (Figure 2-2). This suggests the following relationship: $|X/f_o| \propto |X/Y|$ when comparing the harmonic forcing and base excitation frequency responses.

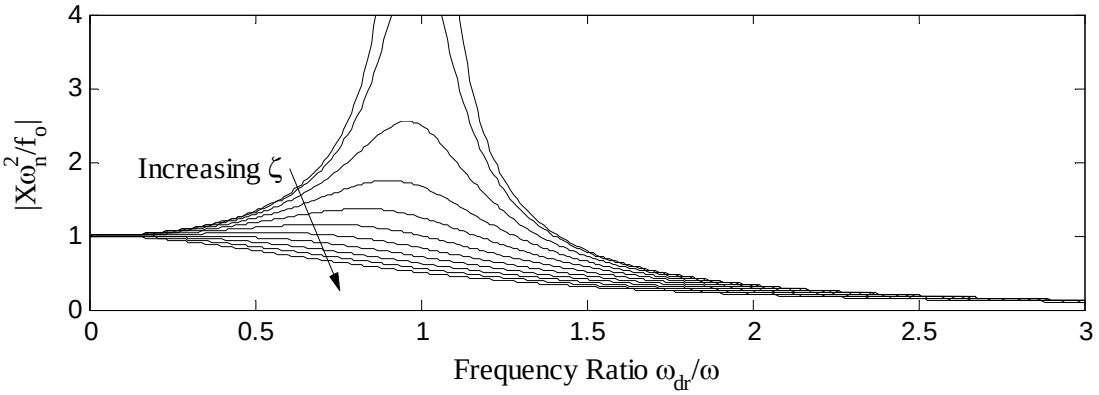

Figure 3-2: Normalized amplitude with respect to static displacement under a harmonic force.

The response of the rotating unbalance system is different from the harmonic forcing in that the magnitude of the force is assumed to vary with frequency such that

$$|F| = m_o e \omega_{dr}{}^2 \tag{3.7}$$

as in equation (3.3). The transfer functions Ψ and Ω represent transmitted force and absolute displacement, respectively.

$$\psi = \left|\frac{F_T}{m_o e \omega_n{}^2}\right| = r^2\sqrt{\frac{1+(2\zeta r)^2}{(1-r^2)^2+(2\zeta r)^2}} \tag{3.8}$$

$$\Omega = \left| \frac{X}{f_o} \right| = \frac{1}{\omega_n{}^2 \sqrt{(1-r^2)^2 + (2\zeta r)^2}} \tag{3.9}$$

Similar to the derivation of *R* and η, the RMS of Φ, Λ, Ψ, and Ω are represented as follows:

Harmonic Forcing	$\phi = RMS(\Phi)$, RMS force transmissibility
	$\gamma = RMS(\Lambda)$, RMS absolute displacement
Rotating Unbalance	$\chi = RMS(\psi)$, RMS force transmitted
	$\Gamma = RMS(\Omega)$, RMS absolute displacement

In the following sections of this chapter, the linear isolator will be optimized using the above cost functions, in a similar manner to that done for the base excitation system.

3.1.1 Harmonic Forcing Excitation

Given a harmonic forced system, the RMS force transmitted has a minimum and maximum given a certain stiffness and damping as illustrated in Figure 3-3 and Figure 3-4. As can be seen in Figure 3-3, a minimum transmitted force can be achieved for a given stiffness by tuning the amount of damping such that ζ and f_n, the natural frequency, would lie on the line of minima. Transmitted force could be maximized when $\partial\phi/\partial f_n = 0$ at the maximums shown in Figure 3-4.

Note that, for high stiffness, $\partial\phi/\partial\zeta = 0$ becomes a boundary limited minimum. Figure 3-4 illustrates that $\partial\phi/\partial f_n = 0$ yields a local maximum of transmitted force.

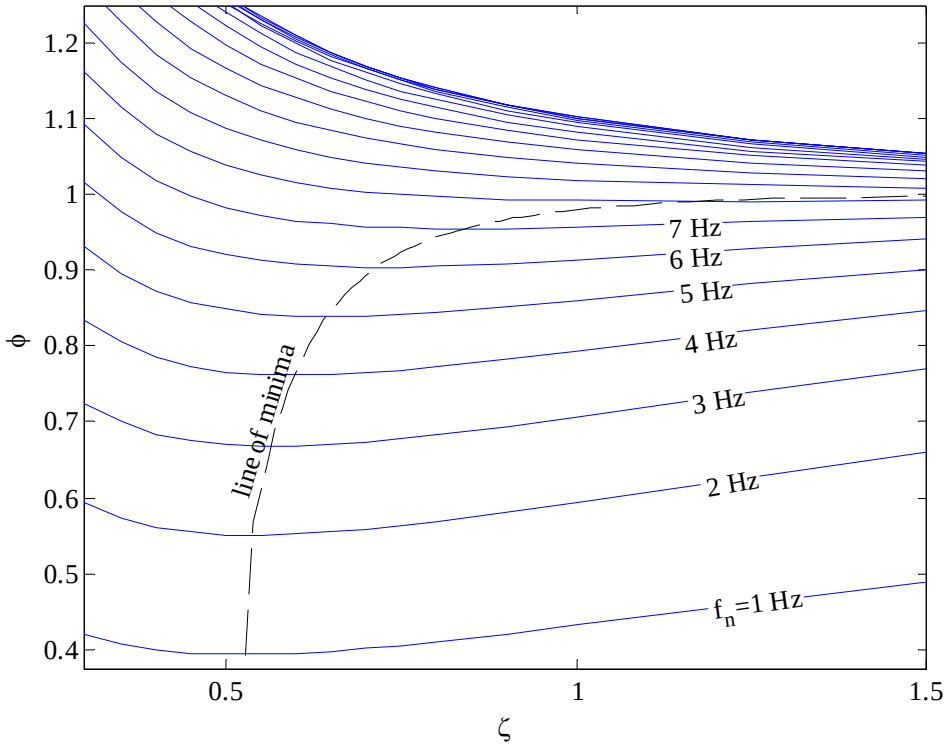

Figure 3-3: The RMS force transmissibility given a harmonic force input for a linear vibration isolator versus the damping ratio for various natural frequencies.

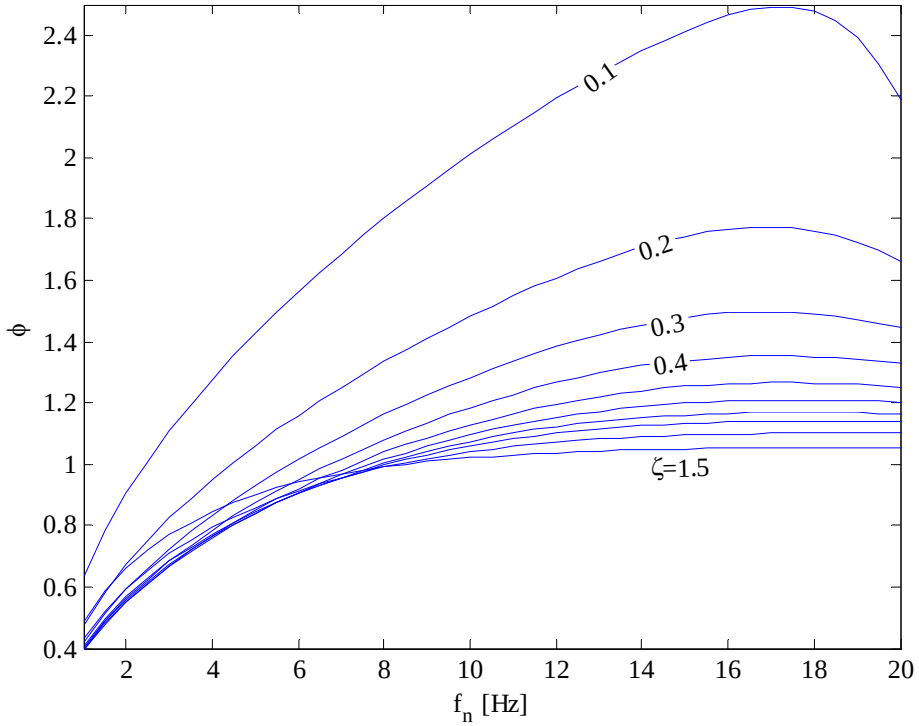

Figure 3-4: The RMS force transmissibility given a harmonic force input for a linear vibration isolator versus the natural frequency for various damping ratios.

Furthermore, Figure 3-5 and Figure 3-6 show that minimizing displacement is boundary limited given that there is no solution to either $\partial\gamma/\partial\zeta = 0$ or $\partial\gamma/\partial\omega_n = 0$.

As previously shown in the base excitation optimization, the RMS of force transmissibility (ϕ) and displacement (γ) are both functions of ζ and f_n; thus for a unique pair of ζ and f_n we can find a related value of ϕ and γ to illustrate the preceding results in the $\phi - \gamma$ plane (Figure 3-7). The line of minima in Figure 3-7 represents the optimal damping ratio which will yield the minimum force transmissibility for a given stiffness or natural frequency.

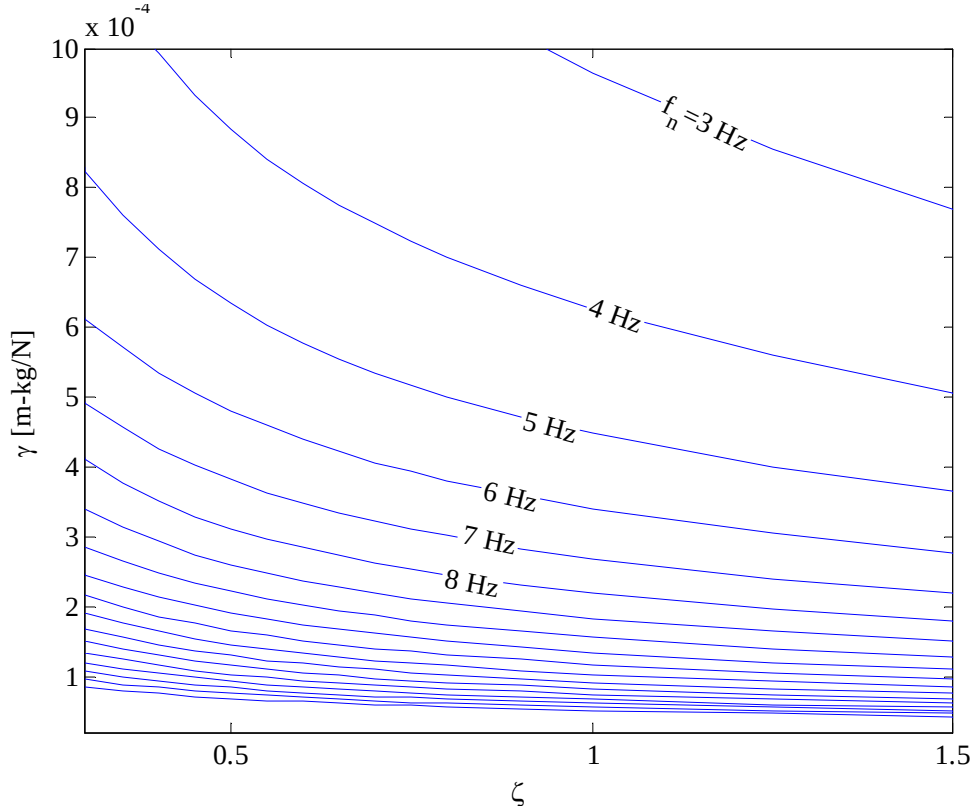

Figure 3-5: The RMS absolute displacement given a harmonic force input for a linear vibration isolator versus damping ratio for various natural frequencies.

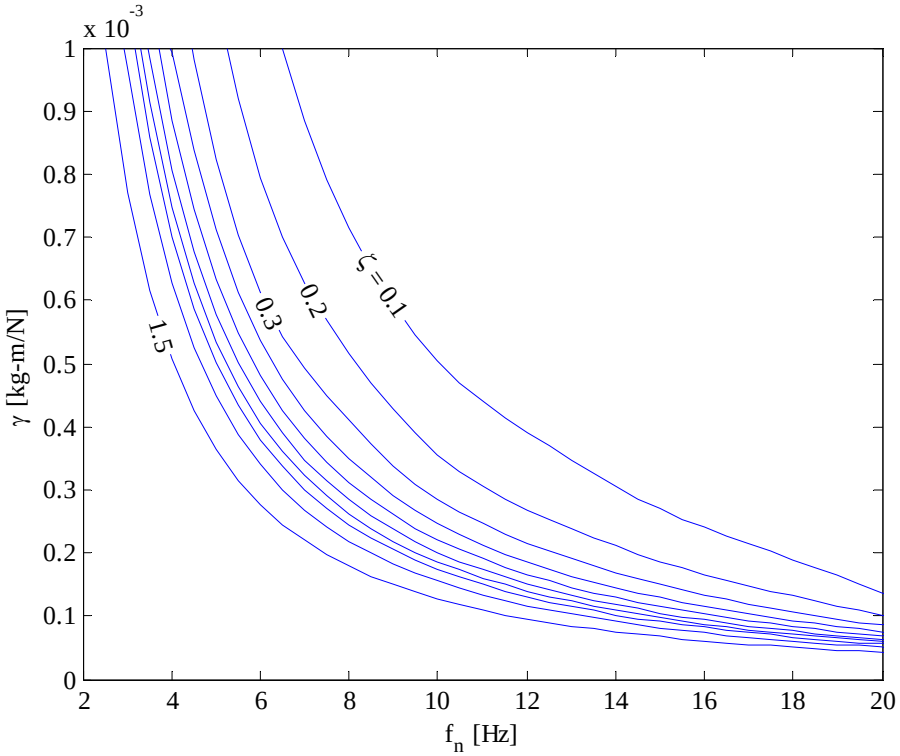

Figure 3-6: The RMS absolute displacement given a harmonic force input for a linear vibration absorber versus the natural frequency for various damping ratios.

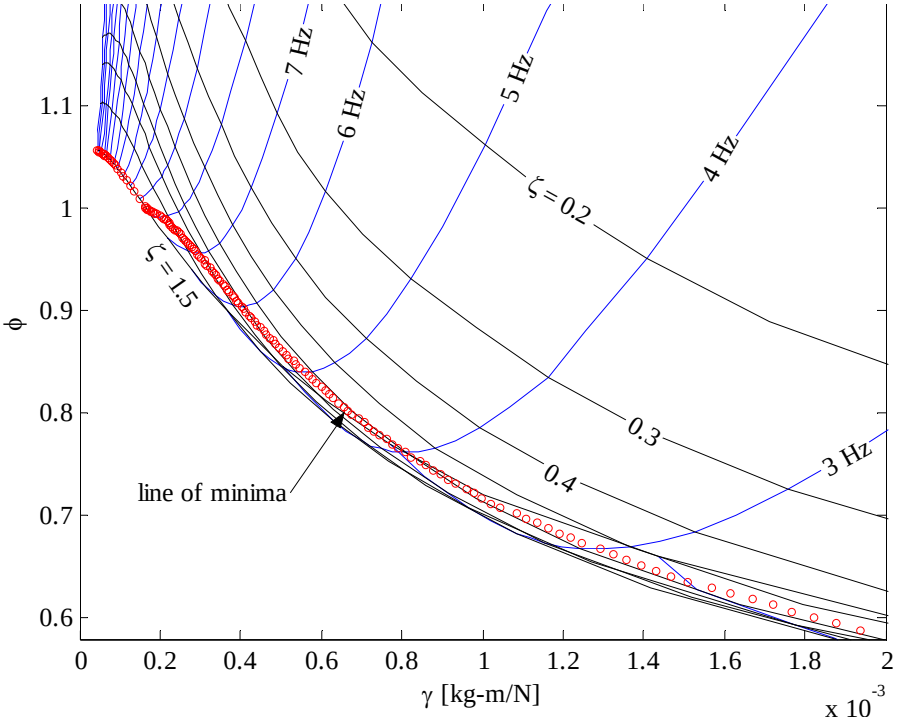

Figure 3-7: The RMS force transmissibility versus the RMS absolute displacement illustrating the line of optimum design for a harmonic forced linear passive vibration isolator.

3.1.2 Rotating Unbalance Excitation

Given a 1 DoF system excited by an unbalance, similar to the previous cases there is a local minimum associated with $\partial\chi/\partial\zeta = 0$, as illustrated in Figure 3-8. Given $\partial\chi/\partial\omega_n = 0$, there may exist both a local minimum and maximum for low damping; however the absolute minimum is again boundary limited and the absolute maximum exists at low natural frequency (Figure 3-9).

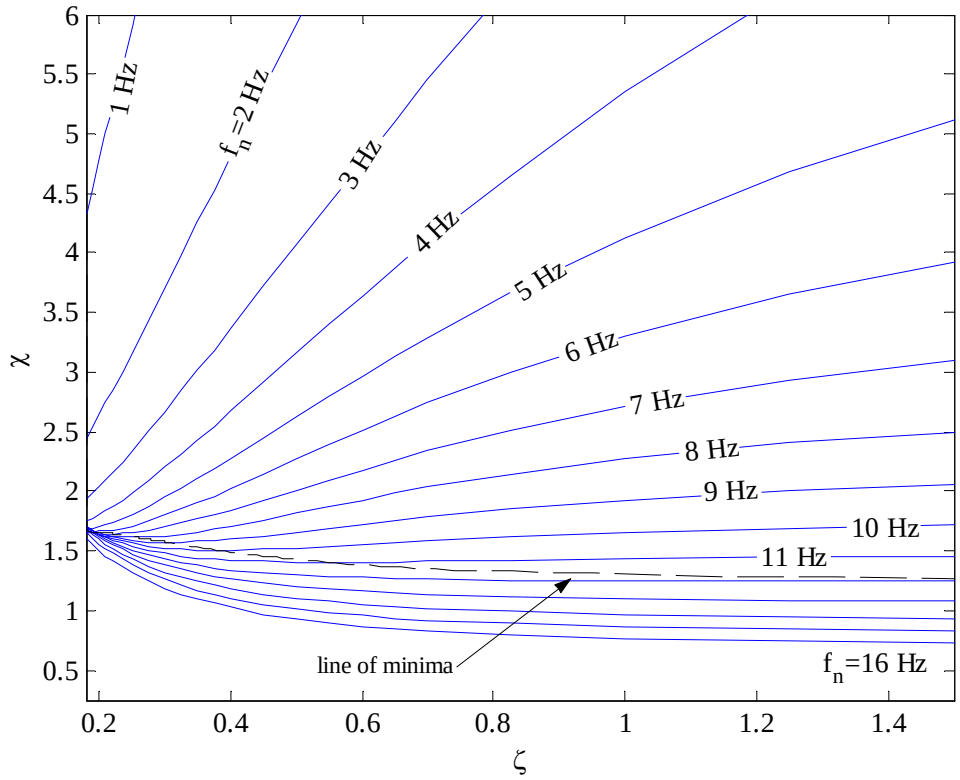

Figure 3-8: The RMS force transmitted given a rotating unbalance for a linear vibration isolator versus the damping ratio for various natural frequencies.

The maximum and minimum values of absolute displacement, Γ, exist at the boundaries and the there is no solution to $\partial\Gamma/\partial\zeta = 0$ as shown in Figure 3-10. However, Γ may be maximized with respect to natural frequencies for underdamped systems (Figure 3-11). These results are summarized in the $\chi - \Gamma$ plane, similar to the $R - \eta$ plane, where a line of minima represents the optimal damping which yields the minimum RMS force transmitted given a certain natural frequency.

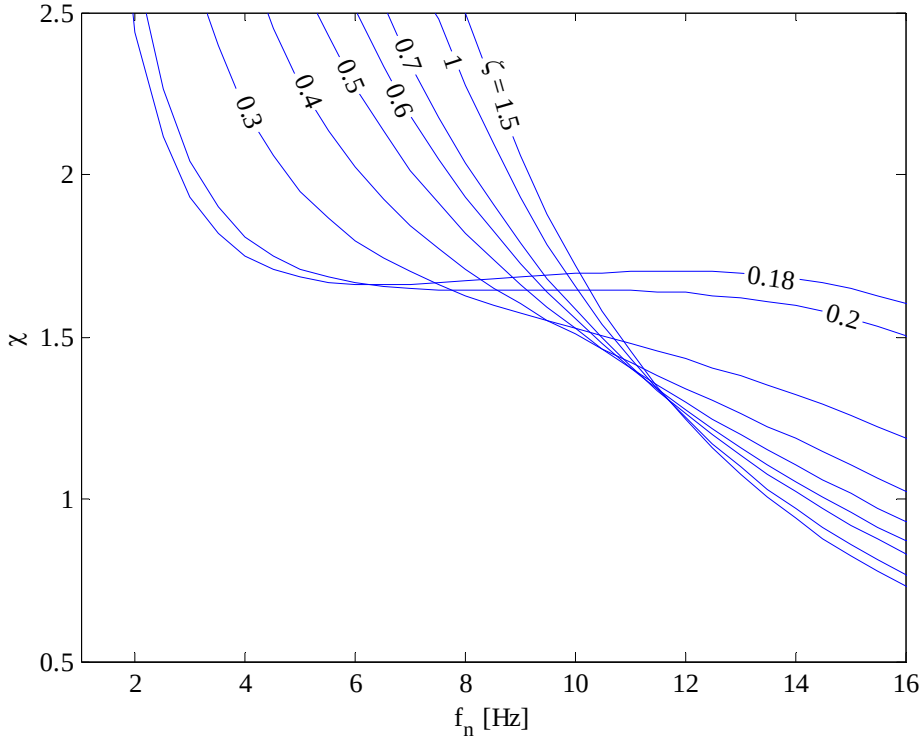

Figure 3-9: The RMS force transmitted given a rotating unbalance for a linear vibration isolator versus the natural frequency for various damping ratios.

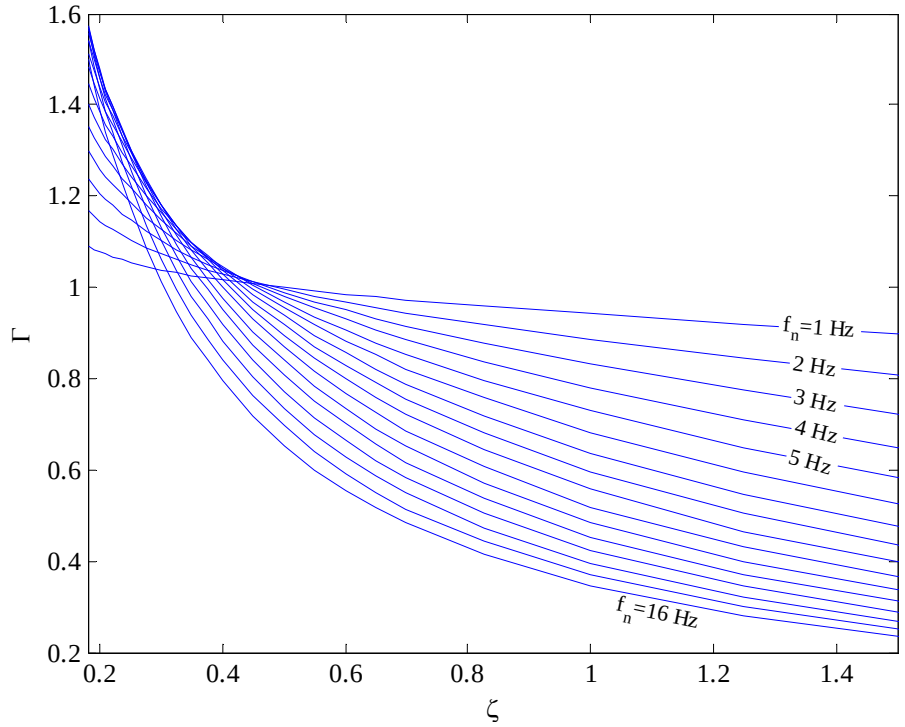

Figure 3-10: The RMS absolute displacement given a rotating unbalance for a linear vibration isolator versus damping ratio for various natural frequencies.

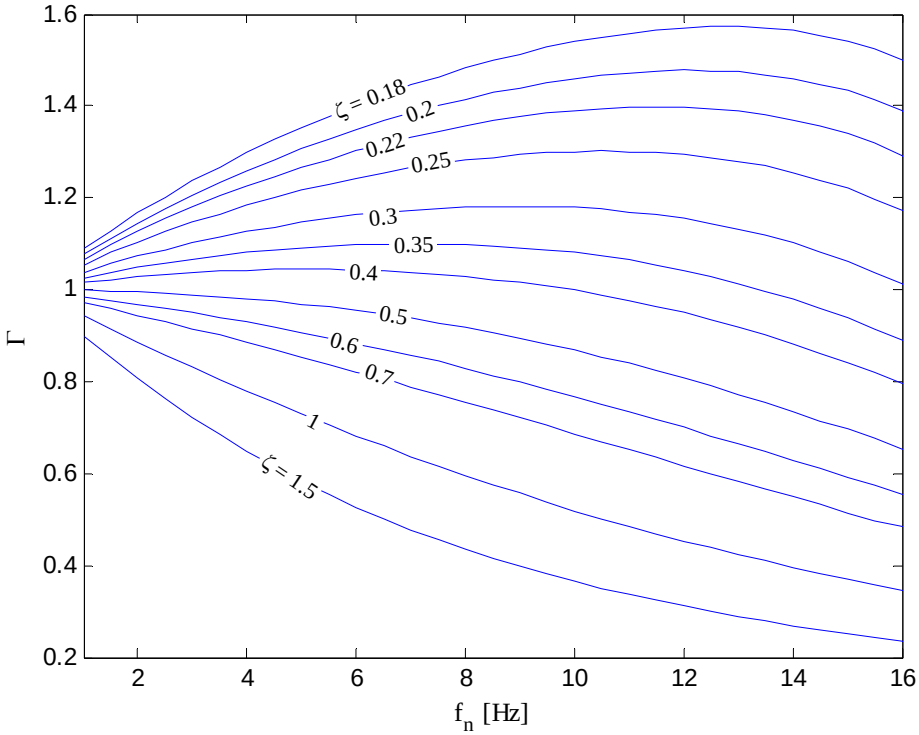

Figure 3-11: The RMS absolute displacement given a rotating unbalance for a linear vibration absorber versus the natural frequency for various damping ratios.

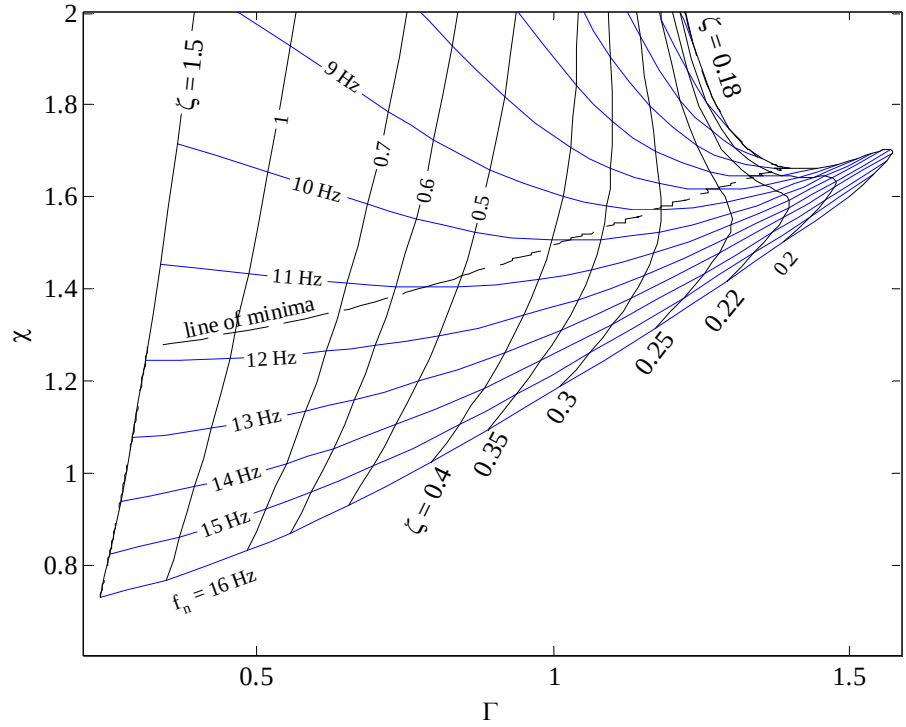

Figure 3-12: The RMS force transmitted versus the RMS absolute displacement illustrating the line of optimum design for a rotating unbalance linear passive vibration isolator.

3.1.3 Linear Optimization Summary

As mentioned previously and illustrated in Figure 3-1, three inputs to the linear isolator have been considered: base, rotating unbalance, and harmonic forcing excitations. As shown in Figure 3-13, an optimum frequency response design chart exists for each of the inputs considered.

Optimum design has been developed based on the frequency domain minimization of the RMS of the magnitude of the force transmitted through the mount with respect to the RMS of the amount of deflection of the isolator.

Figure 3-14 illustrates the optimum points in the $\zeta - f_n$ plane. Note that the base excitation and rotating unbalance excitation systems have identical optimum points. This result is expected due to the similarity of transmitted force and acceleration equations. Furthermore, Figure 3-14 illustrates the conflict of interest in designing an optimum mount for rotating unbalance or base excitations versus an optimum mount designed for harmonic forcing. For example, a damping ratio of 0.6 may satisfy one constraint (such as a time domain constraint) while the optimum natural frequency is around 4 Hz for harmonic forcing and 11 Hz for base or rotating unbalance excitations. This result illustrates the limitations of a passive mount and thus the incentive to develop semi-active designs to improve performance. Knowledge of this limitation could be useful for the application of controlling cylinder deactivation. When the cylinder switches modes it is possible that a semi-active bushing could switch to the harmonic forced optimum curve to better isolate the engine.

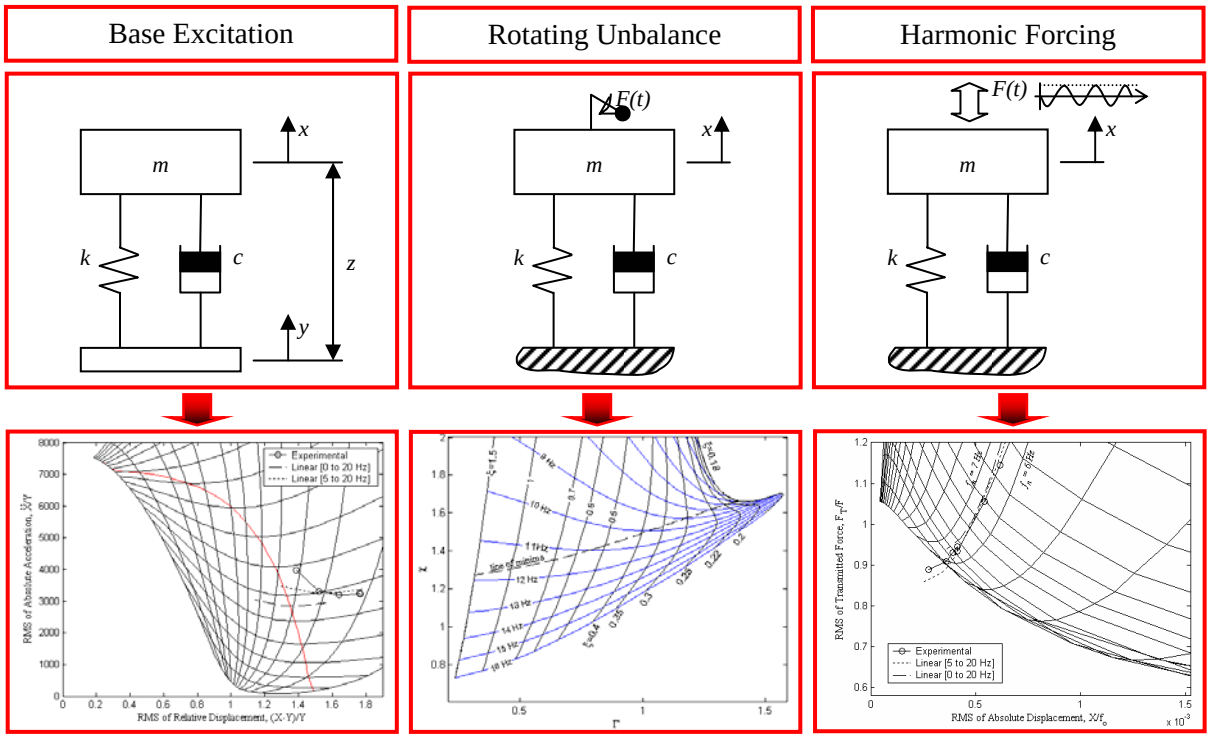

Figure 3-13: Illustrative summary of the various inputs and their corresponding RMS domain optimization design curves.

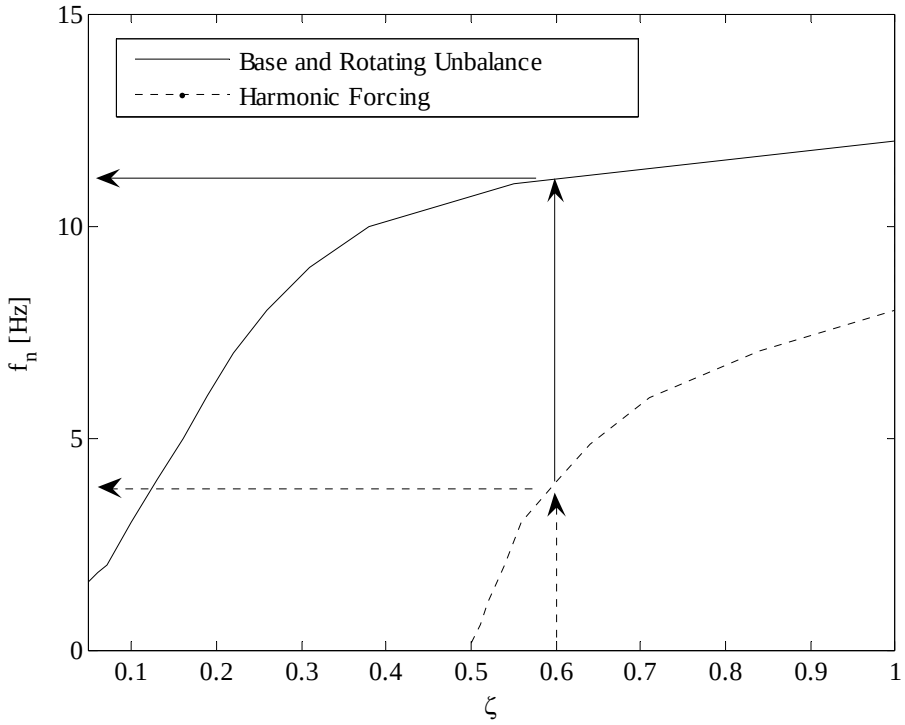

Figure 3-14: The line of optimum design for the base, rotating unbalance and harmonic forced excited linear passive vibration isolator in the $\zeta - f_n$ plane.

3.2 Force Nonlinear Isolator Optimization

A cubic nonlinear system similar to that presented in Narimani and Golnaraghi (2004) will be studied. This analysis will include a method of multiple scales time domain solution of the free vibration system to briefly describe the instability associated with the nonlinear parameters of the system, as well as a method of averaging solution of the forced response to be used in the RMS optimization of the system.

3.2.1 Unforced Time Domain Solution of Cubic Nonlinear Isolator

The equation of motion of the unforced system is

$$\ddot{x} + 2\zeta\omega_n\dot{x} + \alpha\dot{x}^3 + \omega_n{}^2 x + \gamma x^3 = 0 \tag{3.10}$$

This is similar to the linear system with cubic damping ($\alpha\dot{x}^3$) and stiffness (γx^3) added. A linearized stability analysis yields three equilibrium positions due to the cubic stiffness and damping as shown in equations (3.11) and (3.12) for the system as characterized in equation (3.11).

$$\begin{aligned} \dot{v} &= -2\zeta\omega_n v - \alpha v^3 - \omega_n{}^2 x - \gamma x^3 \\ \dot{x} &= v \end{aligned} \tag{3.11}$$

$$\begin{aligned} \left\{ x_{c,1} \quad v_{c,1} \right\} &= \left\{ 0 \quad 0 \right\} \\ \left\{ x_{c,2,3} \quad v_{c,2,3} \right\} &= \left\{ \frac{\pm\omega_n I}{\sqrt{\gamma}} \quad 0 \right\} \end{aligned} \tag{3.12}$$

The root $\left\{ x_{c,2,3} \quad v_{c,2,3} \right\}$ appears in the phase plane as a saddle point if $\gamma < 0$ (negative cubic stiffness); however, this linear analysis does not adequately describe the effect of cubic damping on the stability of the system. A perturbation solution of the nonlinear system can provide greater insight into the stability.

The standard perturbation method transformation $x = \varepsilon^n u$ (Nayfeh, 1981) is applied to yield the following system:

$$\ddot{u} + 2\zeta\omega_n\dot{u} + \alpha\varepsilon^{2n}\dot{u}^3 + \omega_n{}^2 u + \gamma\varepsilon^{2n}u^3 = 0 \tag{3.13}$$

By setting $n = 1/2$ and $\zeta = \varepsilon\mu$ equation (3.13) becomes

$$\ddot{u} + 2\varepsilon\mu\omega_n\dot{u} + \alpha\varepsilon\dot{u}^3 + \omega_n{}^2 u + \gamma\varepsilon u^3 = 0 \tag{3.14}$$

Applying the method of multiple scales (Nayfey & Mook, 1979), denoted MoMS, to (3.14), where $T_0 = t$ and $T_1 = \varepsilon t$ yields

$$\begin{aligned} &D_0^2 u(T_0,T_1) + \omega_n{}^2 u(T_0,T_1) + 2\varepsilon D_1 D_0 u(T_0,T_1) + \varepsilon\gamma u(T_0,T_1)^3 \\ &+\varepsilon\alpha D_0 u(T_0,T_1)^3 + 2\varepsilon\mu\omega_n D_0 u(T_0,T_1) + \ldots = 0 \end{aligned} \tag{3.15}$$

where D_p^n represents the n^{th} derivative with respect to the p^{th} timescale. According to the method of multiple scales an approximate solution of the form of equation (3.16) is assumed.

$$u(T_0,T_1) = u_0(T_0,T_1) + \varepsilon u_1(T_0,T_1) + \ldots \tag{3.16}$$

Substituting equation (3.16) into (3.15), neglecting high powers of ε, and setting the coefficients of equal powers of ε to 0 yields the following two equations to be solved in sequence in the form of a variation of parameters problem.

$$D_0^2 u_0(T_0,T_1) + \omega_n{}^2 u_0(T_0,T_1) = 0 \tag{3.17}$$

$$\begin{aligned} &D_0^2 u_1(T_0,T_1) + \omega_n{}^2 u_1(T_0,T_1) = \\ &-2D_1 D_0 u_0(T_0,T_1) - \gamma u_0(T_0,T_1)^3 - \alpha D_0 u_0(T_0,T_1)^3 - 2\mu\omega_n D_0 u_0(T_0,T_1) \end{aligned} \tag{3.18}$$

The solution to (3.17) is

$$u_0(T_0,T_1) = a(T_1)\cos(\omega_n T_0 + \beta(T_1)) = \frac{a(T_1)e^{(\omega_n T_0 + \beta(T_1))j} + a(T_1)e^{-(\omega_n T_0 + \beta(T_1))j}}{2} \tag{3.19}$$

This result is substituted into (3.18) to yield

$$D_0^2 u_1(T_0,T_1) + {\omega_n}^2 u_1(T_0,T_1) = \left\{ a(T_1)\omega_n D_1\beta(T_1) - \frac{3}{8}\gamma a(T_1)^3 \right. \\ \left. -\left[\mu{\omega_n}^2 a(T_1) + \frac{3}{8}\alpha{\omega_n}^3 a(T_1)^3 + \omega_n D_1 a(T_1) \right] j \right\} e^{(\omega_n T_0 + \beta(T_0))j} + NST + CC \tag{3.20}$$

where, as denoted by Nayfeh (1981), *NST* are non-secular terms and *CC* represents the complex conjugate of the terms appearing to the right of the equality. Since the perturbation solution does not include secular terms (Nayfeh, 1981), the coefficient of $e^{(\omega_n T_0 + \beta(T_0))j}$ in equation (3.20) must sum to zero as shown in equation (3.21).

$$\left\{ a(T_1)\omega_n D_1\beta(T_1) - \frac{3}{8}\gamma a(T_1)^3 - \left[\mu{\omega_n}^2 a(T_1) + \frac{3}{8}\alpha{\omega_n}^3 a(T_1)^3 + \omega_n D_1 a(T_1) \right] j \right\} = 0 \tag{3.21}$$

Solving equation (3.21) results in the equations for the rate of change of amplitude and phase.

$$a' = -\mu\omega_n a - \frac{3}{8}\alpha{\omega_n}^2 a^3, \ \beta' = \frac{3}{8}\frac{\gamma a^2}{\omega_n} \tag{3.22}$$

Furthermore, solving the first order differential equations in equation (3.22) yields the amplitude of the response as a function of time.

$$a(T_1) = \frac{4}{\sqrt{\frac{2(3\alpha\omega_n {a_0}^2 + 8\mu)}{\mu {a_0}^2} e^{2\mu\omega_n T_1} - \frac{6\alpha\omega_n}{\mu}}} \tag{3.23}$$

The above result, equation (3.23), is illustrated and compared to the numerical solution of the system in Figure 3-15.

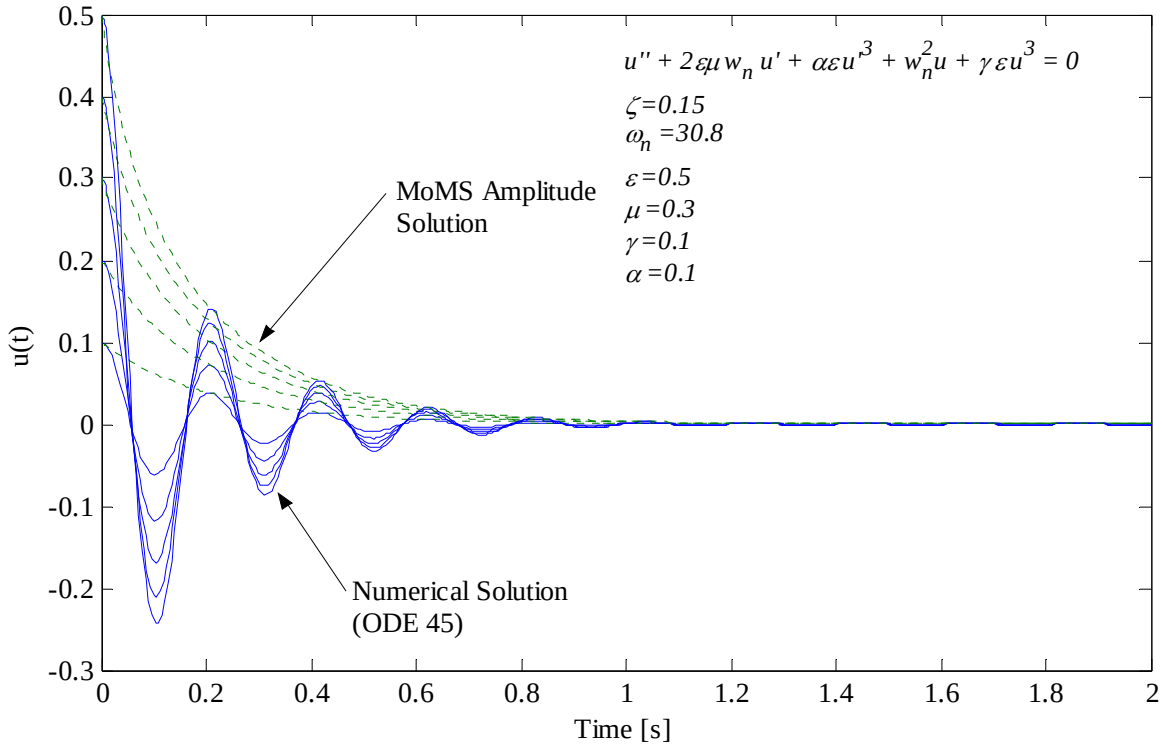

Figure 3-15: Amplitude versus time relative to the actual numerical simulation of the nonlinear system for various initial conditions.

By examining the first derivative of the steady state amplitude with respect to the initial condition a_0, we find that a critical amplitude results when $\alpha < 0$ (or in the presence of negative cubic damping). This suggests an unstable limit cycle. The diameter of the limit cycle is given by a_{lc} as follows:

$$a_{lc} = \pm\frac{2}{3}\frac{\sqrt{-6\mu\alpha\omega_n}}{\alpha\omega_n} \tag{3.24}$$

This is demonstrated for the following case: $\mu = 0.03$, $\alpha = -0.5$, and $\omega_n = 30.8$. This yields the limit cycle $a_{lc} = \pm 0.228$. If the initial amplitude is beyond this critical amplitude the system is unstable, as illustrated in Figure 3-16.

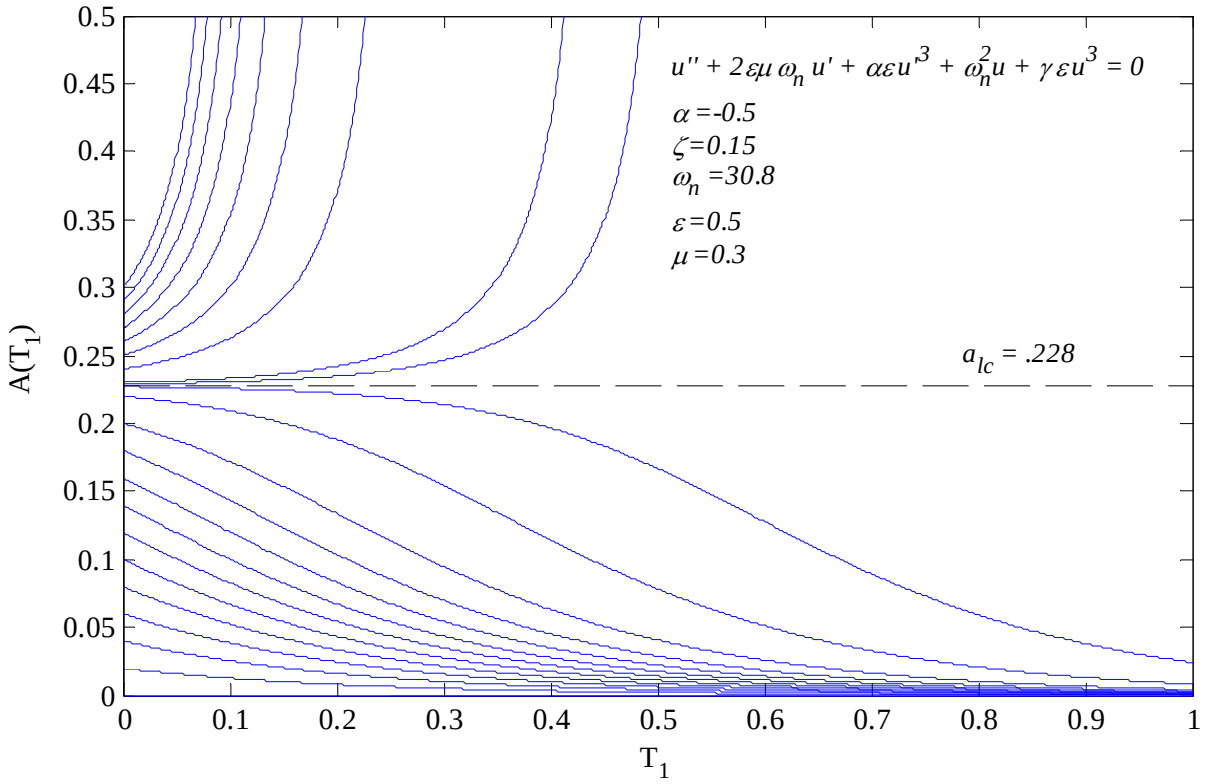

Figure 3-16: Amplitude of the time domain solution of the cubic nonlinear system for various initial conditions illustrating the unstable limit cycle of the negative cubic damping system.

3.2.2 Forced Solution of Cubic Nonlinear Isolator

Given the unbalance excitation of the nonlinear system under study can be expressed as

$$m\ddot{x} + c_1\dot{x} + c_3\dot{x}^3 + k_1 x + k_3 x^3 = m_o e\omega_d{}^2 \cos(\omega_d t) \tag{3.25}$$

This can be non-dimensionalized with the following substitutions to yield equation (3.26).

$$\frac{k_3}{m} = k_3^* \omega_n{}^2, \quad f_o = \frac{m_o e}{m}, \quad u = \frac{x}{f_o}, \quad \tau = \omega_n t, \quad \omega = \frac{\omega_d}{\omega_n}$$

$$\frac{\partial(\ )}{\partial\tau} = \frac{1}{\omega_n}\frac{\partial(\ )}{\partial t}, \frac{\partial^2(\ )}{\partial\tau^2} = \frac{1}{\omega_n{}^2}\frac{\partial^2(\ )}{\partial t^2}$$

$$u'' + 2\zeta_1 u' + 2 f_o{}^2\omega_n{}^2\zeta_3 u'^3 + u + f_o{}^2 k_3^* u^3 = \omega^2\cos(\omega\tau) \tag{3.26}$$

Substituting the cubic stiffness parameter $\rho = f_o^{\,2} k_3^{\,*}$ and cubic damping parameter $\xi = f_o^{\,2} \omega_n^{\,2} \zeta_3$ yields the simplified equivalent system:

$$u'' + 2\zeta u' + 2\xi u'^3 + u + \rho u^3 = \omega^2 \cos(\omega\tau) \tag{3.27}$$

The system can be solved using the modified averaging technique (MoAVG – discussed in Chapter 2) assuming a solution

$$u(\tau) = a(\tau)\cos(\omega\tau + \beta(\tau)) \tag{3.28}$$

The differential equation can be solved by variation of parameters, where

$$u' = -a\omega \sin(\omega\tau + \beta) \tag{3.29}$$

$$u' = a'\cos(\omega\tau + \beta) - a\omega\sin(\omega\tau + \beta) - a\beta'\sin(\omega\tau + \beta) \tag{3.30}$$

$$\omega\tau + \beta = \phi \tag{3.31}$$

$$u'' = -a'\omega\sin(\omega\tau + \beta) - a\omega^2\cos(\omega\tau + \beta) - a\omega\beta'\cos(\omega\tau + \beta) \tag{3.32}$$

Equations (3.29) to (3.32) are used to develop the following equalities:

$$a'\cos(\phi) - a\beta'\sin(\phi) = 0 \tag{3.33}$$

$$\begin{aligned} &a'\omega\sin(\phi) + a\omega\beta'\cos(\phi) = -a\omega^2\cos(\phi) - 2\zeta a\omega\sin(\phi) - 2\xi a^3\omega^3\sin(\phi) \\ &+2\xi a^3\omega^3\sin(\phi)\cos^2(\phi) + a\cos(\phi) + \rho a^3\cos^3(\phi) - \omega^2\cos(\phi - \beta) \end{aligned} \tag{3.34}$$

Using the above relationships, the first derivatives of the amplitude and phase can be obtained:

$$\begin{aligned} \omega a' = &\frac{1}{4}\rho a^3\sin(2\phi) - \zeta_1 a\omega + \zeta_1 a\omega\cos(2\phi) - \frac{1}{2}\omega^2\sin(\beta) + \frac{1}{2}\omega^2\sin(-2\phi + \beta) \\ &+\xi a^3\omega^3\cos(2\phi) - \frac{1}{4}\xi a^3\omega^3\cos(4\phi) - \frac{3}{4}\xi a^3\omega^3 - \frac{1}{2}a\omega^2\sin(2\phi) \\ &+\frac{1}{2}a\sin(2\phi) + \frac{1}{8}\rho a^3\sin(4\phi) \end{aligned} \tag{3.35}$$

$$\omega a\beta' = \frac{3}{8}\rho a^3 + \frac{1}{2}\rho a^3\cos(2\phi) - \frac{1}{2}a\omega^2 - \frac{1}{2}a\omega^2\cos(2\phi) + \frac{1}{2}a + \frac{1}{2}a\cos(2\phi)$$
$$+\frac{1}{8}\rho a^3\cos(4\phi) - \zeta a\omega\sin(2\phi) - \frac{1}{2}\omega^2\cos(-2\phi+\beta) - \frac{1}{2}\omega^2\cos(\beta)$$
$$+\frac{1}{4}\xi a^3\omega^3\sin(4\phi) - \frac{1}{2}\xi a^3\omega^3\sin(2\phi) \tag{3.36}$$

and averaged over a period of 2π to yield:

$$\omega a' \approx \frac{1}{2\pi}\int_0^{2\pi}\omega a' = -\left(\zeta a\omega + \frac{3}{4}\xi a^3\omega^3\right) - \frac{1}{2}\omega^2\sin(\beta) \tag{3.37}$$

$$\omega a\beta' \approx \frac{1}{2\pi}\int_0^{2\pi}\omega a\beta' = \frac{3}{8}\rho a^3 + \frac{a(1-\omega^2)}{2} - \frac{1}{2}\omega^2\cos(\beta) \tag{3.38}$$

Equations (3.37) and (3.38) can be solved for the frequency and phase as follows:

$$\omega^2 = \left(2\zeta a\omega + \frac{3}{2}\xi a^3\omega^3\right)^2 + \left(\frac{3}{4}\rho a^3 + a(1-\omega^2)\right)^2 \tag{3.39}$$

$$\beta = \tan^{-1}\left(\frac{2\zeta\omega + \frac{3}{2}\xi a^2\omega^3}{\frac{3}{4}\rho a^2 + (1-\omega^2)}\right) \tag{3.40}$$

The solution can be compared to the linear solution by neglecting the nonlinear terms:

$$\omega^2 = \left(2\zeta a\omega\right)^2 + \left(a(1-\omega^2)\right)^2 \tag{3.41}$$

Solving the above for amplitude yields the linear solution for amplitude:

$$a = \frac{\omega}{\sqrt{\left(2\zeta\omega\right)^2 + \left(1-\omega^2\right)^2}} \tag{3.42}$$

Similarly, (3.40) yields the linear phase:

$$\beta = \tan^{-1}\left(\frac{2\zeta\omega}{(1-\omega^2)}\right) \tag{3.43}$$

The cubic nonlinear frequency response defined in terms of amplitude and phase as shown in equations (3.39) and (3.40) can be used in Section 3.2.3 to examine the change in the RMS forced response due to the addition of cubic stiffness ρ and cubic damping ξ.

3.2.3 RMS Optimization of the Cubic Nonlinear System

A RMS study of the transmitted force and relative displacement can be done using the MoAVG results for the cubic system. Given a nominal linear system with f_n = 10 Hz and ζ = 0.4, the RMS of the frequency response is generated for a range of ρ and ξ similar to that of Narimani and Golnaraghi (2004).

This study yields a RMS patch similar to that of the base excited system where an increase in negative cubic stiffness can simultaneously reduce both transmitted force and displacement from the optimal linear response (at point ρ = 0 and ξ = 0). This result is illustrated in Figure 3-17. The performance relative to changing the parameters of the linear system is shown in Figure 3-18.

Furthermore, it has been found through numerical simulation of the time response of the nonlinear system that while the small amounts of nonlinearity may have a significant impact on the frequency response, their effect on the peak displacement and peak force transmitted is negligible.

For example, the time domain response to a step or impulse response is highly sensitive to the linear parameters, as illustrated in the step response shown in Figure 3-19. However, Table 3-1 shows that the non-dimensional peak force and peak displacement do not change as the nonlinear parameters traverse the limits of the patch defined in Figure 3-17. The same phenomenon is demonstrated via numerical simulation in Table 3-2 given a pulse input. Note that X_{st} is the static displacement due to the step loading.

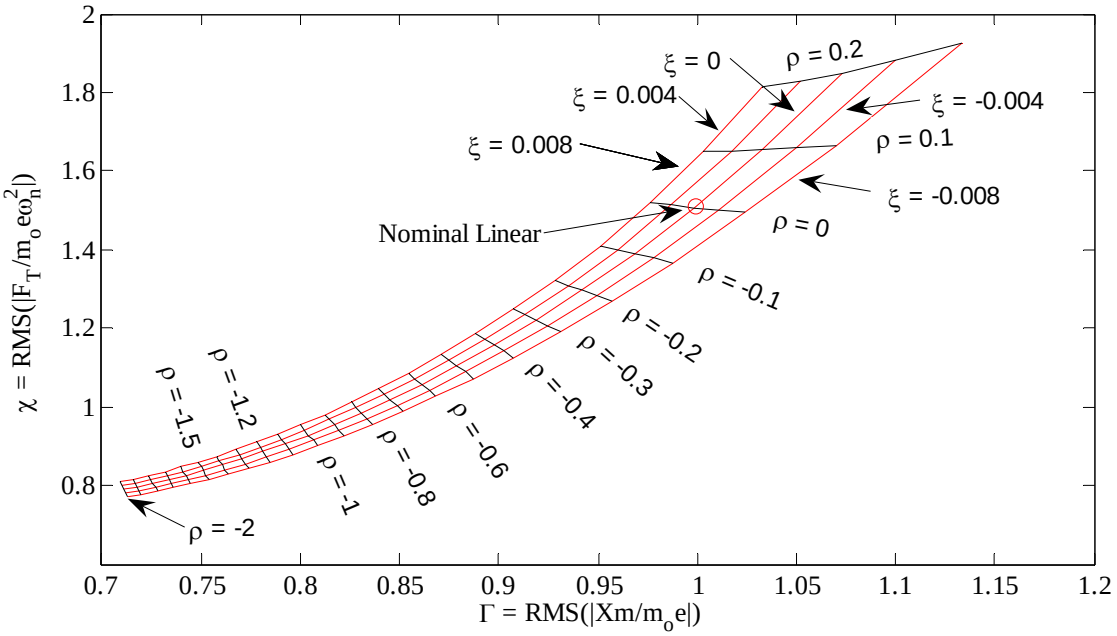

Figure 3-17: RMS patch illustrating the effect of varying nonlinear cubic stiffness and damping in an unbalance forced system.

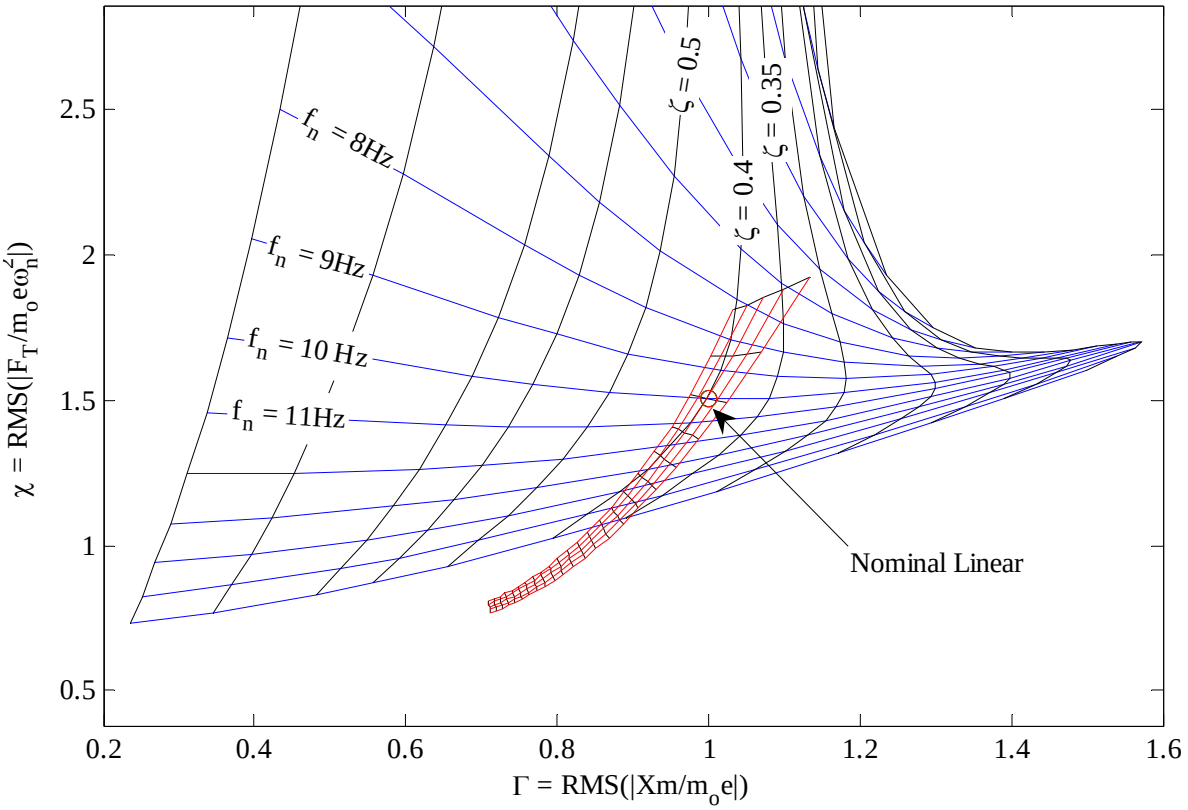

Figure 3-18: RMS patch illustrating the effect of varying nonlinear cubic stiffness and damping in an unbalance forced system.

Table 3-1: Dimensionless peak step response data describing the effect of varying the nonlinear stiffness and damping.

ρ	ξ	Peak X/X_{st}	% Diff. ($x10^5$)	Peak F_T/F_o	% Diff. ($x10^5$)
0.0	0.000	1.2529443669	0.0000	1.2529667499	0.0000
0.2	0.008	1.2529443534	-1.0732	1.2529667617	0.9413
-2.0	0.008	1.2529445000	10.6211	1.2529666306	-9.5246
0.2	-0.008	1.2529443537	-1.0530	1.2529667620	0.9616
-2.0	-0.008	1.2529445002	10.6414	1.2529666308	-9.5044

Table 3-2: Dimensionless peak pulse response data describing the effect of varying the cubic nonlinear stiffness and damping.

ρ	ξ	Peak X/X_{st}	% Diff. ($x10^5$)	Peak F_T/F_o	% Diff. ($x10^5$)
0.0	0.000	0.4204936779	0.0000	0.4205413158	0.0000
0.2	0.008	0.4204936554	-5.3676	0.4205412942	-5.1338
-2.0	0.008	0.4204937868	25.8986	0.4205414150	23.5972
0.2	-0.008	0.4204936766	-0.3171	0.4205413154	-0.0900
-2.0	-0.008	0.4204938081	30.9491	0.4205414362	28.6411

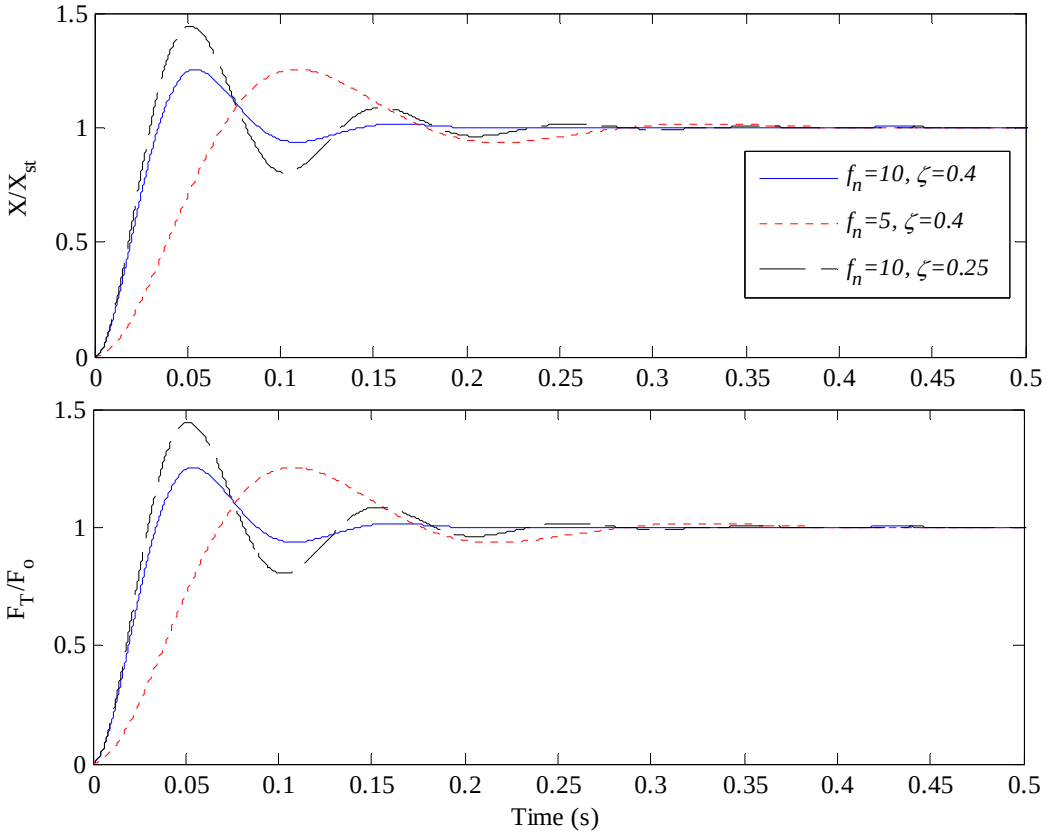

Figure 3-19: Effects of varying linear parameters on the dimensionless response to a step input.

3.3 MR Hydraulic Bushing Modeling

3.3.1 MR Bushing Design

Based on the valve design proposed by Gorodkin *et al*. (1998) and Kordonsky *et al*. (1995), an MR valve module has been designed to be implemented on hydraulic bushing P/N 90575028 (GM Saturn). The built in inertia track of the bushing will be blocked and the fluid is forced to bypass through the MR valve module. This design effectively creates a tuneable inertia track.

The design of the valve is illustrated in Figure 3-20 where L_c is the length of the coil, g and w are the height and width of the fluid channel, D_i and D_o are the inner and outer diameters of the coil, and t is the outer wall thickness of the valve. The color brown denotes materials of low magnetic permeability, such as aluminium; these are used to control the flux path and are not intended to conduct the flux.

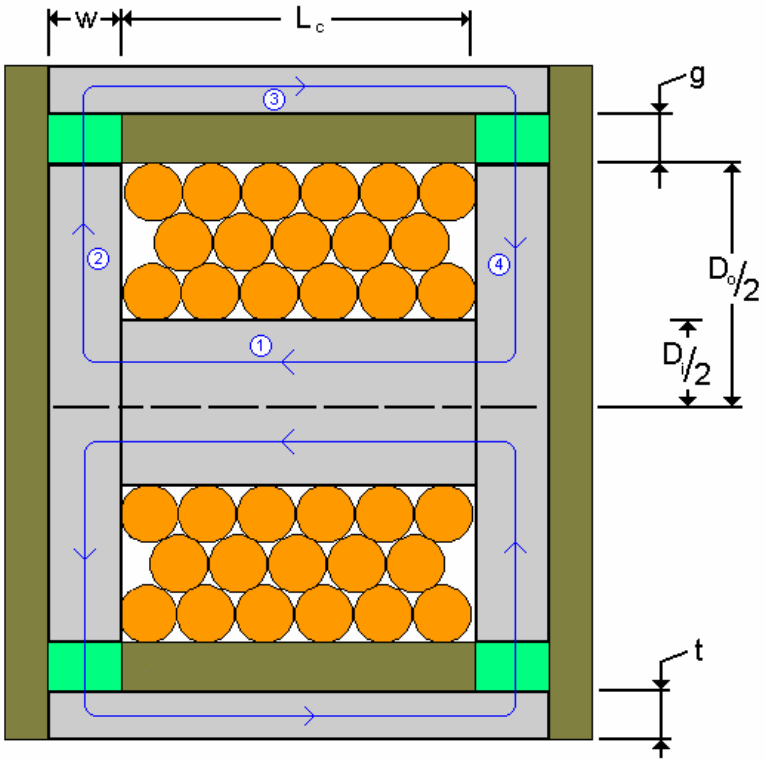

Figure 3-20: MR valve schematic illustrating the radial fluid channels (green) as well as the flux path (blue), the coil (orange), core material (grey) and non-flux conducting material (brown).

The core of the valve is to be manufactured from ‘magnetically soft’ material, illustrated in the color grey. This is a material which has the properties of high permeability, low hysteresis and low residual magnetism (Askeland, 1996). For the purpose of the prototype, readily available low carbon 1020 steel was selected. The magnetic properties of this material are illustrated in Figure 3-21.

The total length of the of the fluid path in the flux is approximately

$$l \cong 2\pi D_o \tag{3.44}$$

since it flows through two radial channels between the entrance and exit of the valve (denoted Q_{in} and Q_{out} in Figure 3-22).

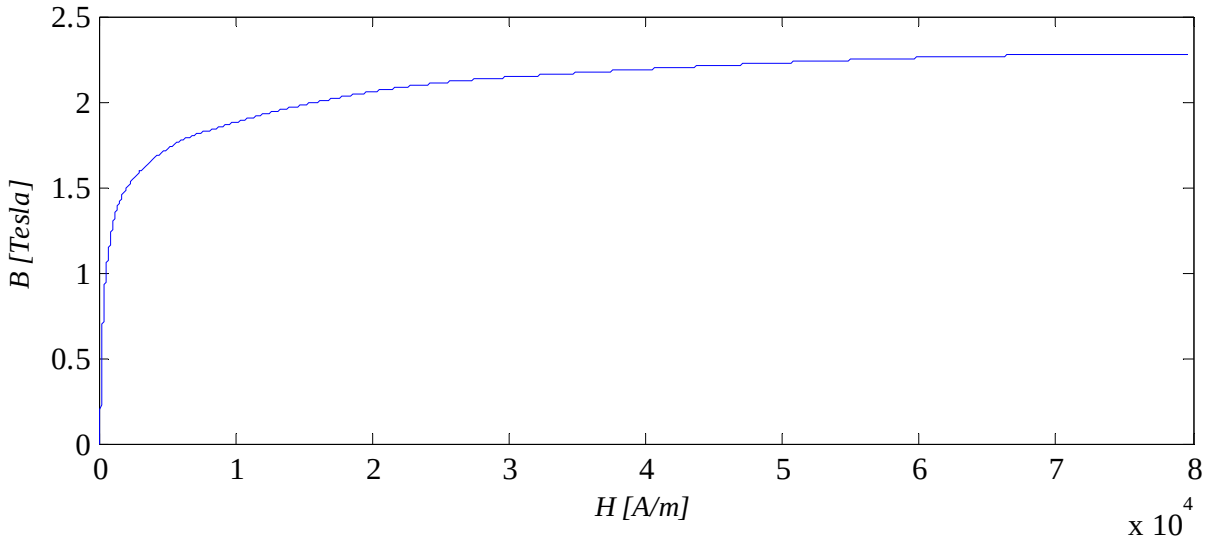

Figure 3-21: Magnetic properties of 1020 steel.

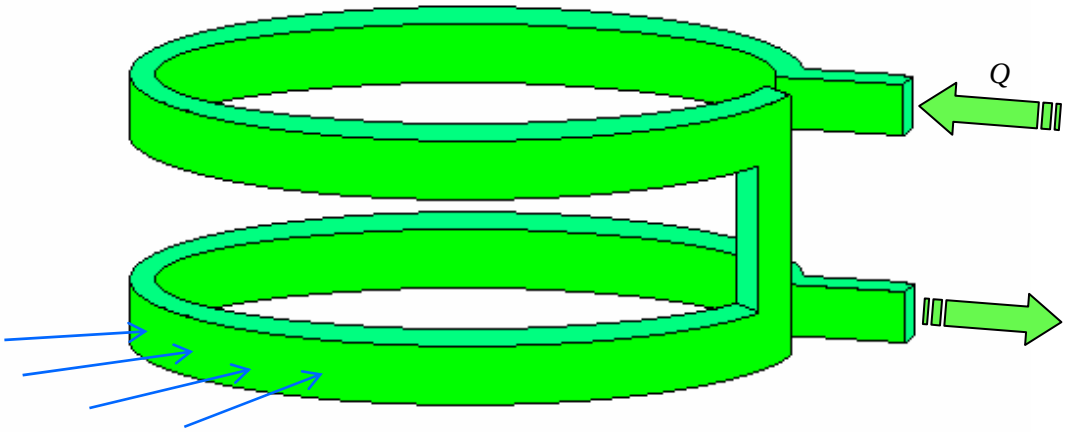

Figure 3-22: Radial channel of MR fluid through the valve.

The performance of the valve was optimized using the NCD Toolbox of Matlab 6.5. The inputs, or variables to be determined, to the optimization algorithm are the valve parameters illustrated in Figure 3-20 as well as the wire gauge (diameter). All of these parameters affect the magnitude of the flux which passes through the channel of MR fluid (Halliday, Resnick, & Walker 1997).

The criteria for optimization are the minimization of the rise time of the magnetic circuit, the input current and the controllability ratio of the device.

The rise time, denoted τ_e, is the time required for the coil to energize and begin to function. It is measured in seconds and is computed via the following formula:

$$\tau_e = \frac{L_i}{R_e} = \frac{\mu_{core}}{4}\left(\frac{D_o - D_i}{D_o + D_i}\right) D_i^{\,2} \frac{WPA}{OPM} \tag{3.45}$$

where L_i is the inductance of the coil, R_e is the electrical resistance, μ_{core} is the magnetic permeability of the core material, *WPA* is the number wires per square metre and *OPM* is the resistance (in ohms) per metre. The wire specifications *OPM* and *WPA* are obtained from wire gauge data. This information is supplied by magnet wire manufacturers.

The input current is derived from the resistance (R_e) of the circuit and the input voltage (V_{in}). The input voltage is assumed to be 24 V. Thus the current is computed from $I = V_{in} / R_e$.

The controllability of the valve is an expression which relates the pressure drop across the valve with and without a magnetic field. The total pressure drop as defined by Lord Corporation (1999) is

$$\Delta p = \Delta p_\mu + \Delta p_\tau = R_f Q + \frac{c_{MR} l}{g} \tau_y(I) = R_f Q + K_{MR} I(t) \tag{3.46}$$

where Δp_μ is the viscous pressure drop, Δp_τ is the pressure drop due to yielding the MR fluid, c_{MR} is a constant of magnitude 2-3 depending on the controllability, l is the length of the inertia track, R_f is the hydraulic resistance to flow, and τ_y is the yield stress of the fluid. A measurable property of MRFs is the yield stress as a function of the field intensity in the fluid. Yield stress can be written $\tau_y = \tau_y(H_f)$ or since H_f is a function of the input current $\tau_y = \tau_y(I)$. The controllability ratio is defined as follows:

$$\kappa = \frac{\Delta p_\mu}{\Delta p_\tau} \propto R_f \Big/ \left(\frac{c_{MR} l}{g} \tau_y \right) \tag{3.47}$$

To determine the magnitude of the controllability, the yield stress must be computed. In order to determine the yield stress, the magnetic circuit equations must be solved given the inputs to the optimization algorithm as listed above. The circuit is solved via the simplified equation $NI = R_{eq} \varphi$, which can be rearranged to yield the field intensity as shown in equations (3.48) and (3.49).

$$\varphi = NI / R_{eq} \tag{3.48}$$

$$H_f = \varphi \Big/ \left(\mu_{MR} A_f' \right) = NI \Big/ \left(R_{eq} \mu_{MR} A_f' \right) \tag{3.49}$$

where N is the number of wire turns in the coil, φ is the flux, A_f' is the effective area of the magnetic pole where $A_f = lw$, μ_{MR} is the magnetic permeability of the MRF, and R_{eq} is the equivalent magnetic resistance of the circuit. The resistance is computed by integrating the flux per unit area over the entire length of the path, resulting in equation (3.50).

$$R_{eq} = \frac{g}{\mu_{MR} A_f'} + \frac{4(L_c + w)}{\mu_{core}\pi}\left[\frac{1}{D_i^2} + \frac{1}{\left(D_o + g + t\right)^2 - \left(D_o + g\right)^2}\right] + \frac{1}{\mu_{core}\pi w}\ln\left(\frac{D_o}{D_i}\right) \qquad (3.50)$$

The MRF used was a formulation developed by General Motors Corporation, referred to as 13MAG098. The approximate magnetic properties of this fluid are summarized in Figure 3-23 and Table 3-3.

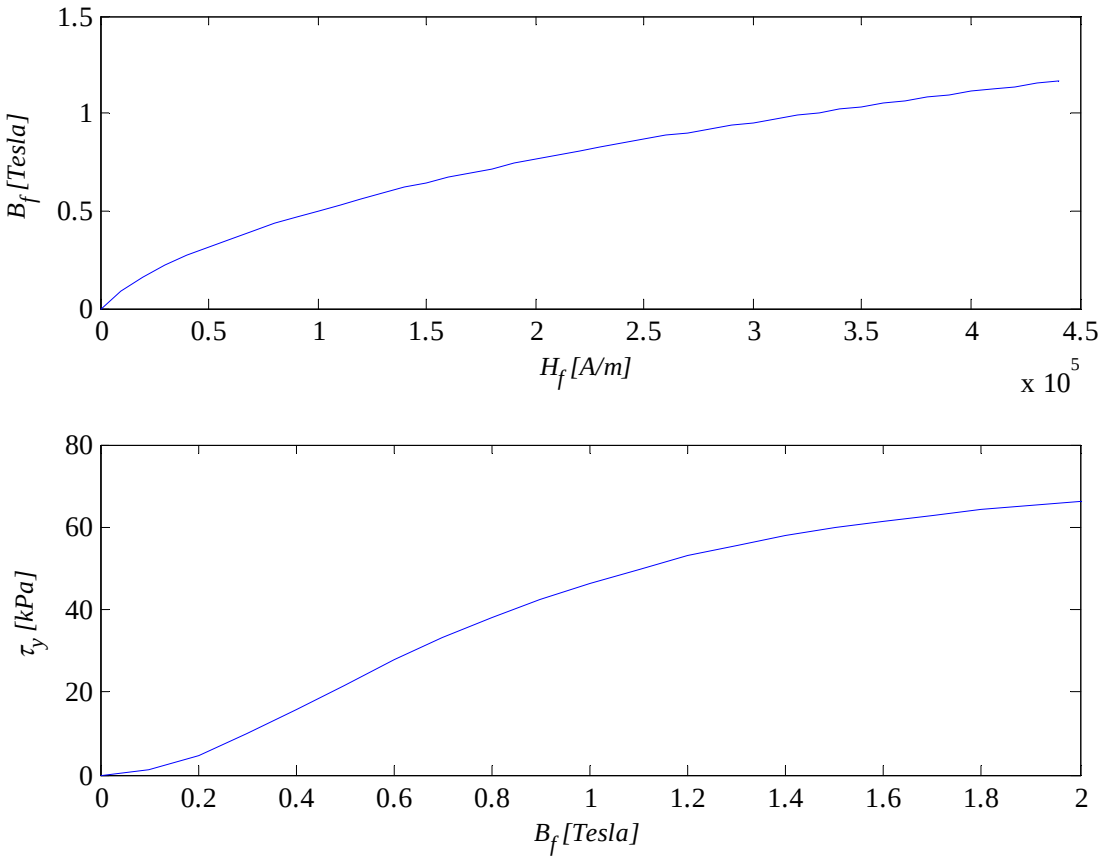

Figure 3-23: Magnetic properties of GM Corp. formulated MRF 13MAG098.

Table 3-3: Properties of GM Corp. formulated MRF 13MAG098.

Fluid Parameter	Value
Percent Solids (by volume)	30 %
μ_f	0.173 Pa·s
ρ_f	2910 kg/m^3

It is important to note that flux saturation is also an issue when simulated magnetic circuits. Since $B = \varphi / A$, the maximum B for each effective area of the valve design was checked each iteration of the optimization algorithm and the flux was reduced in accordance with the saturation limits of the core material of about 2.25 Tesla (Figure 3-21).

The final valve design parameters are illustrated in Table 3-4. The resulting gain on current, K_{MR}, as shown in equation (3.46) with c_{MR} = 2.2 is plotted versus current in Figure 3-25. Saturation of the valve occurs at approximately 1 A. This gain assumes steady state conditions in the valve.

Table 3-4: MR valve design parameters.

Design Parameter	Value
D_o	24.1 mm
D_i	9.7 mm
g	5 mm
t	15 mm
w	15 mm
L_c	15 mm
Wire gauge	26
N	579 turns
c_{MR}	2.2

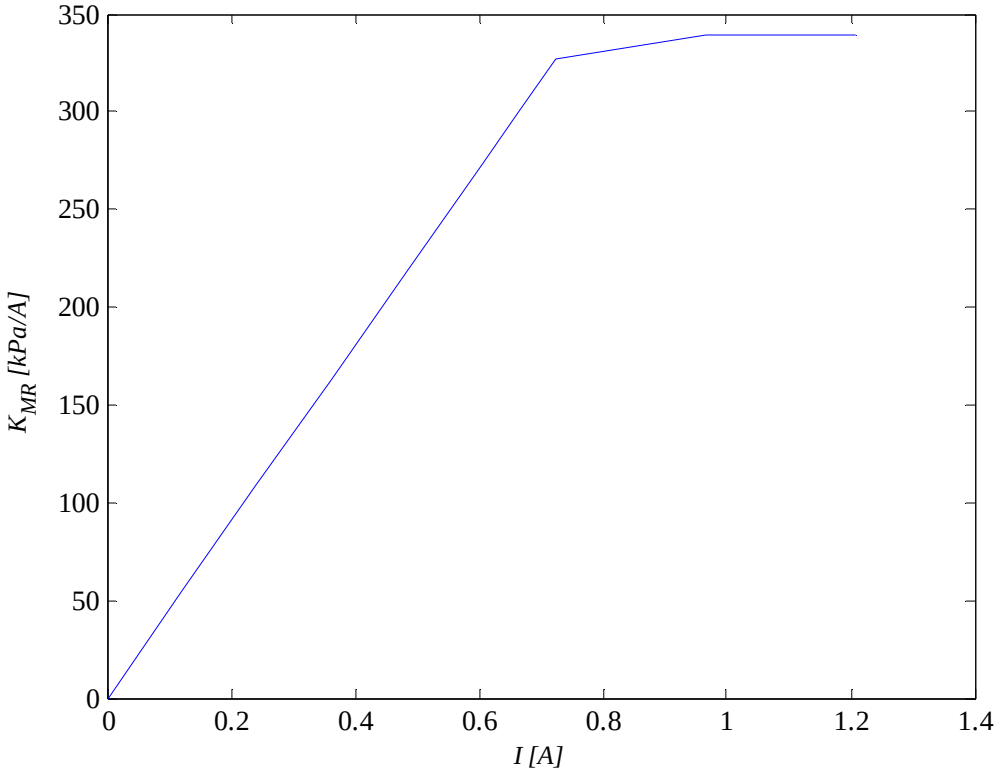

Figure 3-24: Valve gain K_{MR} versus input current I.

3.3.2 MR Bushing Dynamic Modeling

Writing the continuity equations of a hydraulic bushing we have

$$\dot{P}_1 = \frac{1}{C_1}(-Q + A_p \dot{z}) \tag{3.51}$$

$$\dot{P}_2 = \frac{1}{C_2} Q \tag{3.52}$$

where A_p is the effective pumping area, C_1, C_2, P_1 and P_2 are compliances and pressure in the upper and lower chambers respectively and Q is the flow rate in the inertia track. The equation for pressure driven flow through the inertia track is

$$P_1 - P_2 = L\dot{Q} + R_f Q + K_{MR} I(t) \tag{3.53}$$

where K_{MR} is a gain on input current *I(t)* producing a magnetorheological damping pressure drop. The parameters of the above hydraulic equations are

$$R_f = \frac{128\pi\mu_f l}{d_h^{\,4}}, \quad L = \frac{4\rho_f l}{\pi d_h^{\,2}} \tag{3.54}$$

where μ_f is the fluid viscosity, ρ_f is the fluid density, and d_h is the hydraulic diameter of the inertia track. The resistance, R_f, is a linear approximation adequate for the purposes of the model.

Using equations (3.51) to (3.53), the force transmitted through the bushing in the laplace domain is as follows:

$$F_T(s) = \left[K_r + B_r s + \frac{A_p^2}{C_1} \frac{s^2 + R_f/L\, s + 1/LC_2}{s^2 + R_f/L\, s + C/L} \right] Z(s) + \left[\frac{A_p K_{MR}/LC_1}{s^2 + R_f/L\, s + C/L} \right] I(s) \tag{3.55}$$

where

$$C = 1/C_1 + 1/C_2 \tag{3.56}$$

Neglecting the MR effect and the rubber damping, the dynamic stiffness is found to be:

$$K_{dyn}(s) = \frac{F_T(s)}{Z(s)} = \left[K_r + \frac{A_p^2}{C_1} \right] \frac{s^2 + 2\zeta_z \omega_z s + \alpha_\omega^{\,2} \omega_p^{\,2}}{s^2 + 2\zeta_p \omega_p s + \omega_p^{\,2}} \tag{3.57}$$

where

$$\omega_p = \sqrt{C/L}\,, \quad \zeta_p = \sqrt{R_f^{\,2}/4LC} \tag{3.58}$$

$$\alpha_\omega = \sqrt{\left(K_r + \frac{A_p^2}{C_1 + C_2} \right) \Big/ \left(K_r + \frac{A_p^2}{C_1} \right)} \tag{3.59}$$

The parameter α_ω is less than unity, and thus the frequency response of the bushing has a second order zero at ω_z followed by a second order pole at ω_p, where $\omega_z = \alpha_\omega \omega_p$. This is illustrated by the notch and peak in Figure 3-25. Least-squares curve fitting techniques were used to fit the pole, zero and gain in equation (3.57) to the experimental data. The experimental data in this figure was obtained from Ping Lee of General Motors, Canada and originated from a Cooper Standard rate machine.

Figure 3-25 illustrates the dynamic stiffness for two different amplitudes. As the input amplitude increases, the amount of damping increases. This nonlinearity was expected and is likely the cause of a quadratic damping (Kim & Singh, 1993). The solid lines in Figure 3-25 represent simulation results where the damping was assumed to be nonlinear.

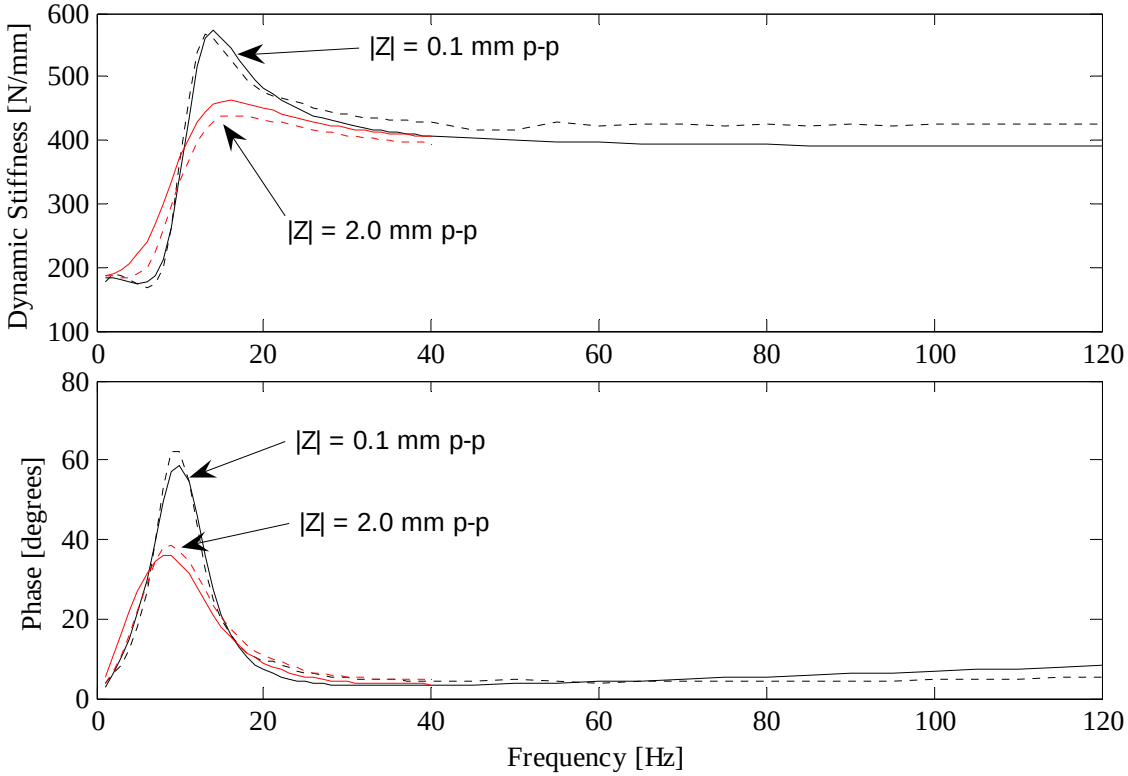

Figure 3-25: Dynamic stiffness of hydraulic bushing P/N 90576090 for 0.1 and 2.0 mm inputs (peak to peak). (solid – simulation, dotted – experimental)

Assuming bushing P/N 90576090 is similar to P/N 90575028, the inertia track and fluid properties are measured to be:

$$\begin{aligned} d_h &= 6.1\ mm \\ l &= 205\ mm \\ \rho_f &= 1040\ kg/m \\ \mu_f &= 0.029\ Pa \cdot s \end{aligned} \tag{3.60}$$

The least-square fitting technique yields the following remaining parameters:

$$\begin{aligned} K_r &= 172.8\ N/mm \\ B_r &= 0.073\ N \cdot s/mm \\ C_1 &= 32510\ mm^5/N \\ C_2 &= 514800\ mm^5/N \\ A_p &= 2634\ mm^2 \\ R_{f,0.1mm} &= 2.374 \times 10^8\ kg/m^4 \cdot s \\ R_{f,2.0mm} &= 4.465 \times 10^8\ kg/m^4 \cdot s \end{aligned} \tag{3.61}$$

Derived parameters are calculated to be:

$$\begin{aligned} \alpha_\omega &= 0.642 \\ \omega_z &= 7.861\ Hz,\ \ \omega_p = 12.252\ Hz \\ \zeta_{z,0.1mm} &= 0.435,\ \ \zeta_{p,0.1mm} = 0.279 \\ \zeta_{z,2.0mm} &= 0.819,\ \ \zeta_{p,2.0mm} = 0.526 \end{aligned} \tag{3.62}$$

Note that the predicted value of R_f based on equation (3.54) is much lower than the experimental values, in accordance with the expected nonlinear result.

$$\zeta_p = \sqrt{R_f^{\,2} / 4LC} \neq 0.279,\ or\ 0.526 \tag{3.63}$$

3.3.3 RMS Optimization of the Passive Bushing Parameters

Again, using the RMS optimization technique the performance of the passive bushing can be evaluated. Since the bushing has many parameters which affect its performance the focus will be on examining the RMS sensitivity to parameters which are pertinent to the cylinder-on-demand project and the MR bushing.

Selecting the inertia track length and hydraulic diameter is of interest since they can both be manipulated using actuators or MR valves. To study the affect of changing these parameters equation (3.64) is substituted into (3.55) with *I(s)* = 0.

$$\begin{aligned} l &= \kappa_1 l \\ d_h &= \kappa_2 d_h \end{aligned} \tag{3.64}$$

The RMS response is computed similar to previous studies on the linear and cubic nonlinear isolator; however, the frequency range is increased to 0-100 Hz for the hydraulic bushing application. The result for base excitation with an effective engine mass of 80 kg is illustrated in Figure 3-26, assuming that the parameters of equation (3.64) vary the fluid inertia and resistance according to the linear relationships developed in equation (3.54) resulting in the scaling:

$$L = \frac{\kappa_1}{\kappa_2^{\,2}} L, \;\; R_f = \frac{\kappa_1}{\kappa_2^{\,4}} R_f \tag{3.65}$$

The dotted lines represent lines of constant inertia track length and the solid curves are lines of constant hydraulic diameter. The RMS response of the nominal, purchased mount is marked at $\kappa_1 = 1$ and $\kappa_2 = 1$ by a circle (Figure 3-26). Decreasing the inertia track length decreases both *R* and η for a given hydraulic diameter. It seems from this result that the hydraulic diameter of this isolator is optimal since it minimizes the acceleration due to base excitation for the range of inertia track lengths considered.

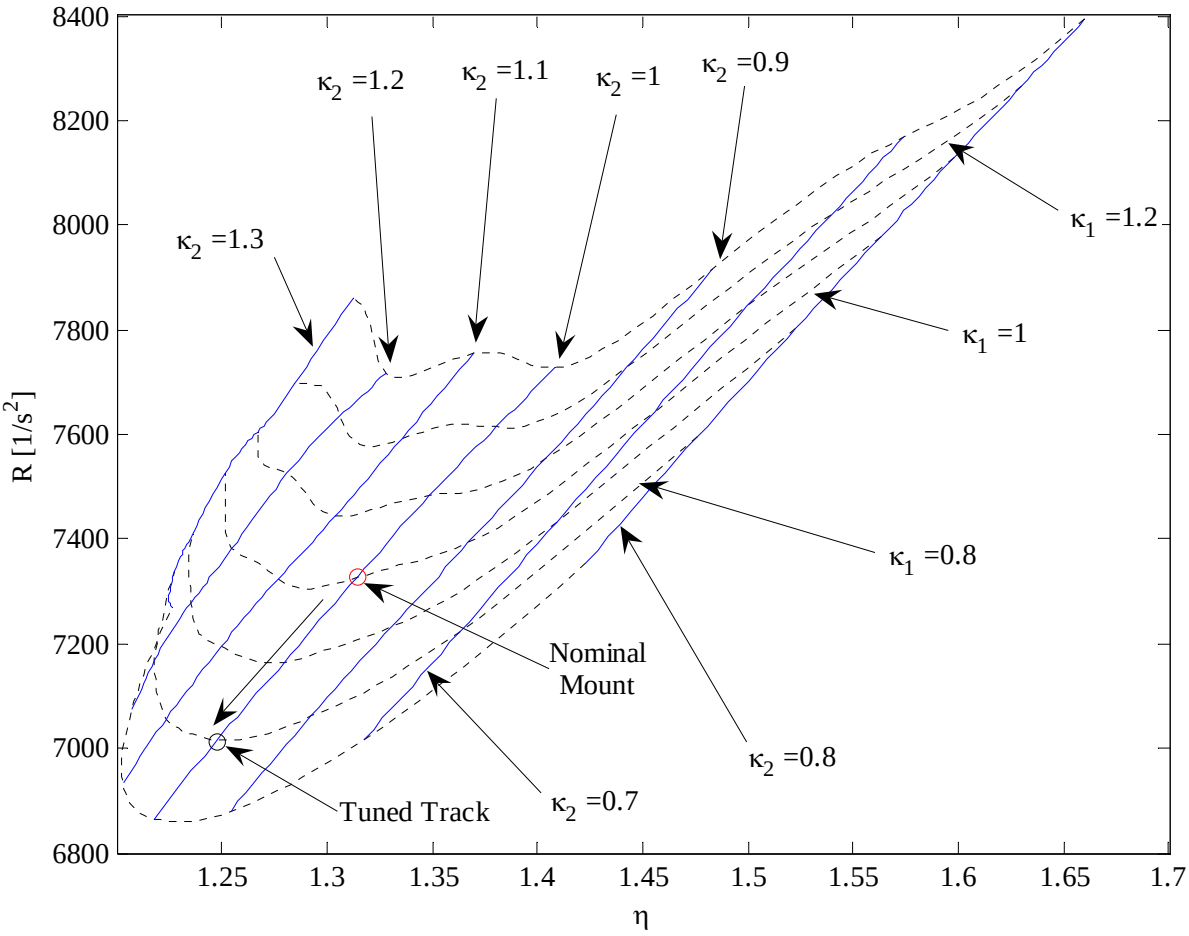

Figure 3-26: Base excitation RMS optimization of the inertia track parameters (solid – constant d_h; dotted – constant l; circles - nominal mount and tuned inertia track, as indicated).

Figure 3-27 illustrates the RMS response of the isolator given a harmonic force input similar to that discussed in section 3.1.1. This result illustrates that although the nominal mount is nearly optimal, it could be improved for example by reducing inertia track length 20 %, indicated in Figure 3-26 by $\kappa_1 = 0.8$. The corresponding change in the dynamic stiffness is illustrated in Figure 3-28.

This change would reduce R by approximately 4.4 % and η by 5.1 %. There would also be a 12 % decrease in ϕ at the cost of a 0.7 % increase in γ. The frequency response of the forced bushing is illustrated in Figure 3-29 and Figure 3-30.

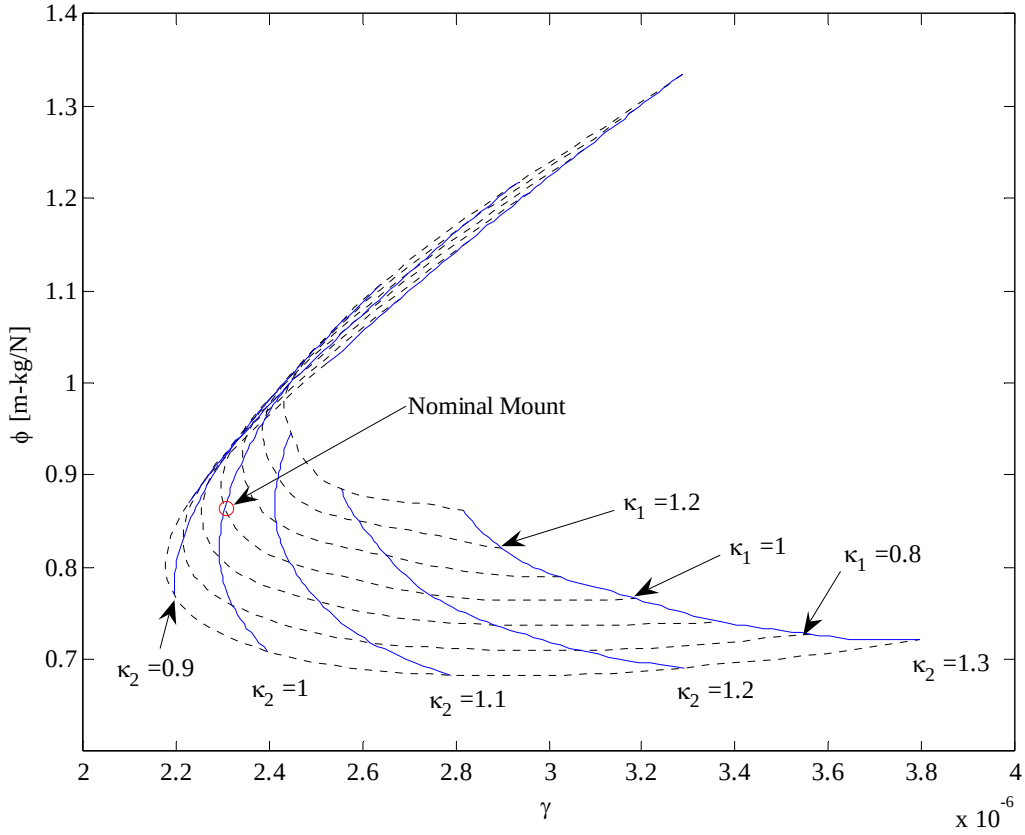

Figure 3-27: Harmonic forced RMS optimization of the inertia track parameters (solid – constant d_h, dotted – constant l, circle - nominal mount).

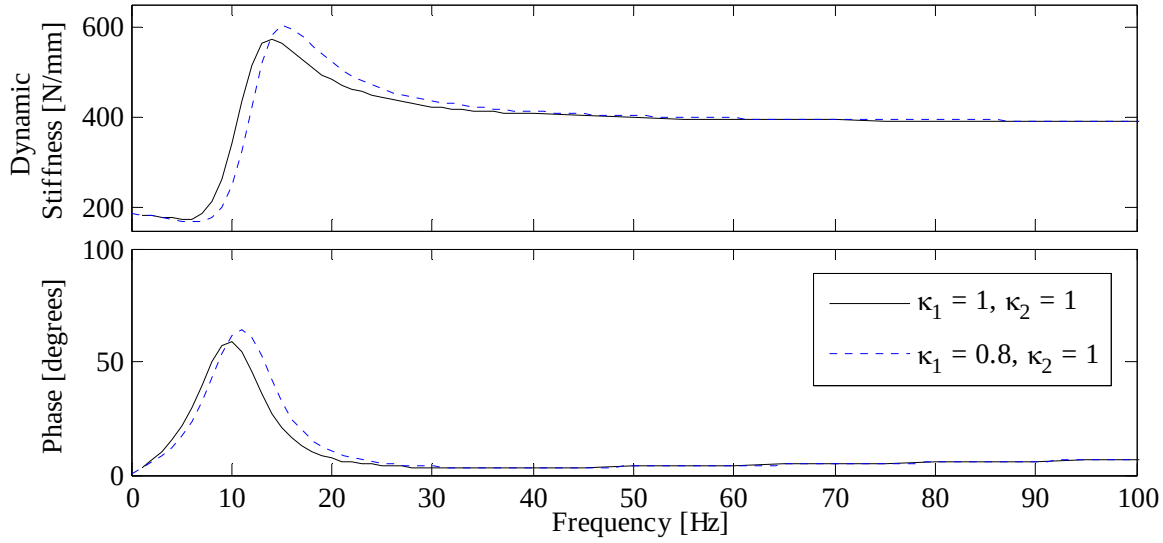

Figure 3-28: Dynamic stiffness given a 20% decrease in inertia track length.

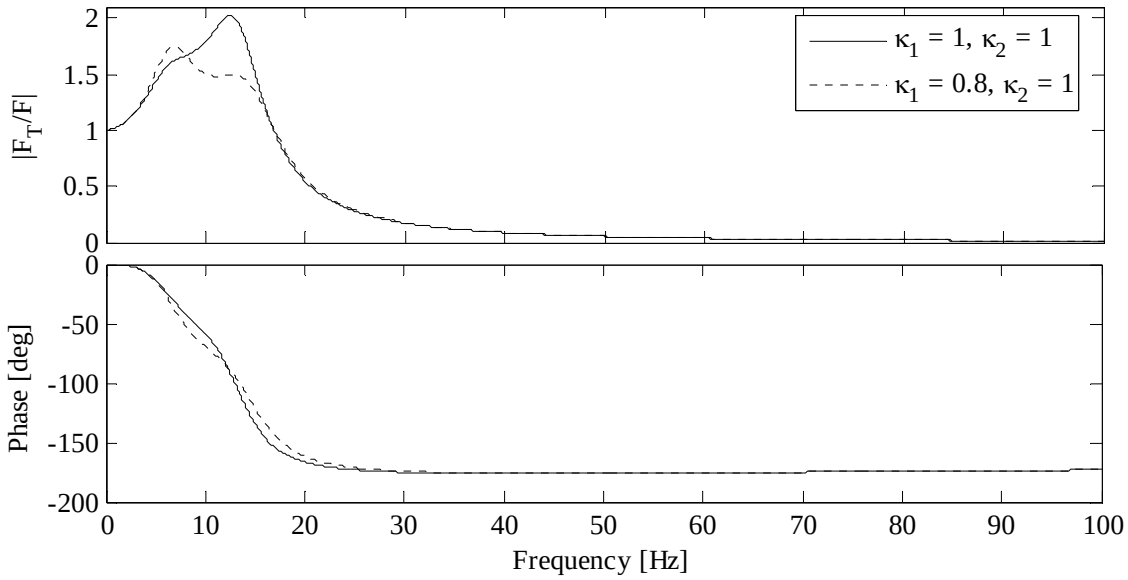

Figure 3-29: Reduction in transferred force given a 20% decrease in inertia track length.

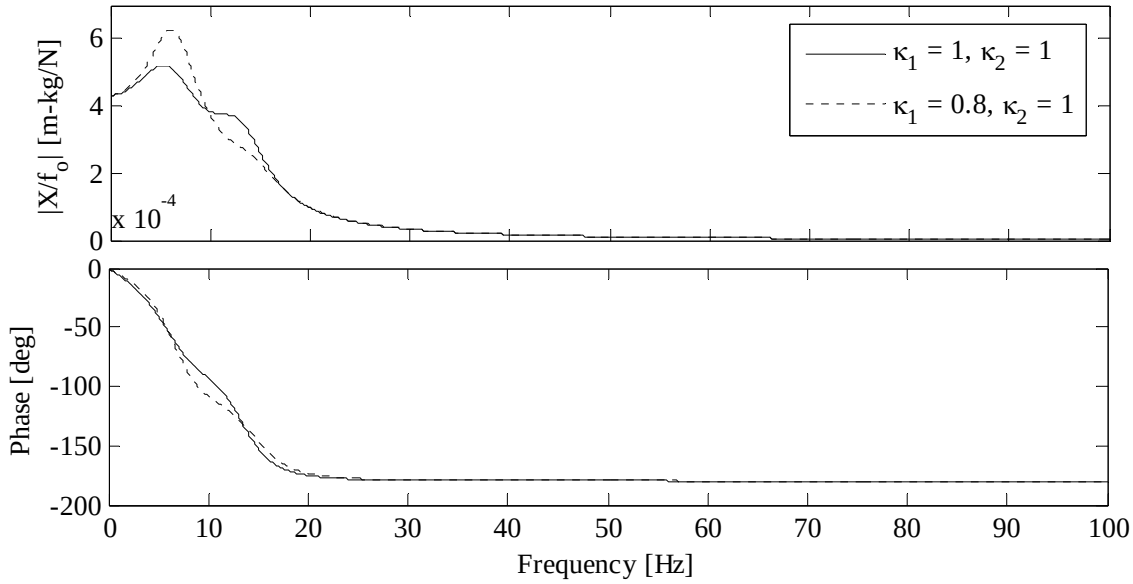

Figure 3-30: Increase in displacement given a 20% decrease in inertia track length.

This study illustrates that the RMS optimization techniques could be helpful in designing the inertia track. Moreover, while the decrease in the inertia track seems have much better low frequency isolation properties, if the engine forcing magnitude increases during cylinder deactivation it may be beneficial to decrease the length of the inertia track to decrease the force transmitted to the chassis at a relatively low cost of increased forced engine displacement.

Similar to the inertia track study, considering the substitution of equation (3.66) into the bushing dynamic stiffness, the parameters β_1 and β_2 can be varied to scale the nominal pumping chamber parameters A_p and C_1, respectively.

$$\begin{aligned} A_p &= \beta_1 A_p \\ C_1 &= \beta_2 C_1 \end{aligned} \tag{3.66}$$

These parameters are of interest since the value of both the compliance, C_1, and pumping area, A_p, have an affect on the dynamic stiffness beyond the notch frequencies. Neglecting rubber damping in equation (3.57), the high frequency stiffness of the mount is:

$$K_{dyn}(\omega) \approx K_r + \frac{A_p^2}{C_1} \tag{3.67}$$
$$\omega \gg \omega_p$$

Although pumping area is difficult to control in an active mount application, a valve directing fluid to a more compliant chamber or an actuator exerting force could be used to control the pumping chamber effective compliance.

The effect of β_1 and β_2 on the RMS response of the bushing to base and forced excitations is illustrated in Figure 3-31 and Figure 3-32.

The RMS study results in Figure 3-31 and Figure 3-32 illustrate that the mount parameters are not exactly optimum, although there is a direct trade off in improving base excitation acceleration and harmonic force excitation transmitted force. This is illustrated by decreasing pumping area and compliance by factors of $\beta_1 = 0.9$ and $\beta_2 = 0.6$. They would result in a 16 % increase in *R* and a 12 % decrease in ϕ. This change would also yield a decrease of RMS displacement due to both inputs by 5.4 % in η and 1 % in γ.

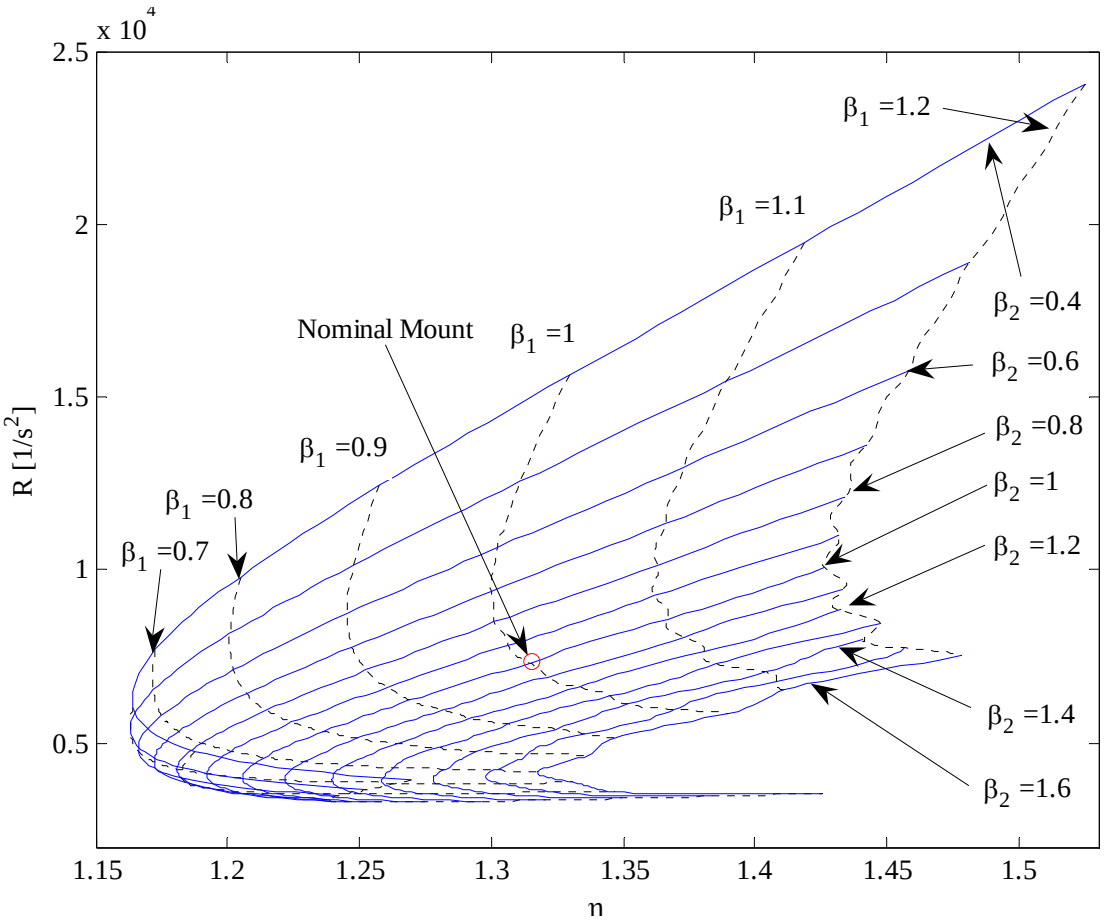

Figure 3-31: Base excitation RMS optimization of the pumping chamber parameters (solid – constant C_1, dotted – constant A_p, circle - nominal mount).

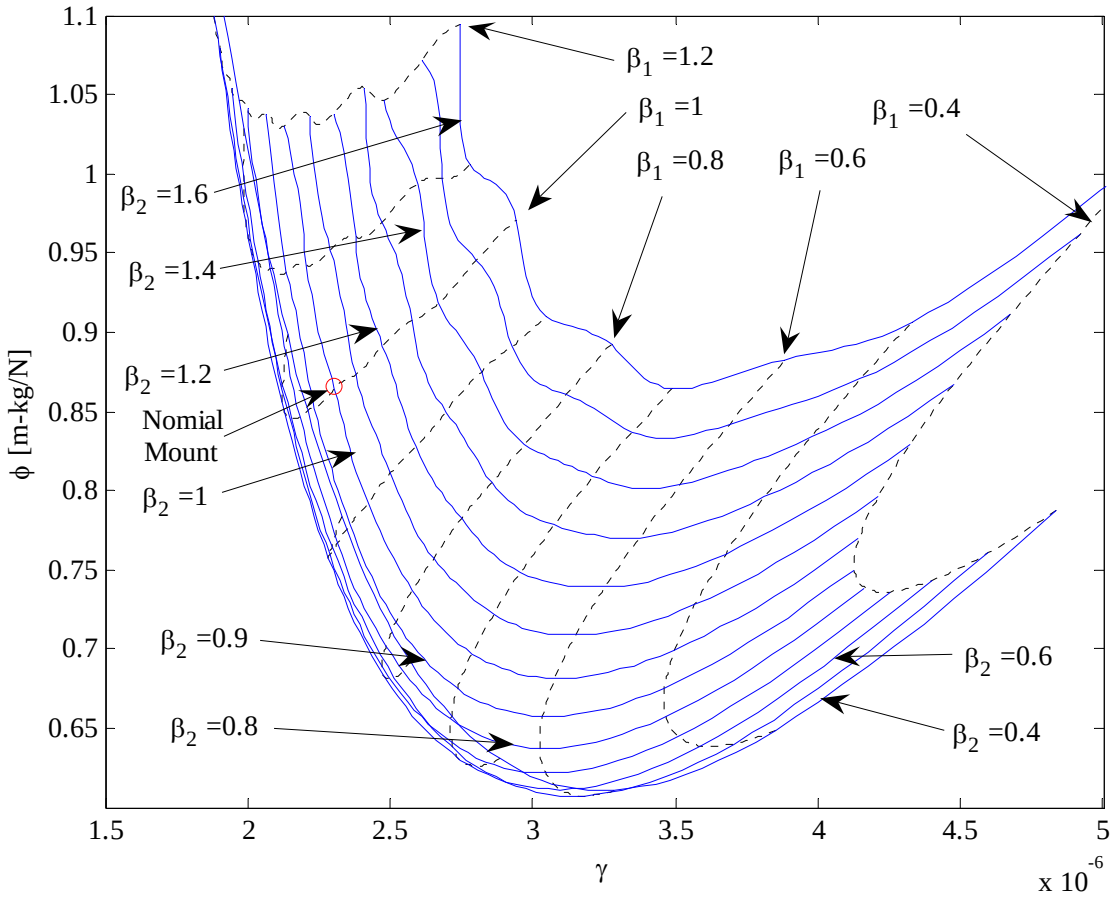

Figure 3-32: Harmonic forced RMS optimization of the pumping chamber parameters (solid – constant C_1, dotted – constant A_p, circle - nominal mount).

3.3.4 MR Bushing Simulation

With the known physical parameters of the standard hydraulic bushing and the property values of the MRF, a numerical simulation of the MR bushing performance can be produced. The only parameters that change are the fluid viscosity and density, which change the fluid inertia in the track and the resistance.

Using the fluid properties in Table 3-3 and valve inertia track parameters in Table 3-4 the model parameters are recalculated. A major assumption is that the damping occurring in the MR bushing is linearly proportional to the experimentally measured damping in equation (3.62); however, the cost of this assumption is assumed to be minimal since it is expected that the damping ratio is relatively high and its affect on the frequency response is somewhat saturated. It is of more interest to predict the

notch frequencies of the bushing as well as the effect of the magnetic field in the inertia track. The predicted MR bushing lumped parameters are summarized in Table 3-5.

The dynamic stiffness simulation result using the estimated parameters in Table 3-5 is illustrated compared to the purchased GM bushing in Figure 3-33. The notch frequencies of the MR bushing are low and approach the minimum frequency achievable experimentally in the test facilities available (5 Hz). Figure 3-33 also demonstrates the simulated dynamic stiffness of the purchased bushing where the fluid has been substituted for MRF 13MAG098. This simulation shows that the dynamic stiffness of the MRF-filled purchased mount would be highly damped and the notch frequencies are increased slightly.

Table 3-5: Simulation MR valve dynamic stiffness pole and zero properties.

Parameter	Value
ω_z	5.931 Hz
ω_p	9.244 Hz
ζ_z	1.465
ζ_p	0.94

The sum of force on a fluid element in the inertia track is

$$\sum \vec{F} = \left(P_1 - P_2 - R_f Q\right) A_i \tag{3.68}$$

where A_i is the cross-sectional area. If this force is greater than the semi-active force produced by the MR effect, then flow occurs in the inertia track. Otherwise, the MR effect prevents flow from occurring as shown in equation (3.69).

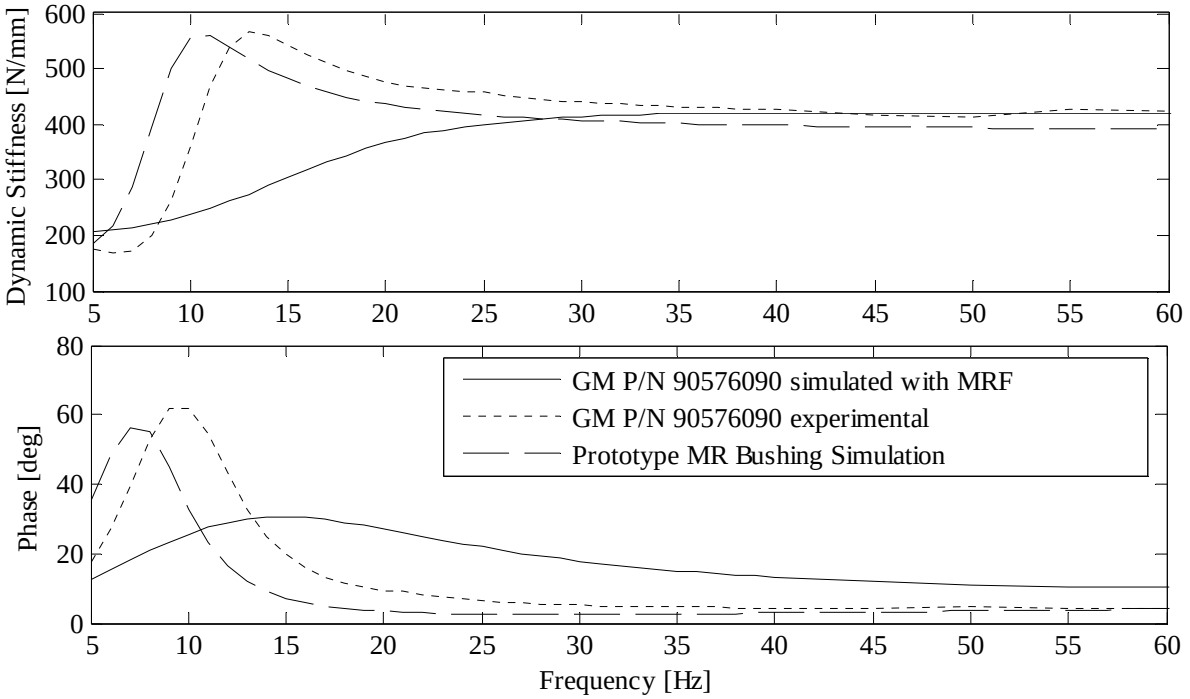

Figure 3-33: Prototype MR bushing simulation and purchased bushing filled with MRF simulation compared to the purchase bushing experimentally measured dynamic stiffness.

$$\begin{aligned} \left|\left(P_1 - P_2 - R_f Q\right) A_i\right| &< K_{MR} I A_i \rightarrow Q = 0 \\ \left|\left(P_1 - P_2 - R_f Q\right)\right| &< K_{MR} I \rightarrow Q = 0 \end{aligned} \tag{3.69}$$

This is illustrated in Figure 3-34, where initially at t = 1 s, the MR effect due to a 0.1 A current is as large as the pressure induced in the pumping chamber at 1 mm amplitude of displacement and very little flow results. At higher frequencies, t > 2 s, the simulated pressure drop due to the MR valve is small and the flow rate increases.

Furthermore, Figure 3-35 illustrates the response of the bushing with a much larger pressure drop across the value with I = 0.4 A. At this amplitude of vibration, the pressure drop across the valve is predicted to be large enough to prevent flow in the inertia track.

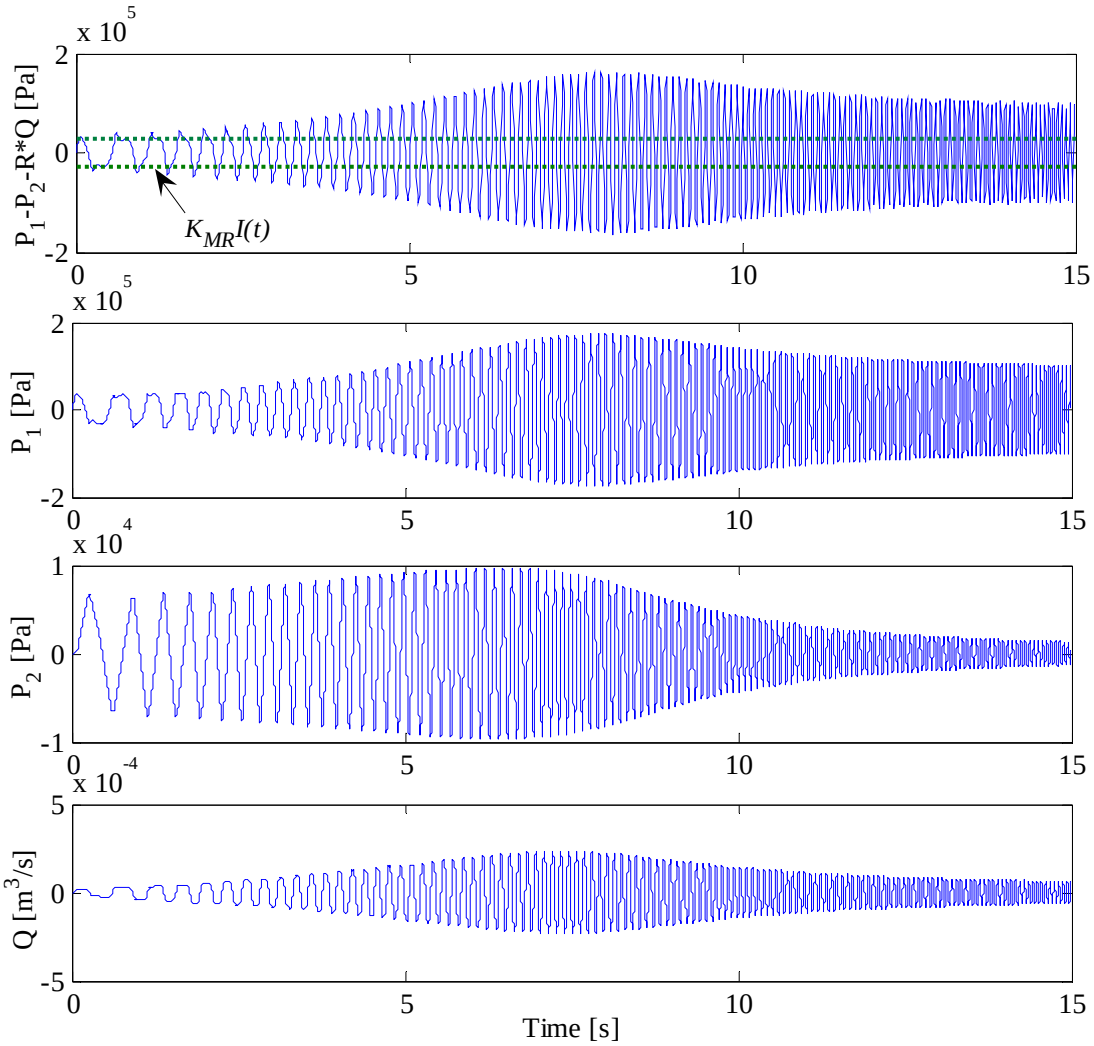

Figure 3-34: Simulation time domain response of the chamber pressures, inertia track flow rate and hydraulic pressure drop versus the MR effect (dotted line in the top axes) for *I* = 0.1 A, *Z* = 1 mm (2 mm peak to peak).

The introduction of the semi-active force results in a highly nonlinear relationship. For example, if the amplitude of vibration was doubled to Z = 2 mm, which is not an unreasonable amplitude of vibration, the pressure in the pumping chamber would double and flow would result with an input current of I = 0.4 A.

With the nonlinearity in mind, the simulated frequency response of the bushing is presented in Figure 3-36. The limiting effect of increasing current is to eliminate flow through the valve, as illustrated in the case of Z = 1 mm, I = 0.3 A. This effectively reduces the mount to a single degree

of freedom systems with constant stiffness. Otherwise, increasing the current increases the low frequency stiffness by reducing flow through the inertia track; therefore, having the effect of decreasing the notch frequency of the bushing.

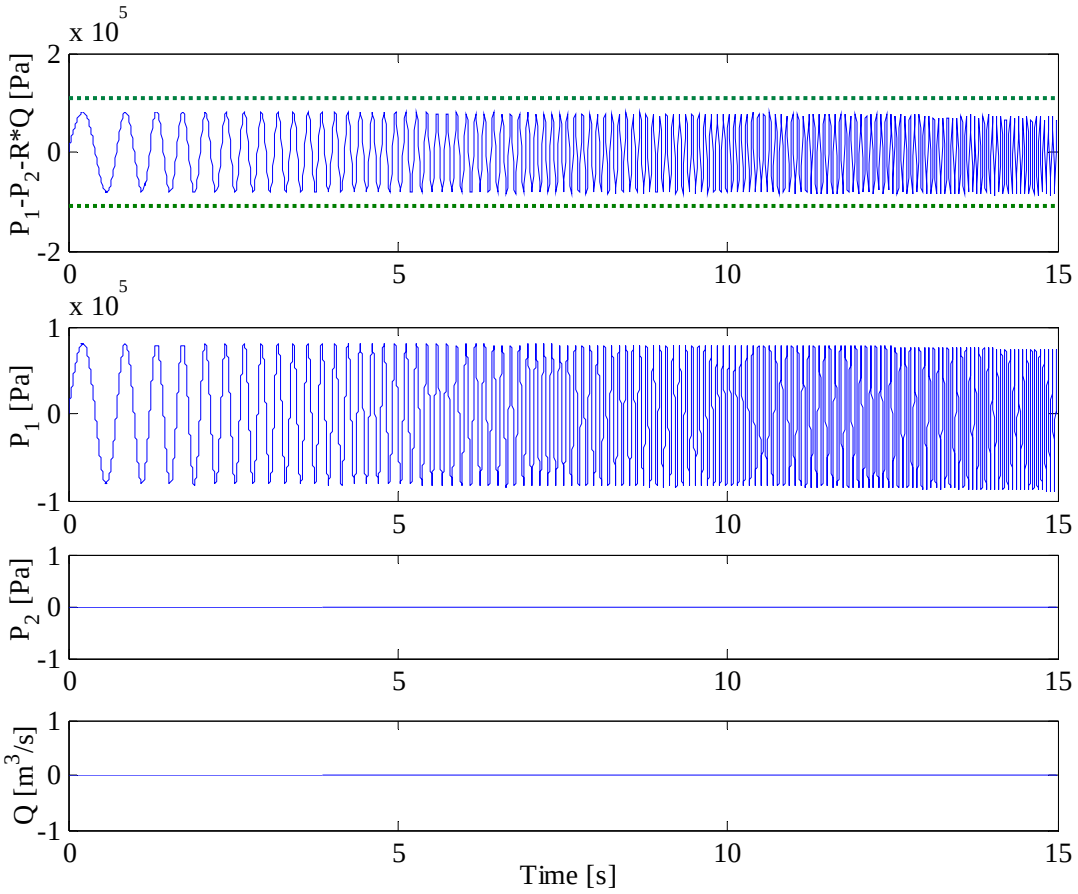

Figure 3-35: Simulation time domain response of the chamber pressures, inertia track flow rate and hydraulic pressure drop versus the MR effect (dotted line in the top axes) for *I* = 0.4 A, *Z* = 1 mm (2 mm peak to peak).

The frequency domain result of the nonlinear MR bushing was generated using an ODE 45 solver to numerically obtain the solution to the state space equations. A zero cross-over algorithm was implemented to monitor the direction of the force vector on the element of fluid in the inertia track and change the sign of the MR force appropriately. This algorithm avoided singularity issues in the numerical solver by automatically truncating the solution at a cross-over point then restarted the solver with the appropriate MR force sign and the initial conditions equal to the final conditions of the previous solution. The FRF was computed from the time domain solution.

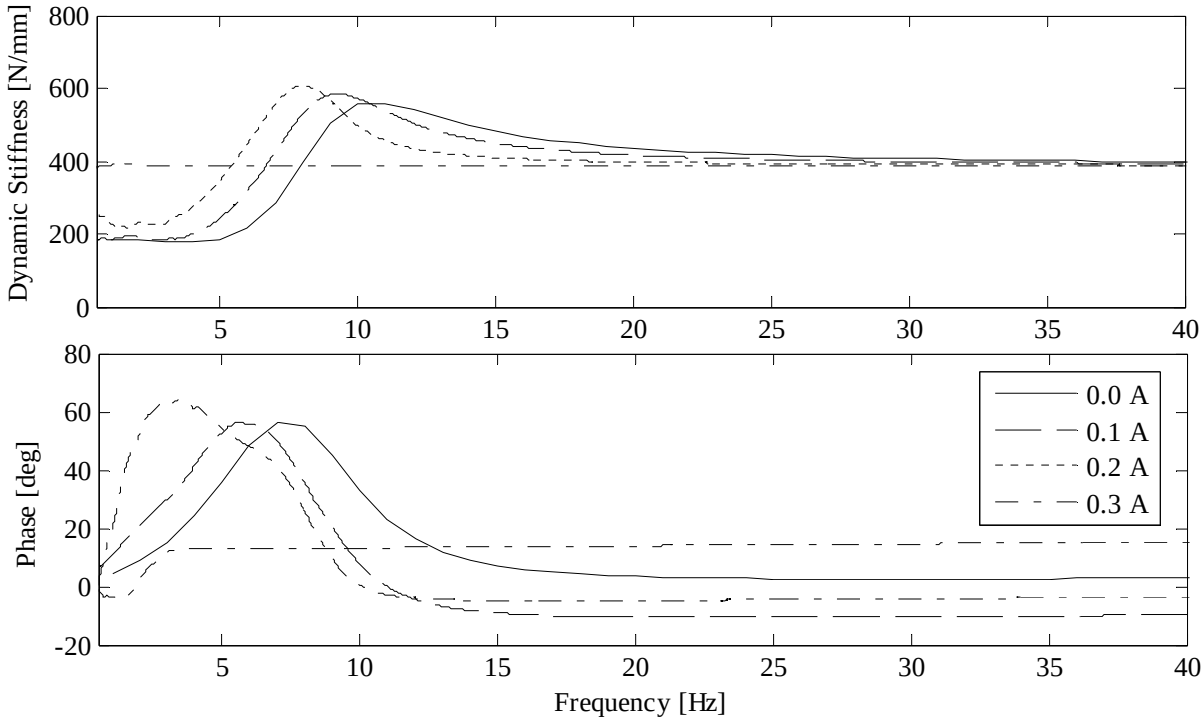

Figure 3-36: MR Bushing dynamic stiffness simulation results for various current inputs and *Z* = 1 mm (2 mm peak to peak).

As mentioned in the previous section, changing the bushing compliance could also be a potential mechanism for changing the dynamic stiffness. Given the current bushing configuration (P/N 90575028), increasing the pumping compliance by a factor of 4 has a significant effect on the dynamic stiffness, as illustrated in Figure 3-37.

Increasing the pumping chamber compliance is advantageous since it provides 50 % of the dynamic stiffness above 20 Hz; however, a similar result could be achieved by placing the off state notch frequency of the bushing at high frequency, thus being soft below the notch for the 3-cylinder mode then increasing the current to lower the notch as demonstrated in Figure 3-37 to ~12 Hz, to provide the state for 6 cylinder mode.

The most critical issue with using semi-active technology to switch a bushing from high compliance (off-state) to low compliance is the potential for failure. If a failure occurs, high compliance would result in extremely high amplitude responses as illustrated in Figure 3-38.

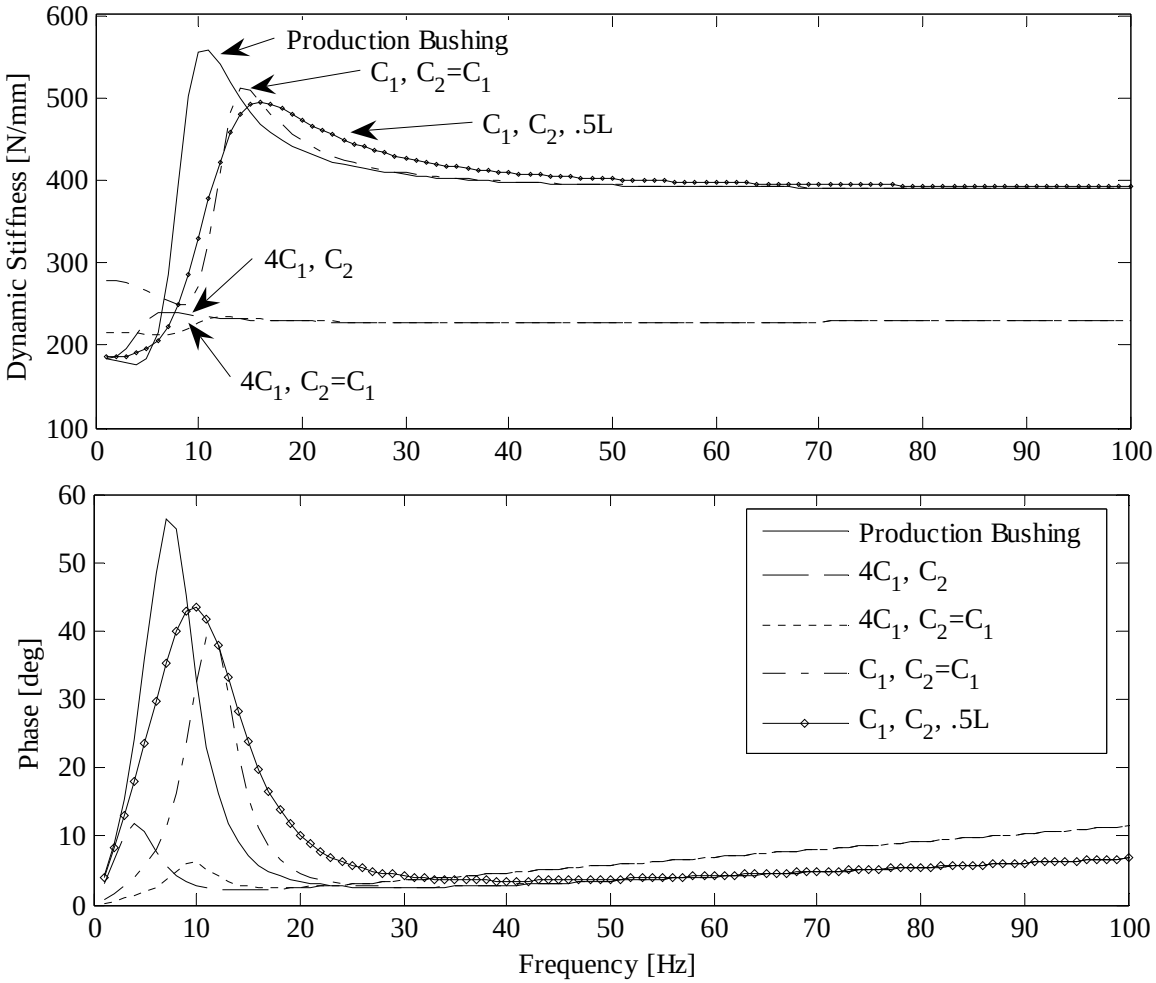

Figure 3-37: Effect of changing fluid inertia and compliance on the bushing dynamic stiffness.

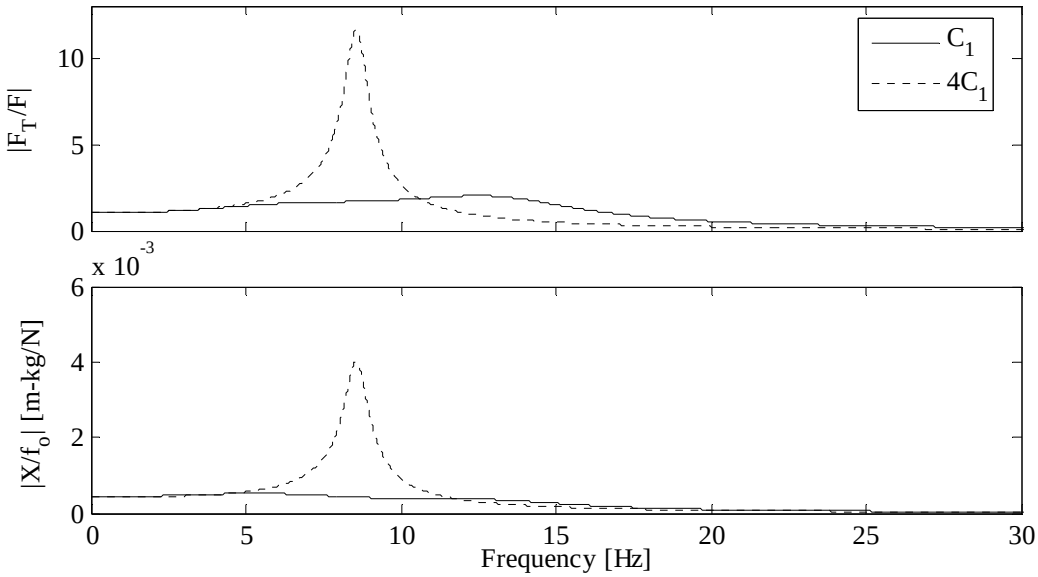

Figure 3-38: Effect of increasing compliance the forced response.

3.4 Summary

Section 3.1 develops the equations of the RMS force transmitted through the linear isolator for both harmonic forcing and unbalance forcing. These values are plotted for various stiffnesses and damping ratios versus the RMS displacement due to these inputs. The end result is that, similar to the base excitation result presented in Chapter 2, optimum values of damping can be selected for a given stiffness. The line of optimum values are plotted in Figure 3-14 for the three cases under study: base, harmonic forced, and unbalance excited systems. Base and unbalance systems are found to share optimum damping ratios. Semi-active control may be used to shift the damping from one line of optimum to the other depending on the input at a given time, for example when the engine deactivates or activates cylinders.

The base excitation cubic nonlinear system RMS optimization illustrated in Chapter 2 is applied to the harmonic forced input. A brief study of the stability of the systems illustrated that there are issues introduced due to the nonlinearity; however it is assumed that the equilibrium states are mechanically unachievable (physical displacement and energy level limitations). The forced result yields similar RMS performance to the base excitation result previously found by Narimani (2004) where negative

stiffness significantly decreases both force and displacement transmitted. Finally, a transient simulation analysis reveals that the negative damping has no significant impact on the step and impulse inputs; hence the linear damping and stiffness could be selected for optimum time domain performance and the cubic stiffness added to tune the frequency response.

A further extension of the RMS optimization technique is achieved by tuning the hydraulic bushing inertia track length and hydraulic diameter as well as the pumping area and pumping chamber compliance. For the given bushing and engine mass it was found that decreasing the inertia track length by 20% would offer the best improvement in the frequency response since it would decrease both absolute acceleration and force transmitted with negligible increase in the RMS of displacement.

The next sections of this chapter deal with MR valve design and simulation of the MR bushing with the MR valve replacing the inertia track. The result illustrates that as the current is increased the bushing tends to a single degree of freedom as fluid flow is decreased. At high currents, flow does not occur and the dynamic stiffness is constant with very little damping. This mechanism could be used by increasing the notch frequency of the bushing and using the current to change the low frequency stiffness.

As an alternative to the MR bushing design, it is suggested that changing the pumping chamber compliance may an effective way to produce a large variation in dynamic stiffness. The case presented in Figure 3-37 illustrates that an increase in compliance by a factor of 4 decreases the stiffness by roughly 50%.

Chapter 4
Experiment Implementation

In previous chapters, the RMS optimization of the frequency response of a linear single degree of freedom isolator was discussed and developed for three elemental inputs: base, unbalance and harmonic forcing excitation. An experiment was designed to test the practical effectiveness of these methods on a real system.

This chapter also describes the apparatus used to measure the dynamic properties of the hydraulic bushing (P/N 90575028) provided by General Motors Corp. as well as the prototype MR hydraulic bushing. A fixture was designed to accommodate rate experiments used to determine dynamic stiffness as well as the base excitation of both the purchased and prototype bushings.

4.1 Linear RMS Optimization Experiment

The experimental apparatus, shown below in Figure 4-1, represents a SDOF oscillator. The two springs in parallel amount to a combined stiffness of k = 770.6 N/m. The total suspended mass is approximately m = 0.45 kg, and thus the linear natural frequency is approximately f_n = 6.6 Hz. Damping is produced using an air dashpot, manufactured by Airpot, model 2KS325. This damper has internal friction coefficient of about 0.2 (assuming no side load) and has a manually adjustable damping coefficient from c = 0 to 7 N-s/mm.

The displacement of the mass is measured by the coordinate x and the displacement of the base (shaker) is y. The relative displacement, z , similar to Figure 2-1 represents the deflection of the spring and dashpot. The states d^2x/dt^2, dy^2/dt^2, and z are measured using two Dytran accelerometers, model 3145AG LIVM, and a RDP Electronics LDC500C DC LVDT, respectively.

An LDS V722 shaker was used to generate the inputs, acceleration feedback controlled via the Dactron SpectraBook and Dactron Shaker Control software. The LDS V722 shaker is capable of delivering 951 m/s^2 of acceleration (bare table) from 5 to 4000 Hz.

Figure 4-1: Single degree of freedom isolator experiment apparatus mounted on the LDS V722 shaker.

The equation of motion of the system illustrated in Figure 4-1 is

$$m\ddot{x} + c\dot{x} + kx = F(t) + c\dot{y} + ky \tag{4.1}$$

Neglecting the force applied directly to the mass, *F(t)*, equation (4.1) can be rearranged and non-dimensionalized to the following form:

$$\ddot{z} + 2\xi\omega_n\dot{z} + \omega_n{}^2 z = -\ddot{y} \tag{4.2}$$

Now, with respect to the inertial frame, forcing on the mass becomes the acceleration input and a coordinate transformation yields equation (4.3).

$$-\ddot{y} = \frac{F(t)}{m} = f_o \cos(\omega_{dr} t) \tag{4.3}$$

$$z \to x \tag{4.4}$$

$$\ddot{x} + 2\xi\omega_n \dot{x} + \omega_n{}^2 x = F(t)/m \tag{4.5}$$

Hence, rather than directly applying a force to the mass, the frame can be accelerated to apply an inertial force as illustrated in Figure 4-2. This is applicable to the experiment since the shaker can only produce controlled displacement.

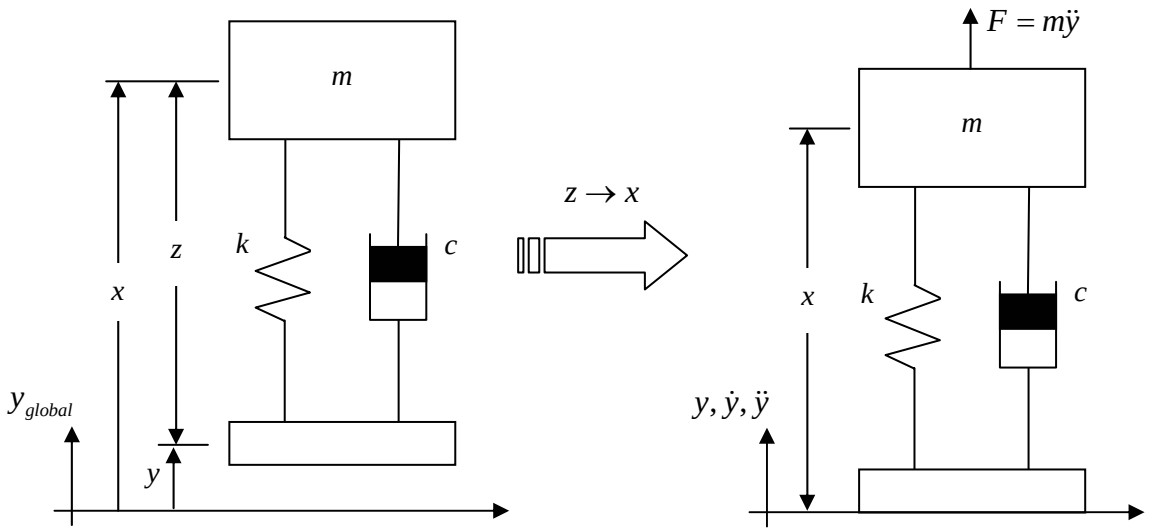

Figure 4-2: An inertial force can be applied to the suspended mass by accelerating the reference frame attached to the base of the isolator.

The RMS response of the base excitation experiment is produced with a constant displacement amplitude sweep over the frequency range. Constant displacement amplitude frequency sweep produced an acceleration loading

$$\left|\ddot{Y}\right| = Y\omega_{dr}{}^2 \tag{4.6}$$

where ω_{dr} is the driving frequency. Hence, the base excitation experiment doubles as an unbalance excitation experiment.

Similarly, the harmonic forcing excitation of the linear isolator can be produced by applying a constant displacement amplitude sweep over the frequency range.

The system illustrated in Figure 4-1 is not perfectly linear; however, with careful selection of the inputs the impact of nonlinearity may be minimized. The purpose of this discussion is to explain some of the nonlinear characteristics observed in a simple qualitative way.

As mentioned previously, the dashpot has a certain amount of friction. Friction

$$F_{friction} = F\,\mathrm{sgn}(\dot{z}) \tag{4.7}$$

also exists in the nylon bearing supporting the suspended mass. To the human hand, it is difficult to perceive this minute force; however, the LVDT is much more precise and detects the motion created as a result of small forces, as demonstrated in Figure 4-3. This figure illustrates that with low input amplitudes the inertia force applied to the mass is less than the friction until approximately 7 Hz during the forward sweep. Beyond 7 Hz, the mass breaks free and relative motion is observed.

The opposite effect is observed on the backward sweep since the inertia of the mass is greater than friction until approximately 6 Hz near the tail end of resonance. Experimentally, it was found that an amplitude of 2.25 mm was sufficient to overcome friction at 5 Hz regardless of the magnitude of damping ratio and sweep direction.

Furthermore, strong jump phenomena can be observed when the amplitude of vibration reaches the maximum with high damping. The result is a piecewise linear system, the dynamics of which are clearly nonlinear. This nonlinearity is avoided by reducing the input amplitude to avoid *saturating* the dashpot.

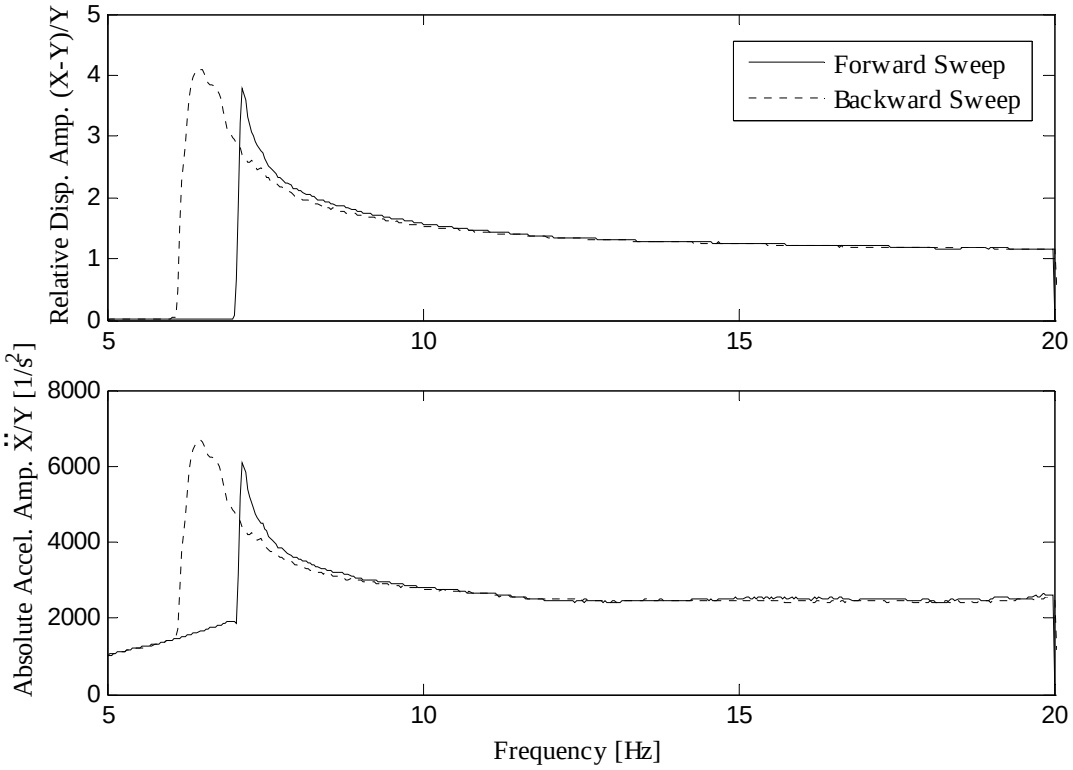

Figure 4-3: Friction causing jump phenomena during low energy frequency responses.

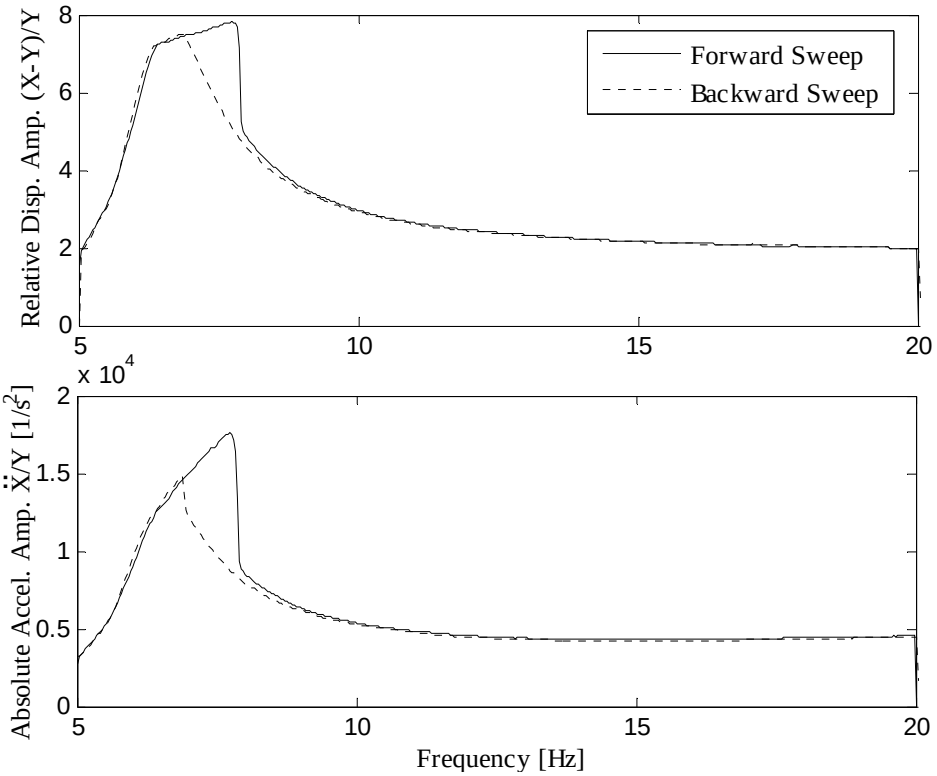

Figure 4-4: Piecewise nonlinearity as the dashpot reaches maximum displacement under high damping ratios

Once the linear limits of the system were defined, linear experimental results were reproducible as shown in Figure 4-5. In terms of reproducing the experimental results, Figure 4-5 also illustrates that as the damping adjustment bolt was changed at constant increments over 12 experiments, the actual damping did not change linearly. Figure 4-5 shows that essentially two groups of results were observed for high and low damping, rather than a smooth increase in damping ratio. Thus, the damping adjustment was finely tuned before each experiment trial while observing the response to a step input for improved control over the change in damping from trial to trail.

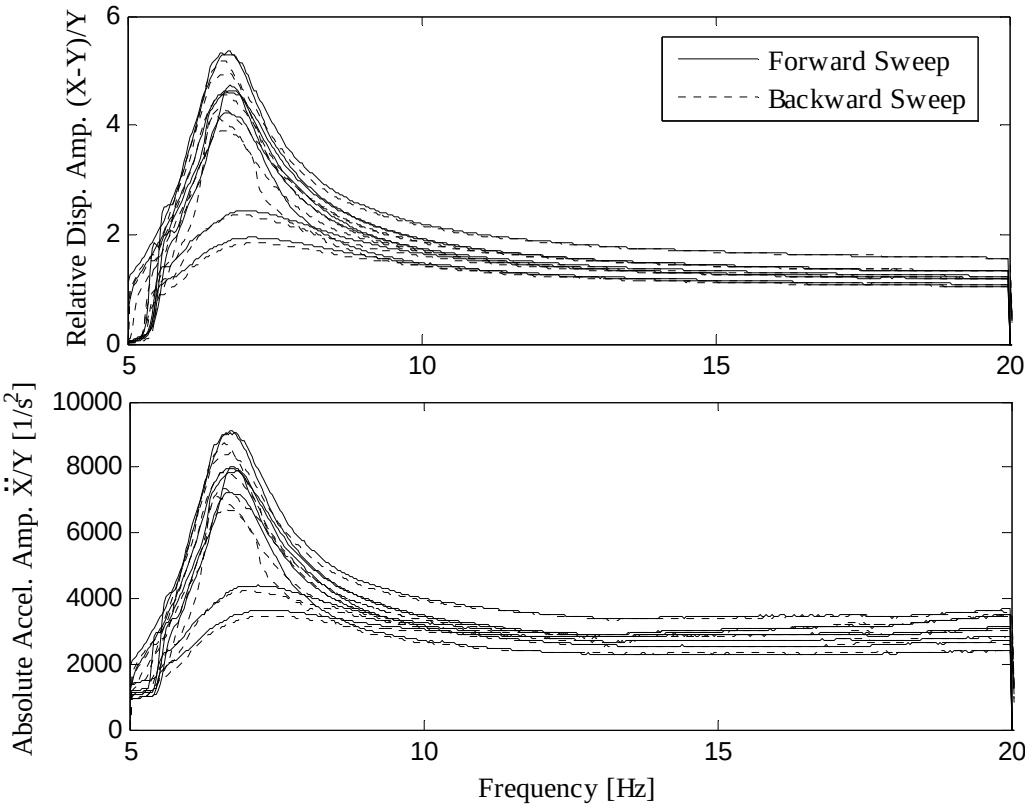

Figure 4-5: Preliminary results illustrating nearly linear experimental base excitation frequency responses.

4.2 Hydraulic Bushing Experiment

4.2.1 MR Valve Implementation

To implement the MR valve design proposed in the previous chapter, a casing has been designed to hold the rubber portion of the bushing (see Figure 4-6). This design allows experiments to be conducted on individual components of the bushing, if necessary.

Not that the pumping chamber in Figure 4-6 has compliance C_1 and the compliance chambers A and B are represented by C_2 in the hydraulic bushing model detailed in the previous chapter.

The casing acts as a manifold, with ports to the compliance and pumping chambers of the rubber bushing. Pressure may be measured at these ports to help identify certain properties of the mount. Furthermore, this casing permits the fluid to bypass the inertia track by blocking ports, blocking channels and redirecting flow. Figure 4-7 illustrates how the casing is combined with the prototype MR valve. The bushing inertia track is blocked and the flow of MRF is redirected through this module bolted to the side of the casing. The channel through the valve provides the fluid damping and also passes through a magnetic flux. The solenoid, not shown in Figure 4-7, which produces the flux is placed in the MR valve inside the aluminium ring in the centre of the valve.

The volumetric stiffness of the bushing can also be measured by blocking all of the ports and the inertia track of the bushing.

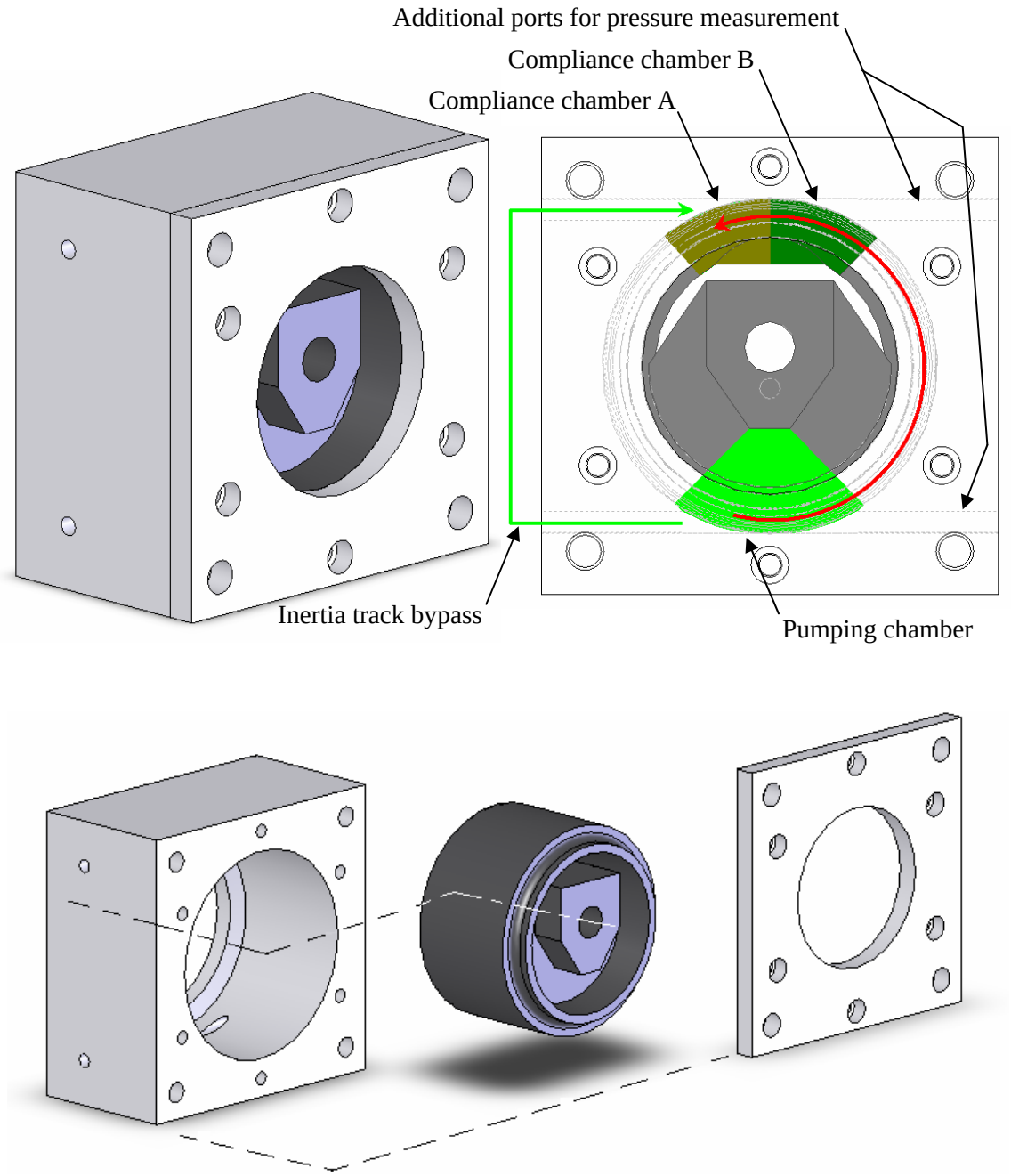

Figure 4-6: Hydraulic bushing casing to house the rubber purchased mount, with ports to allow bypassing the inertia track and of pressure measurement (top left). Illustration of the various ports and chamber of the bushing and casing (top right), where the red curve represents the original inertia track. Exploded view of the bushing and casing (bottom).

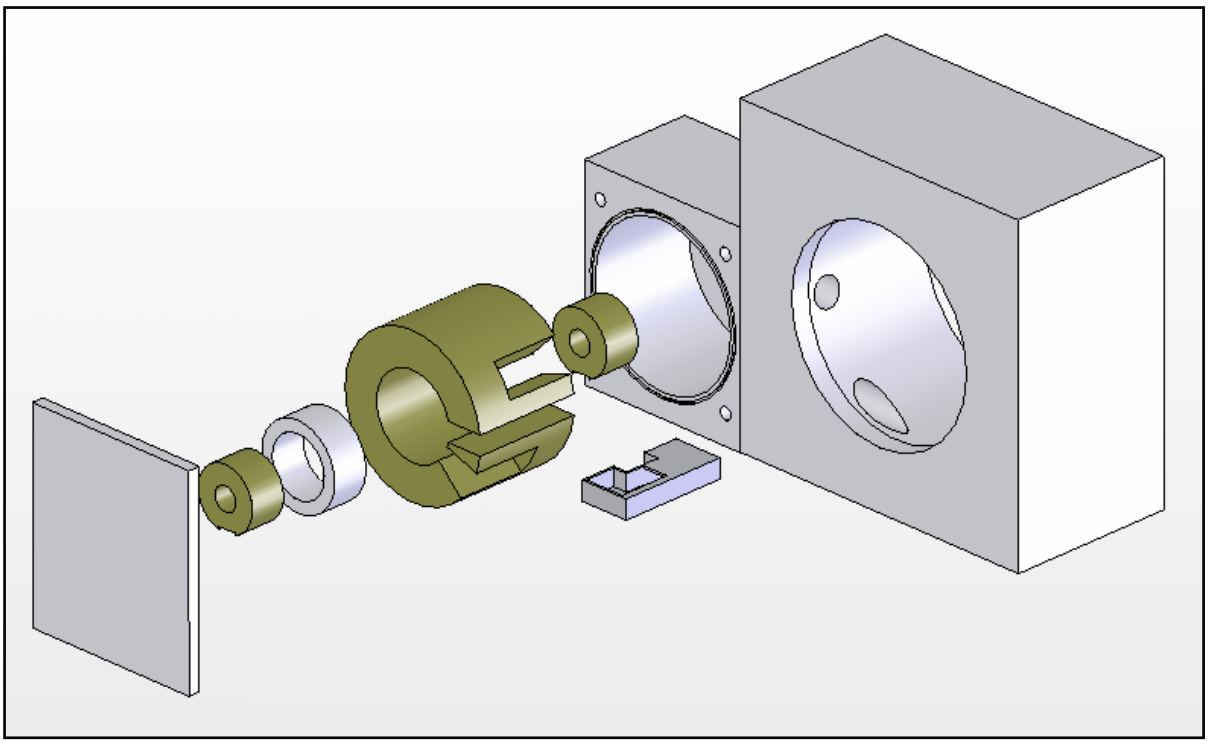

Figure 4-7: Prototype MR valve exploded view (brown – 1020 steel core material, grey – 6061 aluminum).

4.2.2 Fixture design

A fixture is designed to mount the bushing on an electromagnetic shaker. This fixture accommodates both the dynamic stiffness and base excitation experiments. Also, it is designed to conduct the two tests on both the GM Corp. bushing and prototype MR bushing.

The two setups for stiffness and base excitation experiments are illustrated in Figure 4-8 and Figure 4-10, respectively. The brown and dark grey components are fabricated from cold rolled steel. The light grey components are made from stiff 2024 aluminium. Finite element analysis showed that the lowest mode of vibration of these fixtures is beyond 280 Hz, well out of the range of interest (0-120 Hz). Moreover, to ensure accurate results, the maximum deflection of the fixtures under peak loading (4000 N) is less than 0.0075 mm.

The bushing shown in Figure 4-8 and Figure 4-10 can be substituted in the assembly for the prototype bushing. The prototype bushing will be discussed in detail in sections to follow.

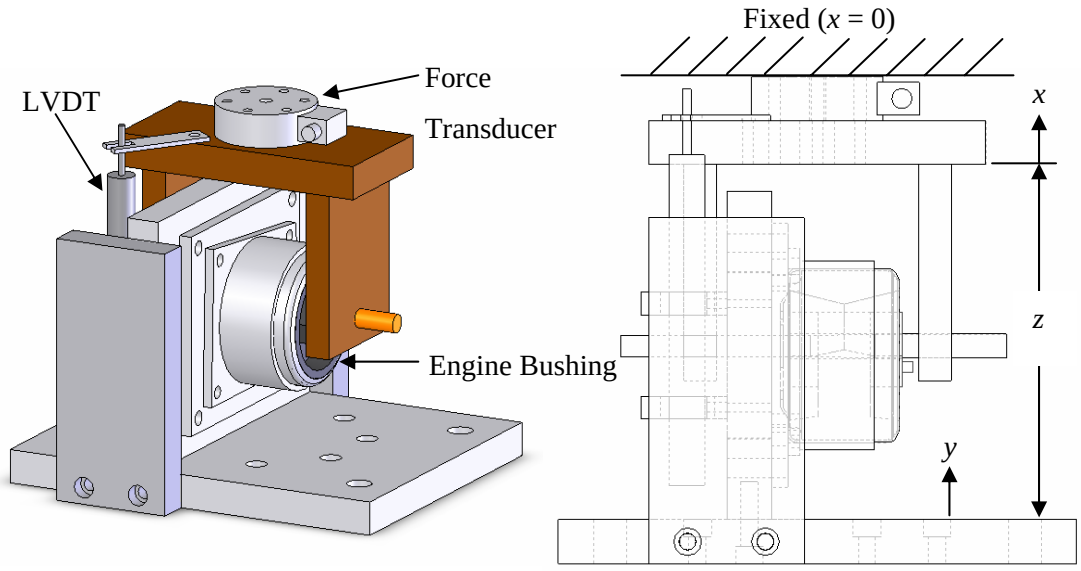

Figure 4-8: Illustration of the setup to measure dynamic stiffness.

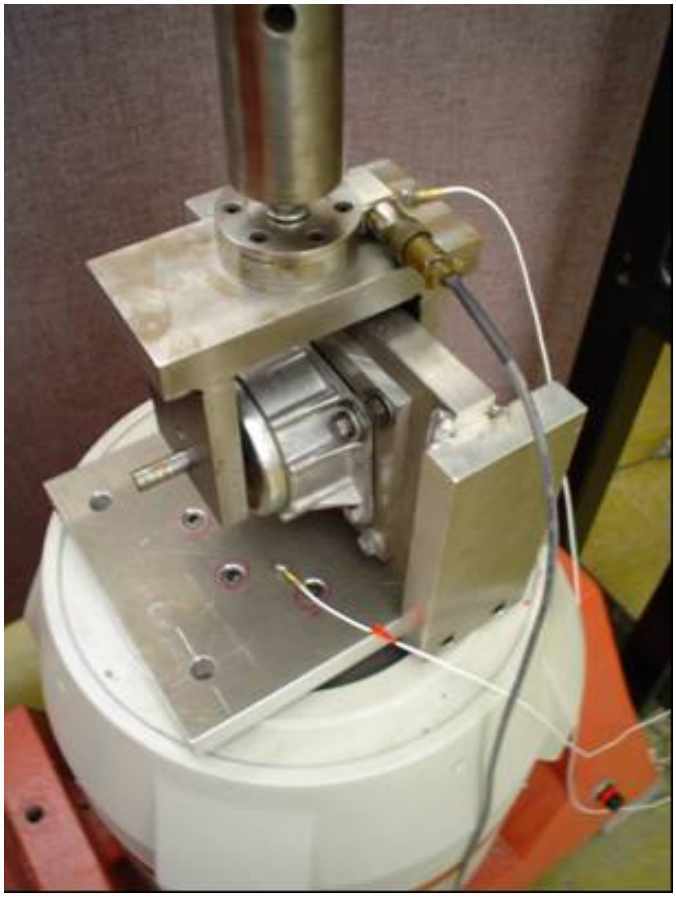

Figure 4-9: Dynamic stiffness fixture and bushing mounted on the LDS V722 shaker.

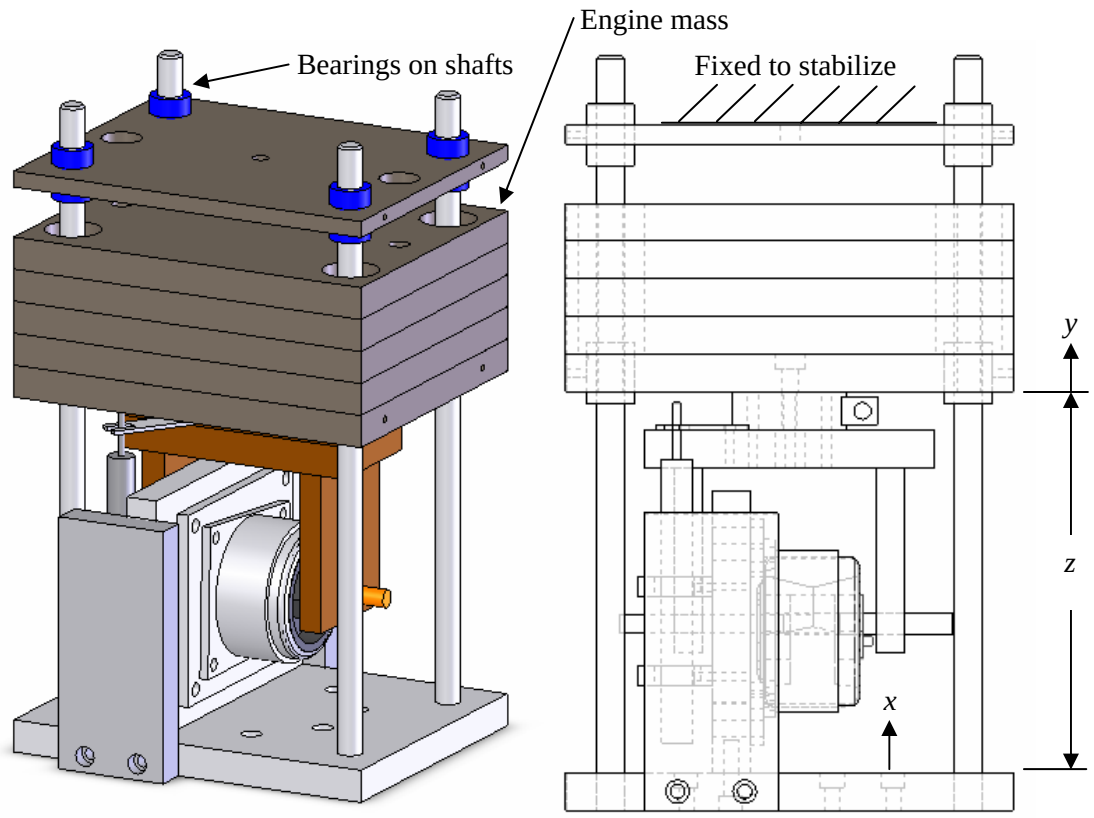

Figure 4-10: Illustration of the setup to measure transmissibility via a base excitation experiment.

The fixture shown above is attached to the mount plate of the shaker, as shown in Figure 4-9, Figure 4-11, and Figure 4-12. Figure 4-12 is a photograph, similar to Figure 4-11, of the MR valve and casing assembly illustrated in Figure 4-7 set up for a base excitation experiment.

4.2.3 Sensors and Excitation

Similar to the RMS experiment, the states $\ddot{x}$, $\ddot{y}$, and z are measured using the Dytran accelerometers the LDC500C DC LVDT, respectively. The force transmitted through the mount is measured by a Sensotec Model 41, 1000 lb precision pancake load cell. The same LDS V722 shaker setup was used to generate the feedback controlled inputs.

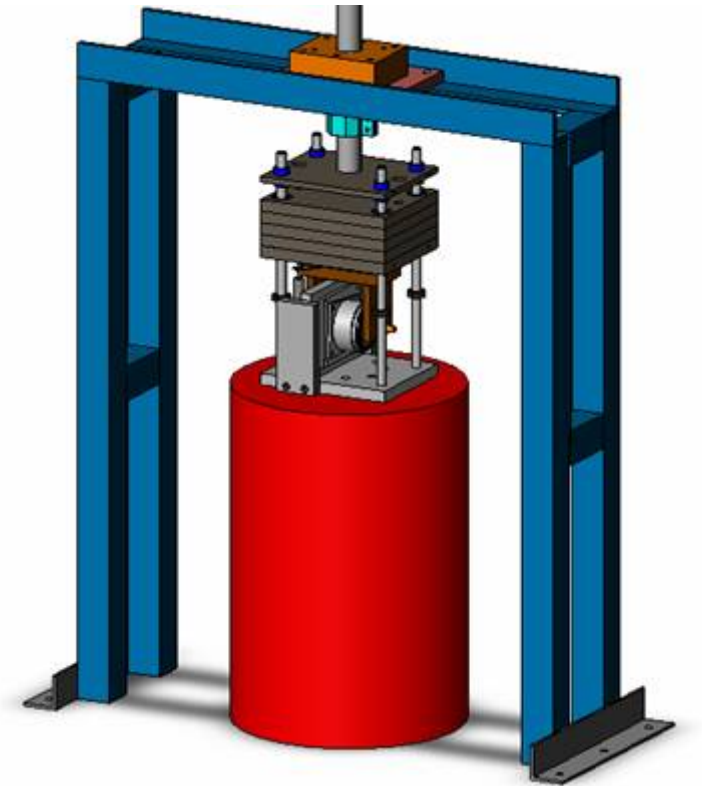

Figure 4-11: Solid model of the base excitation setup mounted on the shaker.

Figure 4-12: The MR valve set up used to conduct base excitation experiments

4.2.4 Experiment Issues

The shaker frame which fixes the mount relative to the shaker (shown in blue in Figure 4-11) is insufficiently rigid to conduct proper dynamic stiffness tests. This frame, similar to a standard rate machine (MTS or Instron hydraulic test stand) stretches and contracts with the load transferred through the mount.

This is illustrated in Figure 4-13, where the LVDT measures the relative displacement to be changing with frequency although the shaker is oscillating with constant amplitude of displacement, during a typical dynamic stiffness test. Dynamic stiffness tests were conducted with a preload of 1175 N such that the frame was in tension.

Corresponding peaks in the transmitted force can be seen in Figure 4-14. This means that any dynamic stiffness measurement would contain the dynamics of the mount and the frame. Under normal conditions, the frame would be assumed to be rigid.

Moreover, modal analysis revealed that the first two modes of the frame are at approximately 19 and 47 Hz, as illustrated in Figure 4-15 and Figure 4-16, respectively.

For this reason, results from the measurement of the dynamic stiffness are assumed to be relatively poor and for the most part will be ignored. The base excitation results were sufficient to measure the performance of the magnetorheological device; however, since only dynamic stiffness simulations have been presented it is difficult to compare the simulations and experiment results directly.

The frame was a structure that was developed for previous projects conducted on the shaker with significantly lower loads. The development of a frame to suit engine mount testing is suggested, but out of the scope of the current project.

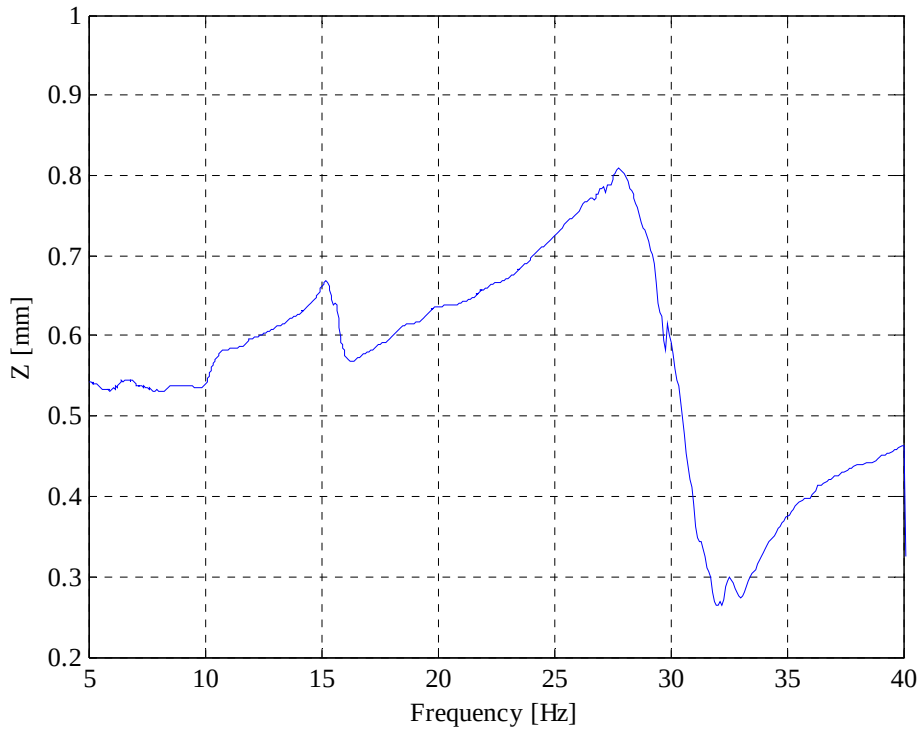

Figure 4-13: Variation of relative displacement despite constant amplitude input during a dynamic stiffness test.

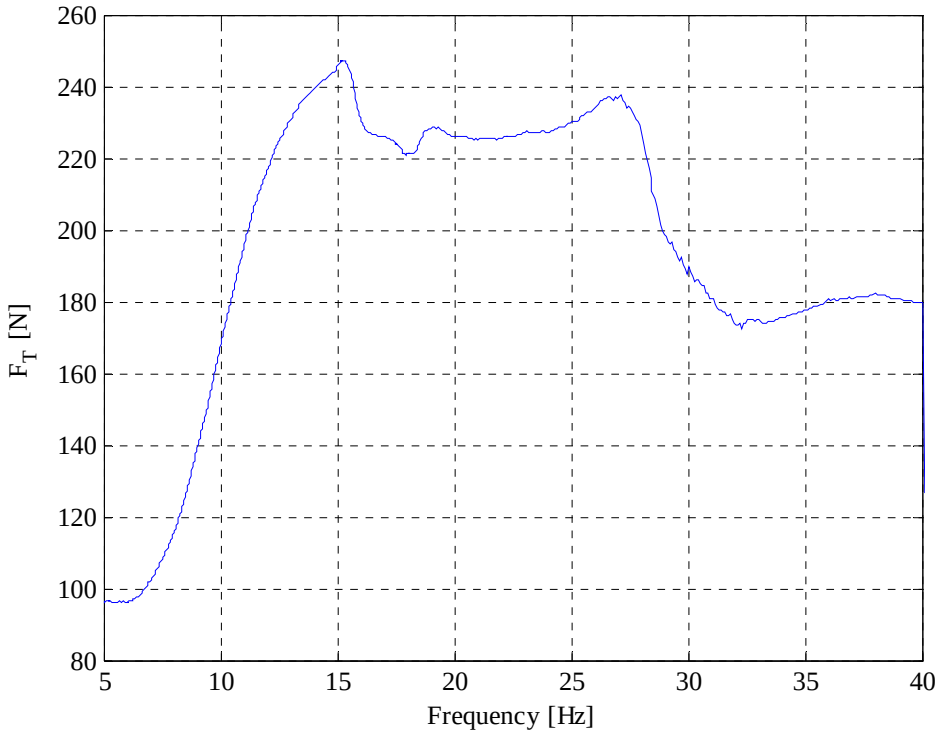

Figure 4-14: Variation of transferred force with peaks corresponding to the peaks in relative displacement during a dynamic stiffness test.

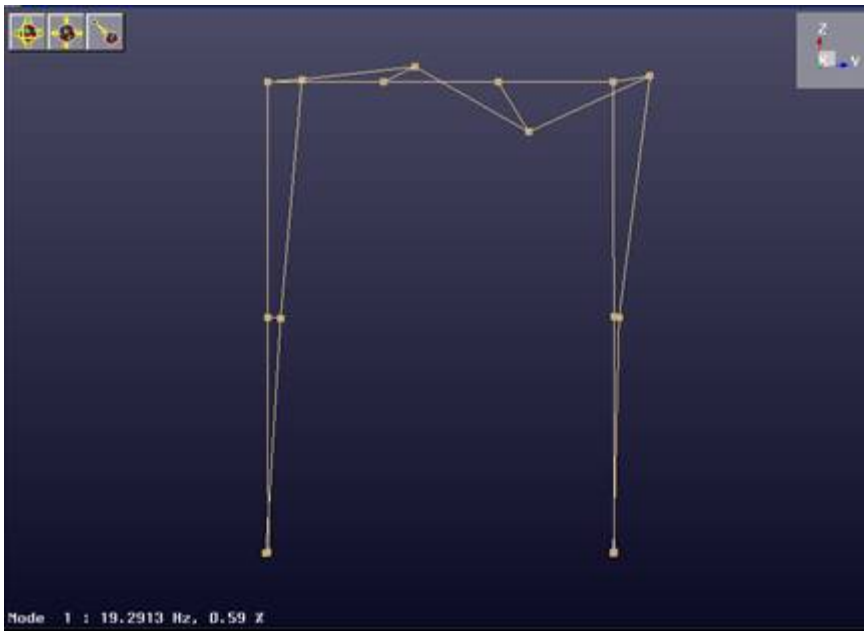

Figure 4-15: Modal analysis results illustrating the first mode of vibration of the shaker frame at approximately 19 Hz.

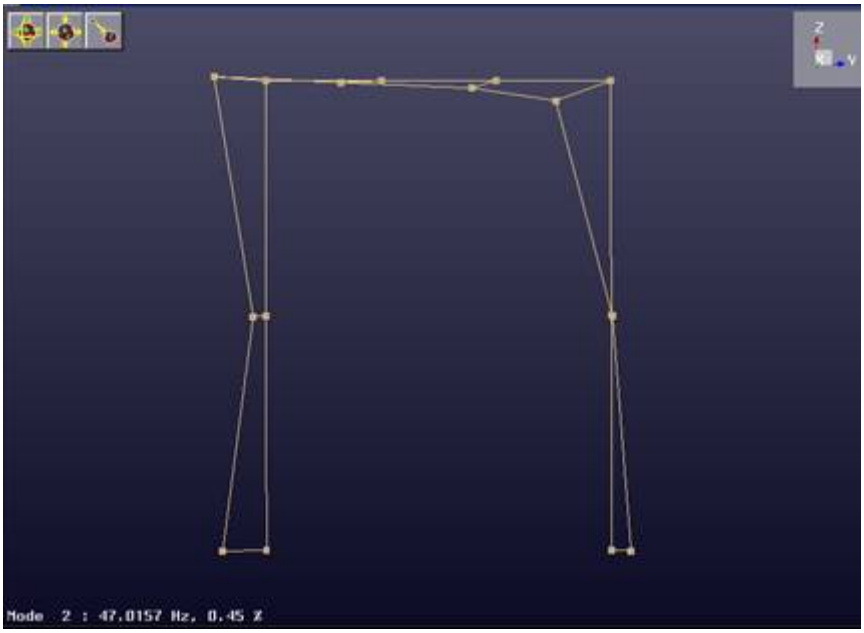

Figure 4-16: Modal analysis results illustrating the second mode of vibration of the shaker frame at approximately 47 Hz.

Furthermore, the base excitation dynamic response was initially highly contaminated by a second mode of vibration, as seen in Figure 4-17 and illustrated in Figure 4-18. This issue was resolved by replacing the original linear ball bearing with brass bushing with 50 mm of engagement.

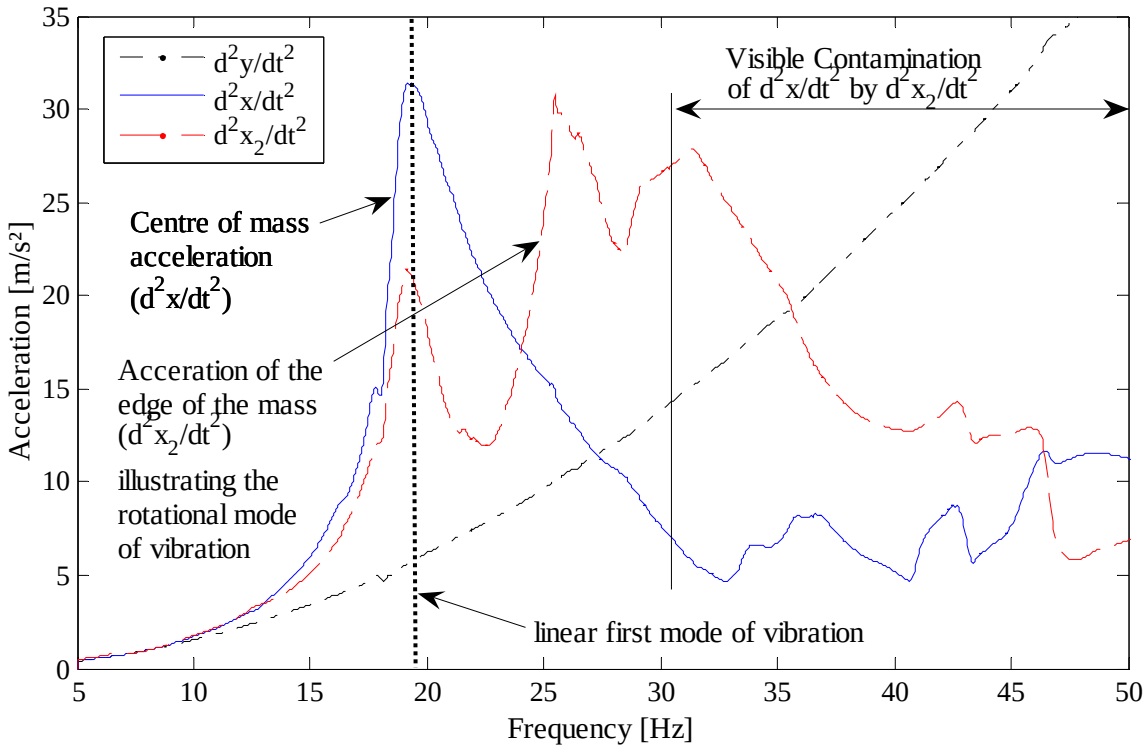

Figure 4-17: Initial hydraulic bushing acceleration results given base excitation input. Two main modes of vibration are present: linear mode (19 Hz) and a rotational mode (26 Hz) identified by the high edge acceleration with respect to the acceleration of the centre of mass.

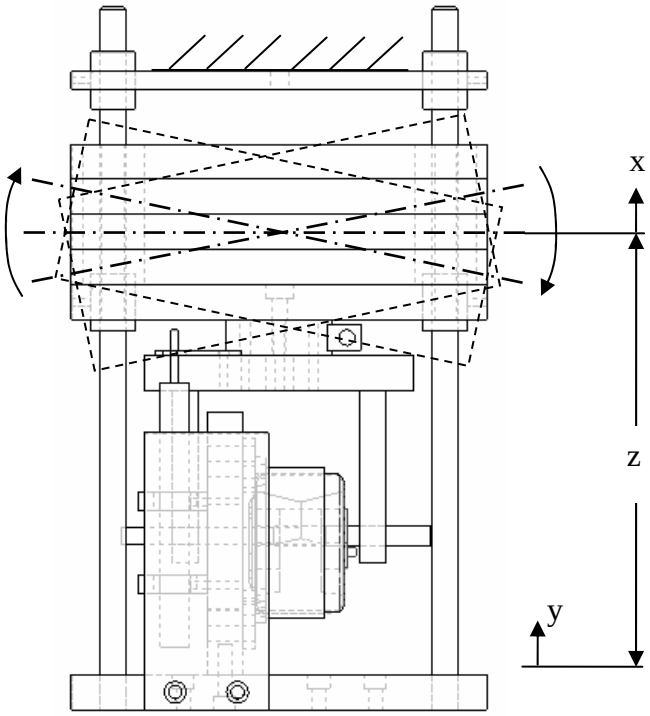

Figure 4-18: Illustration of the undesirable rotational mode of vibration.

4.3 Summary

This chapter details the three setups used to conduct the experiments. In section 4.1 the setup used to verify the previous base excitation frequency domain optimization work conducted by Jazar *et al*. (2003). In addition, this single degree of freedom setup is used to verify the new forced response results presented in Chapter 3.

Section 4.2 describes the components of the MR valve, and the integration of the valve with the existing bushing using a custom made manifold. A fixture is designed to interface the purchased engine bushing and prototype MR bushing to an electromagnetic shaker. The fixture is designed to accommodate both dynamic stiffness experiments and base excitation; however the existing structure is inadequate for dynamic stiffness measurement. It is also concluded that, for base excitation experiments, very long engagement bushings or bearings are required to eliminate rotational modes of vibration and binding.

Chapter 5
Experimental Results and Evaluation

The purpose of this chapter is to illustrate the results of the experiments described in Chapter 4. The experimental verification of the linear RMS optimization techniques are given in section 5.1. The performance of the bushing and MR bushing are given in Section 5.2.

5.1 Linear RMS Optimization Experiments

As demonstrated in previous reports, the root mean square (RMS) of the frequency response of a single degree of freedom (SDOF) oscillator over the range of 0 to 20 Hz reveals an optimum damping ratio given a certain natural frequency. These partial-optimum points have been found under conditions of base excitation, unbalance loading, and constant amplitude forcing inputs.

The results of several experiments are presented in which the frequency response of a SDOF is generated experimentally as detailed in the Chapter 4. The purpose of the experiments is to experimentally verify that the RMS optimization procedure can be applied to a real system.

5.1.1 RMS Optimization of the Base Excited Isolator

In order to verify base excitation RMS optimization curves, a series of frequency responses at different damping ratios were generated, and the RMS values computed. Table 5-1 details the experiment parameters and observations, where ζ is the linear damping ratio of the experiment.

Table 5-1: Base excitation test parameters and observations.

Test	|Y| [mm]	Observations	
		ζ	Comments
1	2.25	0.4543	ζ too high, friction dominated, results omitted
2	2.25	0.3190	
3	2.25	0.2277	
4	2.25	0.1805	
5	2.25	0.1477	
6	2.25	0.1434	

A sample of the experimental data acquired is illustrated in Figure 5-1. Note that friction has an effect on the amplitude of relative displacement at low frequencies. Overall, the response is quite linear. The entire data set is presented in Appendix A.

The RMS results are plotted in Figure 5-2 and Figure 5-3. The RMS results in Jazar *et al*. (2003) are computed over the range of 0 to 20 Hz. This is very difficult to reproduce experimentally since shakers cannot produce zero frequency inputs. The LDS V722 shaker used in this application has a minimum frequency of 5 Hz. The experimental RMS values are slightly skewed since the frequency range that the RMS integral is computed from 5 to 20 Hz. Hence the experimental result must be compared to the theoretical RMS result computed from 5 to 20 Hz, as illustrated by the dotted line in Figure 5-2.

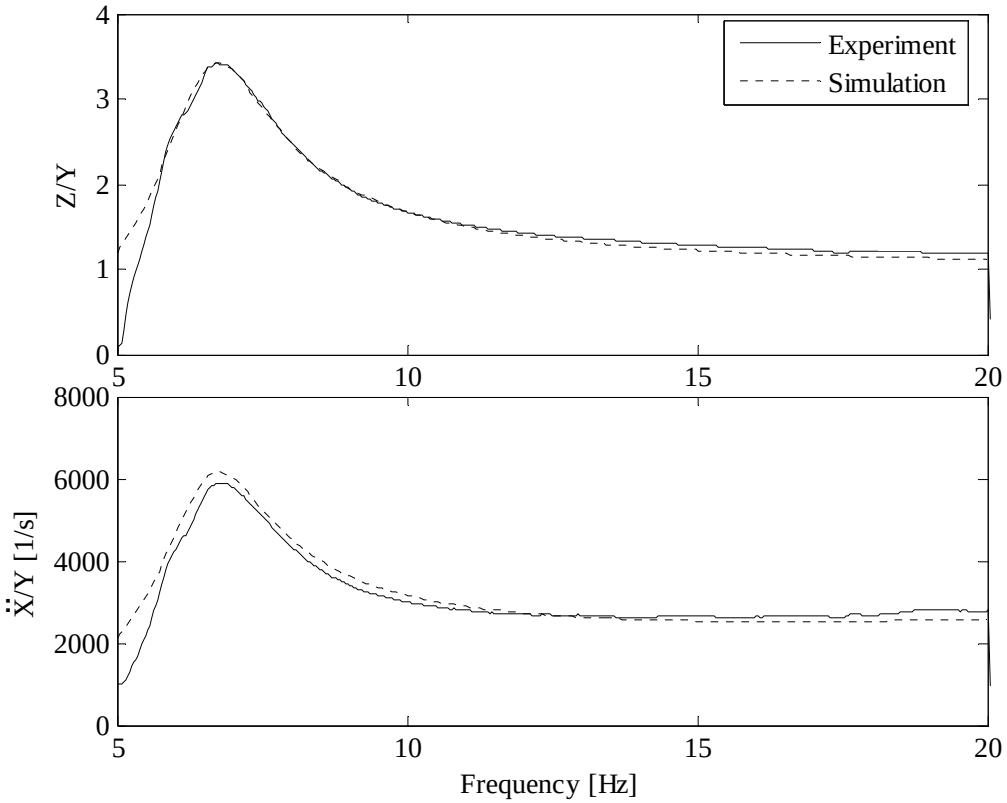

Figure 5-1: Base excitation frequency response (experiment – solid line, simulation – dotted line).

Moreover, the natural frequency of this system is 6.6 Hz, thus the theoretical result lies between the 6 and 7 Hz lines, as illustrated in Figure 5-3. For more detail, the theoretical results plotted in Figure 5-3 can be found in equivalent figures in Chapter 2.

Comparing the experimental data to the equivalent linear 5 – 20 Hz theoretical RMS result shows that the values are quite similar but begin to deviate as damping ratio increases. This is likely due to the increase in the dominance of nonlinear friction as damping ratio increases.

The most important observation that can be made from Figure 5-2 is that the real system is optimal at similar damping ratio as predicted by the theoretical result. The minimum RMS of acceleration (*R*) for a system of $\omega_n = 6.6$ Hz occurs at approximately $\zeta = 0.21$. Similarly, $\zeta = 0.18$ yields the lowest measured value of RMS acceleration for the experimental apparatus.

The exact minimum experimental value is difficult to measure without precise control over the damping ratio. Moreover, ζ cannot be directly measured. However, the experimental result confirms the theoretical result since it demonstrates similar trends in addition to the fact that the damping which produced the lowest measured RMS acceleration value was very close to the theoretical result.

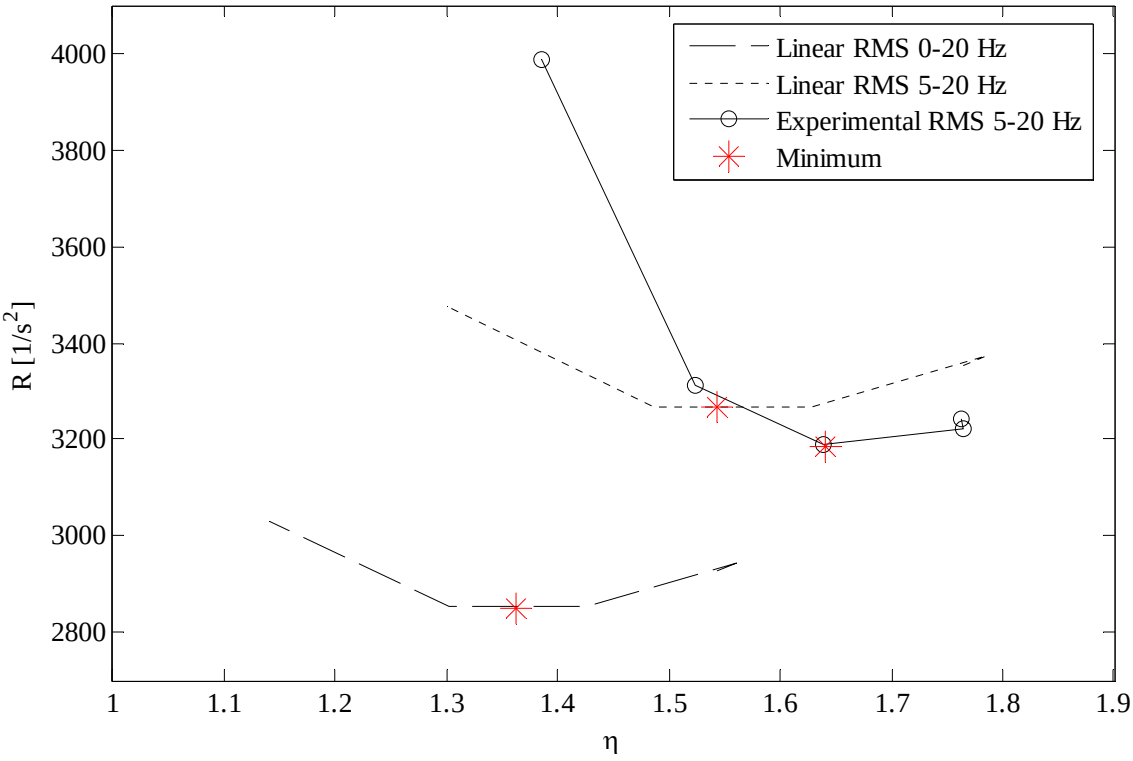

Figure 5-2: Base excitation experiment RMS results compared to theoretical results.

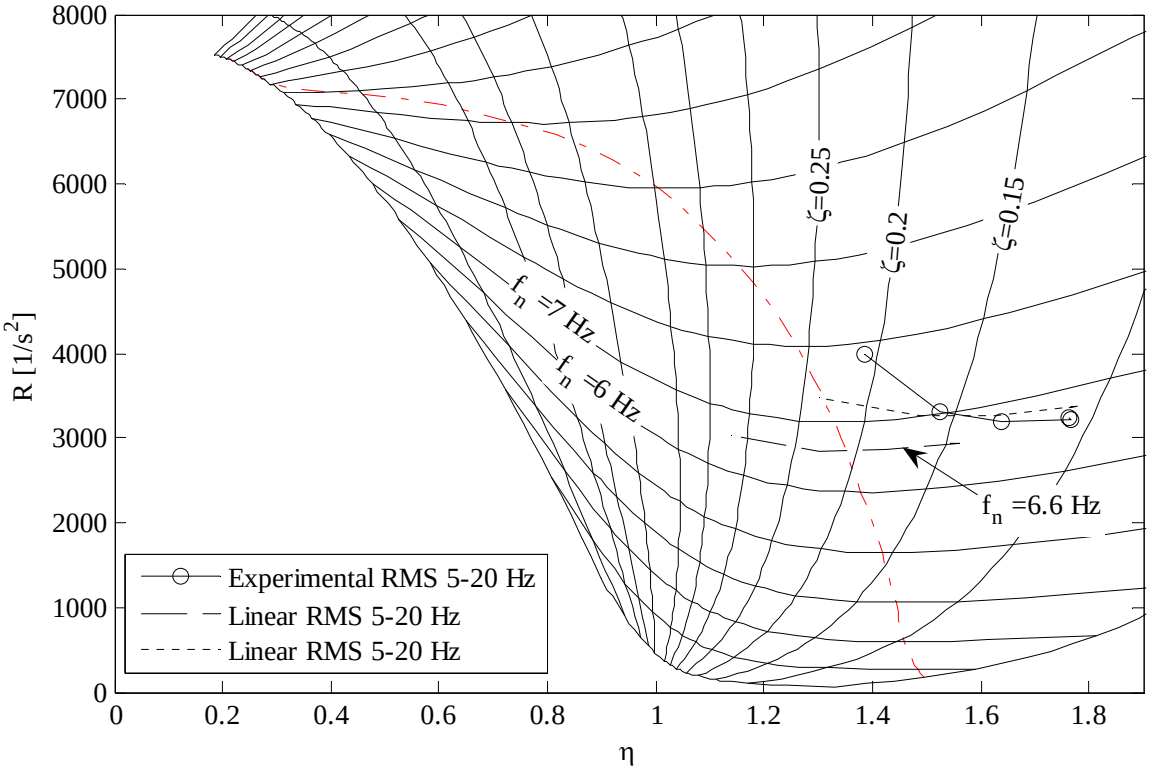

Figure 5-3: Experiment base excitation results illustrated on the linear RMS optimization graph. Note that the experiment RMS values are computed from 5 to 20 Hz.

5.1.2 RMS Optimization of the Unbalance Excited Isolator

The linear SDOF isolator optimization given an unbalance excitation, or a force which increases proportional to ω^2, was presented in Chapter 3. As mentioned in the previous chapter, the experimental generation of these results is achieved by equivalently accelerating the frame of reference. This is done experimentally by applying a base excitation sweep of constant amplitude of displacement. Thus the result presented in section 5.1.1 also validates the RMS optimization of the unbalance excited linear isolator.

5.1.3 RMS Optimization of the Harmonic Force Excited Isolator

In Chapter 3 the optimization of a SDOF isolator given harmonic forcing on the mass was presented. As detailed in the Chapter 4, this result can be generated experimentally by equivalently accelerating the frame of reference; thus there is no need for a force controlled actuator. The similarities in the experimental values and simulated forced responses illustrated in Figure 5-4 validate the experimental method. Table 5-2 details the experiment parameters and observations.

Figure 5-4 illustrates the frequency responses generated from the trials described in Table 5-2. Note that there is very little difference between the linear and experimental results at low frequency. This is because the forcing is constant across the entire frequency range, and initially it is large enough to overcome the friction at 5 Hz.

The RMS result is illustrated in Figure 5-5 for clarity, as well as with the entire optimization plot in Figure 5-6. Figure 5-6 verifies that the 0 to 5 Hz linear RMS result is correct while Figure 5-5 is used to more readily evaluate the result. It can be seen that although the optimum point is being approached, it cannot be reached since the maximum damping ratio is limited to ζ = 0.6514, given by the dashpot; however, this result does verify the trend suggested by the linear analysis. The optimum point could possibly be reached experimentally by decreasing both the stiffness and mass,

maintaining f_n, while increasing the maximum attainable ζ ; although, this change may increase the effect of nonlinearity.

Table 5-2: Forced excitation test parameters and observations.

Test	$\lvert\ddot{Y}\rvert$ [m/s^2]	Observations	
		ζ	Comments
1	5	0.3713	
2	5	0.2715	
3	5	0.2158	
4	5	0.1772	
5	5	0.1605	
6	5	0.1493	
7	5	0.1417	Tests 8 and 9 are omitted due to poor results
10	5	0.6514	Very low damping
11	5	0.4692	Low damping
12	5	0.4230	Low damping
13	5	0.3793	Low damping

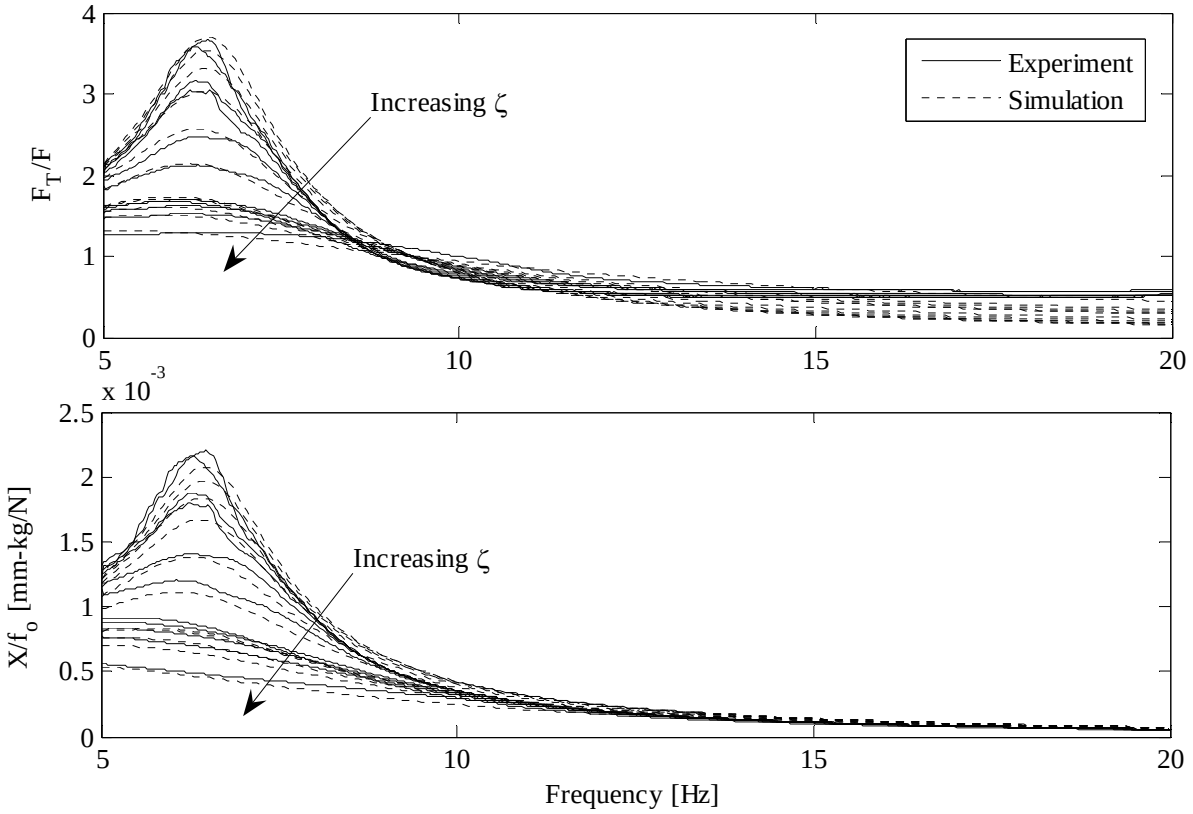

Figure 5-4: Forced frequency response (experiment– solid line, simulation – dotted line).

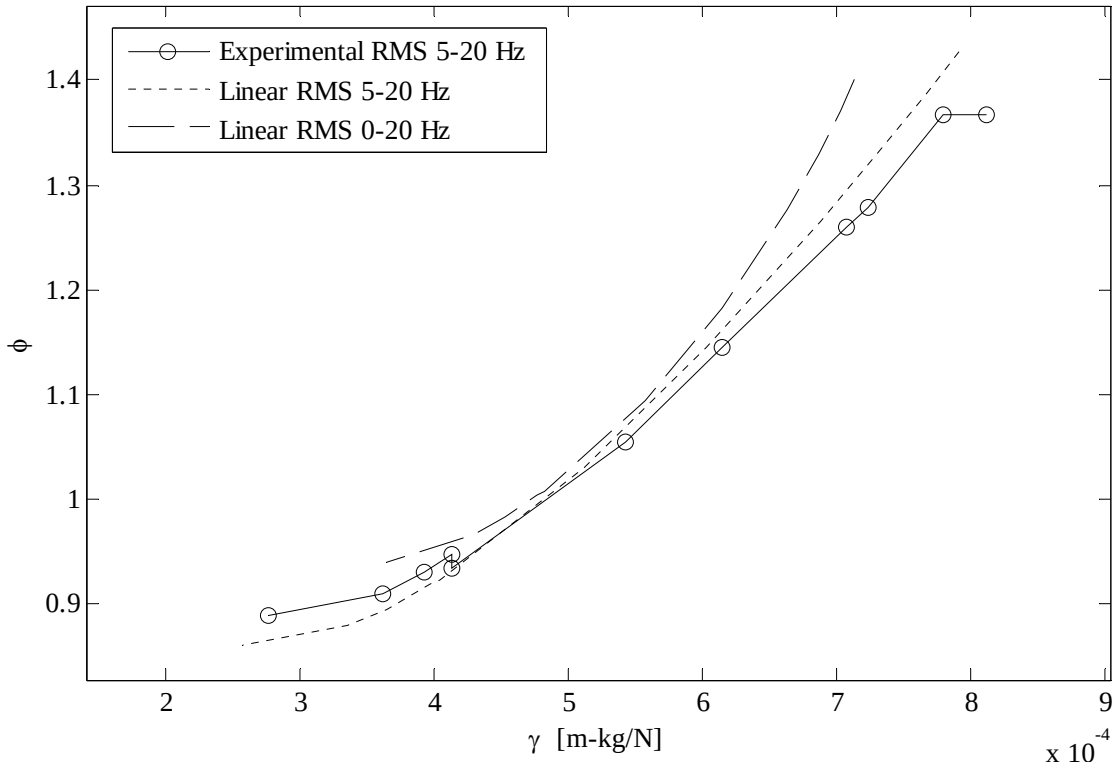

Figure 5-5: Experimental RMS Results compared to linear results.

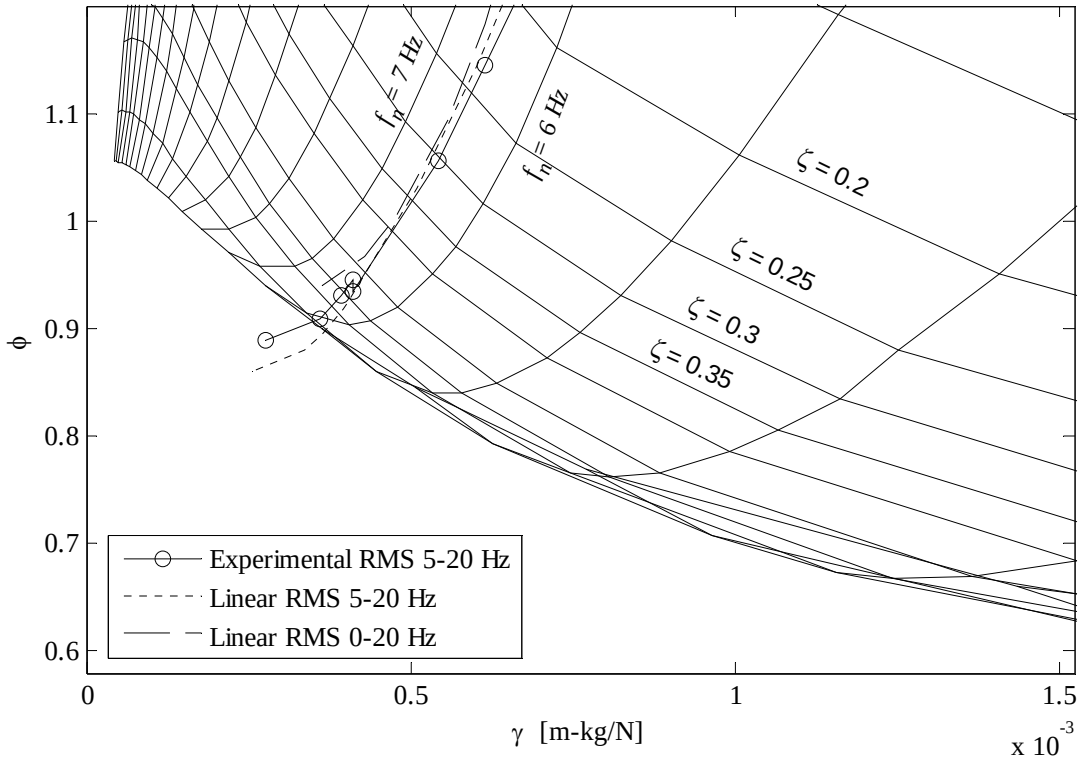

Figure 5-6: Experiment harmonic forced results illustrated on the linear RMS optimization graph. Note that the experiment RMS values are computed from 5 to 20 Hz.

5.2 MR Hydraulic Bushing Experiment

5.2.1 Verification of Bushing Model Parameter Values

A model of a hydraulic bushing was presented in Chapter 3. The parameters of the model were identified from data supplied for the bushing P/N 90576090. However, the bushing that was to be replaced by a semi-active bushing is P/N 90575028 (Figure 5-7). Bushing modeling and parameter identification was carried out on the available data, assuming that the two bushings would have similar properties.

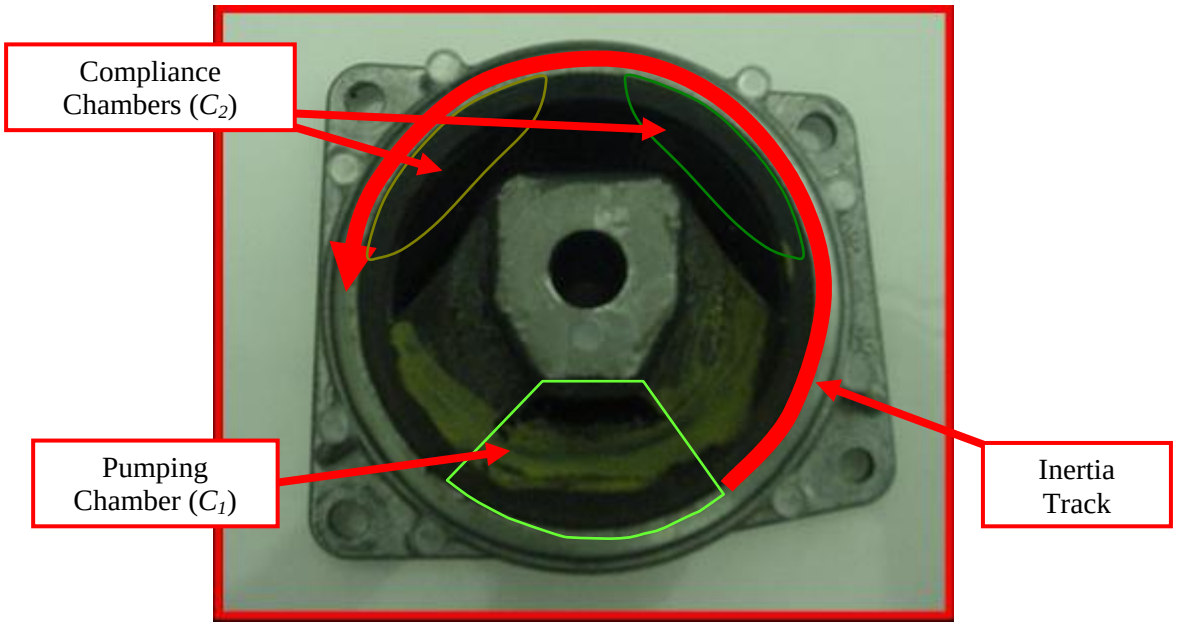

Figure 5-7: Photograph of the hydraulic bushing P/N 90575028 (similar to 90576090).

Several experiments were conducted on bushing P/N 90575028 that would allow comparison of experimentally measured parameters to those derived from the dynamic stiffness response of bushing P/N 90576090. First off, the bushing's formed casing was pierced and the fluid was drained; this permits experimentation to determine the properties of the rubber alone. From the base excitation response to various input amplitudes, as illustrated in Figure 5-8, the rubber damping and stiffness was confirmed to be similar to the values stated previously as follows:

$$K_r = 172.8 \ \ N/mm,$$

$$B_r = 0.073 \;\; N \cdot s/mm \tag{5.1}$$

The two degree of freedom coupled linear equations of motion of a hydraulic bushing is

$$\begin{bmatrix} m & 0 \\ 0 & L \end{bmatrix} \begin{Bmatrix} \ddot{z} \\ \ddot{Q} \end{Bmatrix} + \begin{bmatrix} B_r & 0 \\ 0 & R_f \end{bmatrix} \begin{Bmatrix} \dot{z} \\ \dot{Q} \end{Bmatrix} + \begin{bmatrix} K_r + A_p{}^2/C_1 & -A_p/C_1 \\ -A_p/C_1 & C \end{bmatrix} \begin{Bmatrix} z \\ Q \end{Bmatrix} = 0 \tag{5.2}$$

Neglecting damping to estimate the frequency of the two modes of vibration, the eigenvalue problem is solved to arrive at the following characteristic equation:

$$\lambda_e{}^2 - \left[\frac{1}{m} \left(K_r + \frac{A_p{}^2}{C_1} \right) + \frac{C}{L} \right] \lambda_e + \frac{1}{m} \left[\left(K_r + \frac{A_p{}^2}{C_1} \right) \frac{C}{L} - \frac{A_p{}^2}{C_1{}^2 L} \right] = 0 \tag{5.3}$$

where the frequency of the two modes are

$$\omega_1 = 7.11 \,\text{Hz} \text{ and } \omega_2 = 23.40 \,\text{Hz} \tag{5.4}$$

given a 19.3 kg suspended mass for the bushing with P/N 90576090.

The damped frequency of this mode of vibration for the hydraulic bushing P/N 90575028 is given by the peak in mass acceleration shown in Figure 5-8 (solid curve). The damped frequency is approximately 20 Hz, very similar to the other bushing.

The second mode of vibration, occurring at $\omega_1 = 7.11 \,\text{Hz}$, is not visible in Figure 5-8 since the mass of the engine is relatively small and the second mode dominates. Also, this natural frequency is near to the minimum frequency of the shaker (5 Hz). When the mass is increased, the first mode is more prominent, as illustrated via simulation with an 80 kg mass in Figure 5-9. Comparing the frequency corresponding to the peaks in this simulation result to the computed values in equation (5.5) also illustrates that the simplifications used to estimate the undamped natural frequency predicts the result quite well.

$$\omega_1 = 5.40 \,\text{Hz} \text{ and } \omega_2 = 15.13 \,\text{Hz} \tag{5.5}$$

Furthermore, the dynamic stiffness results in Figure 5-10 comparing the external and internal (University of Waterloo) results for the two shows that the two bushings are very similar. The differences in two responses could be attributed to the poor experimental conditions as described in the previous chapter.

The above results validate the parameter identification and thus the parameters used in the simulation of the bushing and MR bushing results in previous chapters. Although it is difficult to demonstrate that the two bushings are identical without precise dynamic stiffness results on the P/N 90575028 bushing it is believed that the above analysis shows that the simulation model is appropriate to test the effect an MR valve in the inertia track.

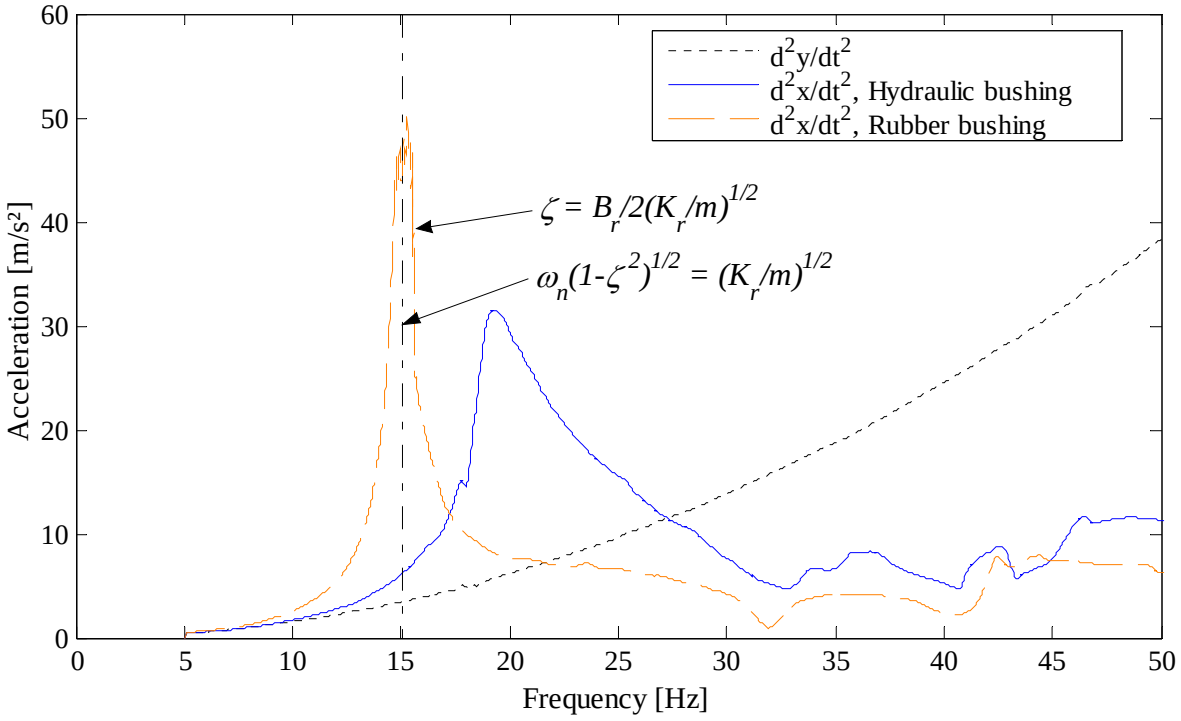

Figure 5-8: Response of the rubber and hydraulic bushing P/N 90575028 (*m = 19.3 kg*).

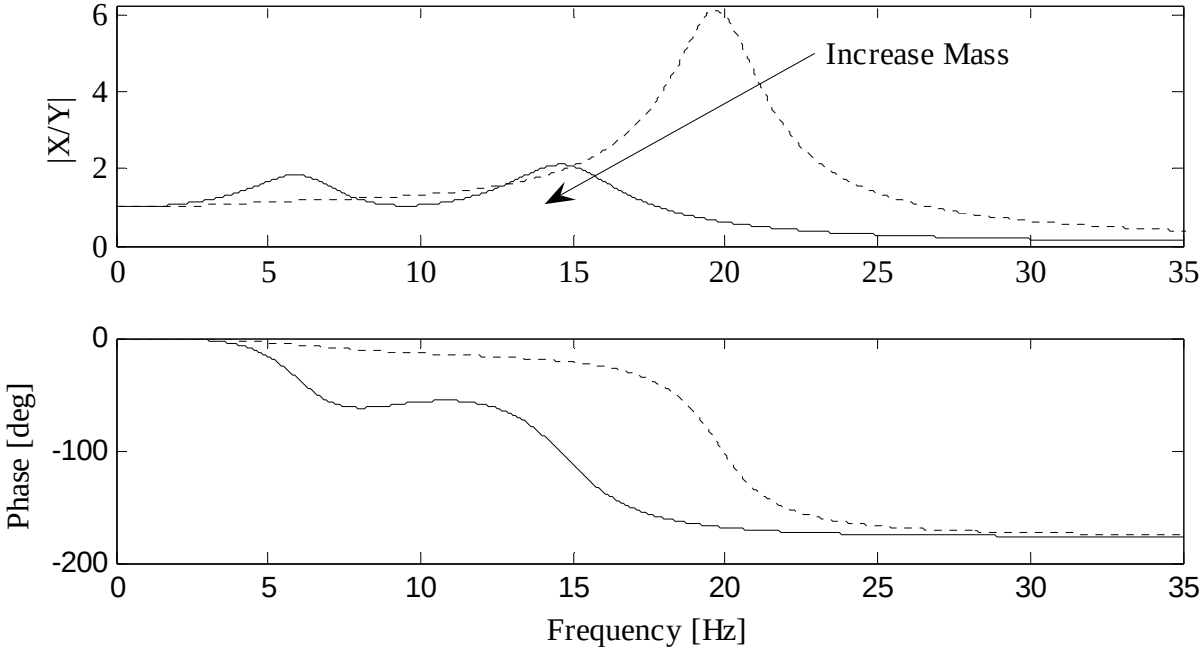

Figure 5-9: Hydraulic bushing simulation illustrating the change in the response of the two degrees of freedom as the suspended mass increases to 80 kg.

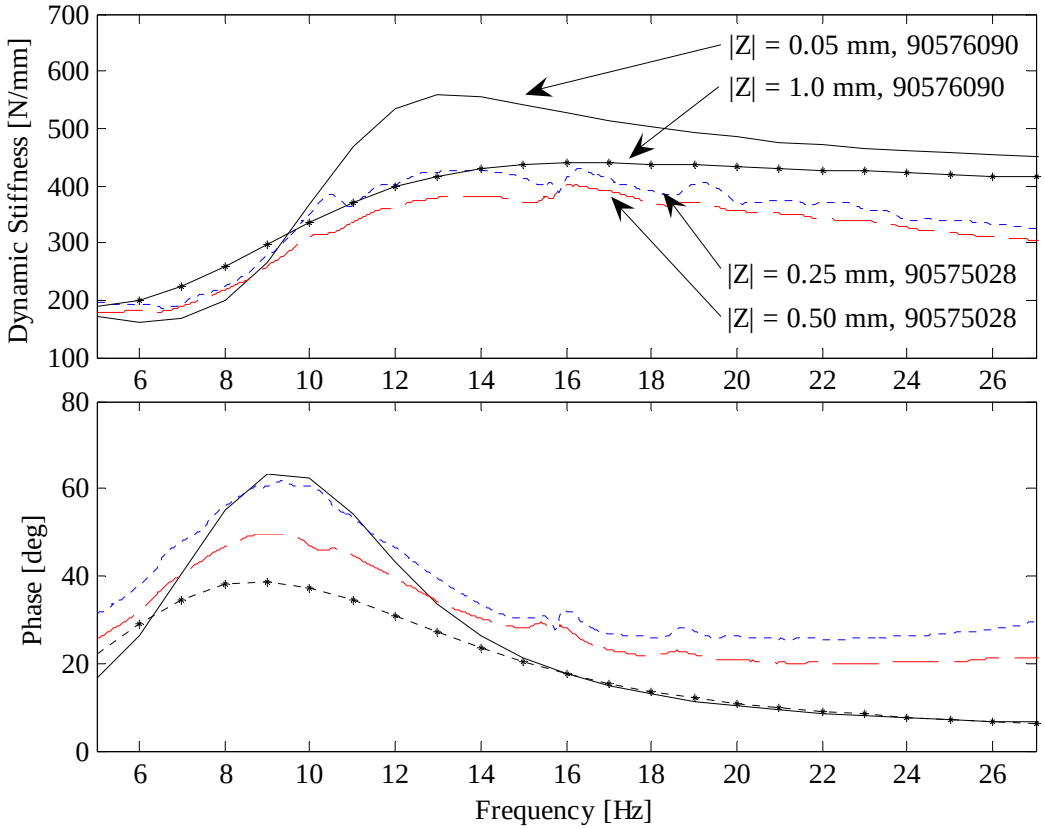

Figure 5-10: Dynamic stiffness of bushing P/N 90576090 (preload 1050 N) and bushing P/N 90575028 (preload 1175 N) measured in the University of Waterloo laboratory.

5.2.2 Dry MR Hydraulic Bushing Experiments

Base excitation experiments were conducted before adding the complexity of the MR fluid in the MR bushing setup. These tests serve as a benchmark for the performance of the experimental apparatus and are referred to as dry response tests since no fluid is used in the bushing. As mentioned in the Chapter 4, the base excitation experiment apparatus initially exhibited a great deal of rotational motion. This was considered not to be ideal and brass bushings were implemented to eliminate this mode of vibration.

The dry response of the MR bushing is shown in Figure 5-11 and Figure 5-12. Figure 5-11 is a plot of the measured response of the original system with the linear bearings and the initial suspended mass of 19.3 kg. Figure 5-12 illustrates the measured response of the final system with the low clearance brass bushings and the 31.3 kg suspended mass.

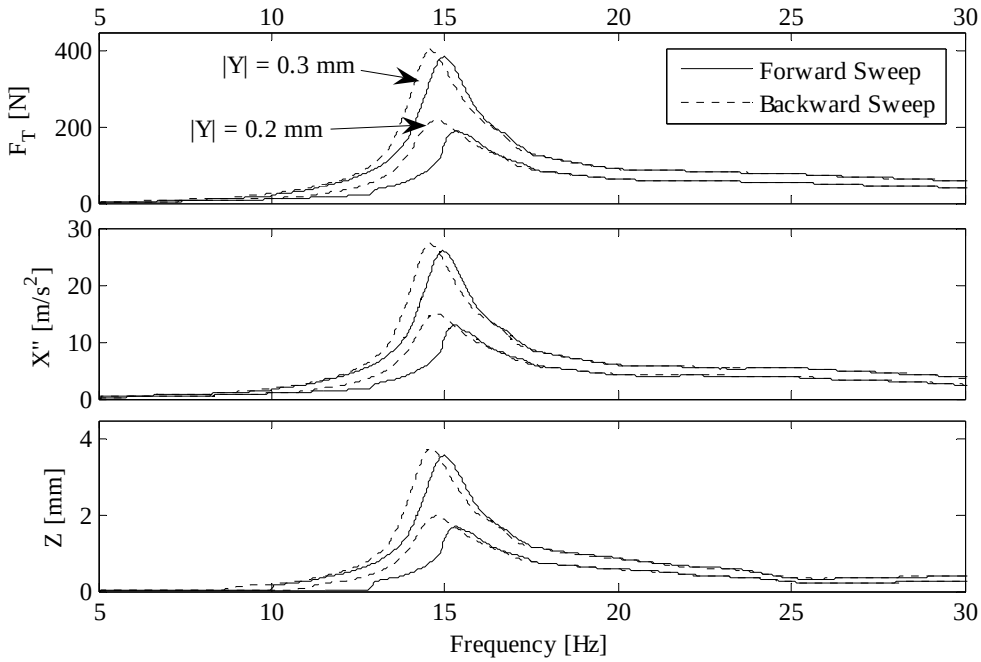

Figure 5-11: Dry engine mount base excitation with a 19.3 kg suspended mass.

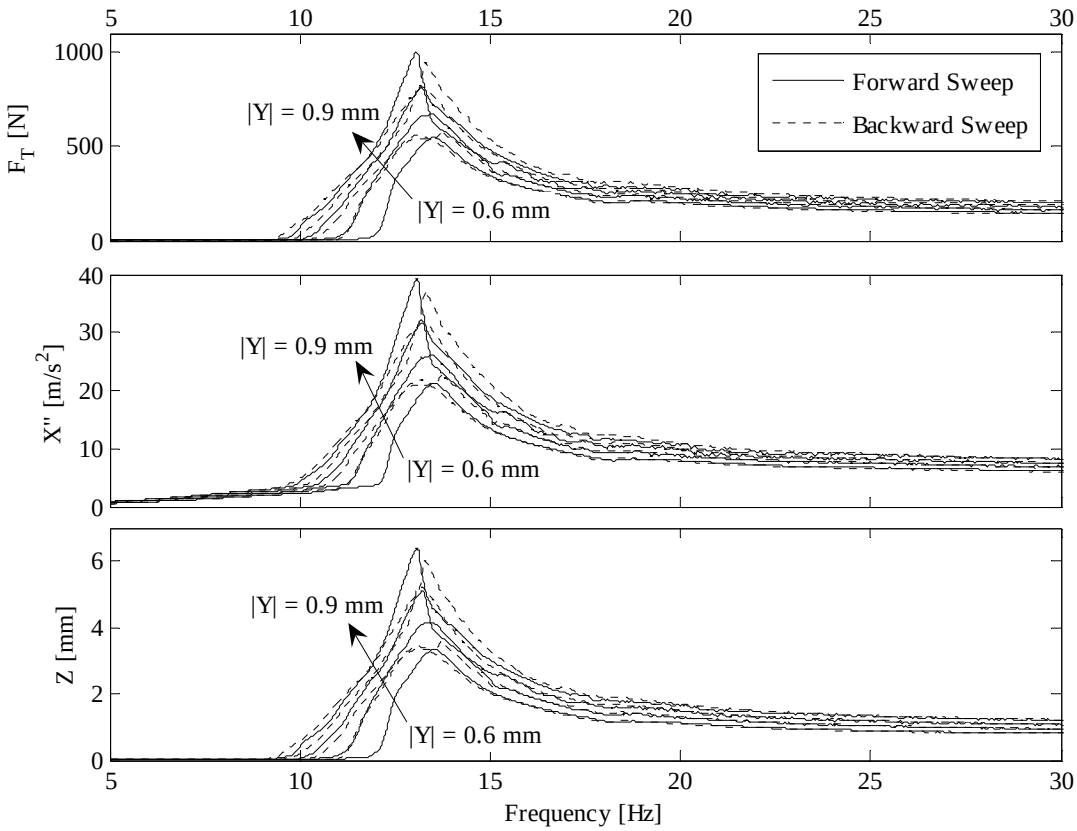

Figure 5-12: Base excitation of the dry engine mount with a 31 kg suspended mass. Base amplitudes are varied from 0.6 mm to 0.9.

Examining the forward and backward sweep frequency responses of both systems illustrates that they both have inherent nonlinearity which affects the response; although the brass bushing system (Figure 5-12) more accurately represents a two DOF system with its increased tolerances, the performance comes at the cost of greatly increased nonlinearity due to the increase in stiction and friction.

As the input amplitude increases, the frequency at which the stiction is overcome decreases proportional to the increase in inertia force, as shown in Figure 5-12. The backward sweep tends to come to rest at a lower frequency than the point where stiction is overcome by relative motion on the forward sweep. This represents the difference in magnitude of the stiction and coulomb friction and thus is the primary nonlinearity which causes the backward sweep from tracking the forward sweep.

Although friction caused by the new bushings has a large affect on the low frequency response, the improvement in the quality of the high frequency response is shown in the transfer function illustrated in Figure 5-13 which shows good results up to 70 Hz.

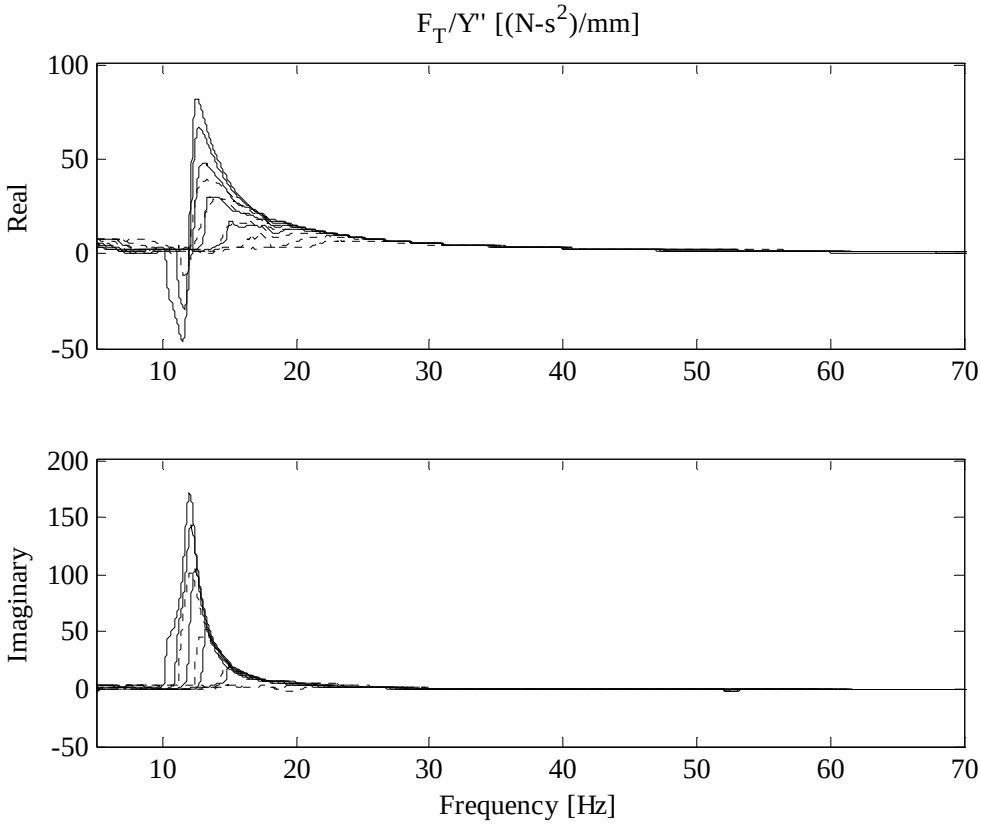

Figure 5-13: Force transmissibility with respect to base acceleration for the dry mount with a 31 kg suspended mass. Experiments are conducted for base amplitudes from 0.4 to 1.8 mm peak to peak. (dashed - backward sweep, solid - forward sweep)

The focus of the experimental work was placed on the system with the brass bushings since the goal was to develop a system suitable to test the dynamics of the low frequency response from 5-30 Hz was as well as the high frequency response (up to ~200 Hz). As more rigorous analysis of the results was done, the more difficult it became to work with such nonlinear experiment results. Weighing the cost of the slightly sloppy linear bearings versus the higher friction brass bushings, it is difficult to say which set up is ultimately better; however, for this stage of development of bushings, it is highly recommended to avoid base excitation experiments and have a set up which will

accurately measure the dynamic stiffness thus reducing the amount of nonlinearity to a more manageable level.

5.2.3 MR Hydraulic Bushing Experiments

Figures 5-14 to 5-17 illustrate the effect of varying current on the base acceleration and relative motion of the MR bushing for both experiment setups and the transmitted force for the base excitation setup with the brass bushings.

The initial result, illustrated in Figure 5-14, shows the base excitation response of the system given the linear bearings and a 19.3 kg suspended mass. Although the solenoid was designed to yield approximately 580 turns of 26 gauge wire only 335 turns where achieved on the initial implementation of the actual design. The current is incremented from 0 to 2 A, and given by the frequency response the MR valve appears to saturate between 1 and 2 A.

The result for the initial test illustrate that the impact of the MR effect on the base excitation response is minimal. However, both the acceleration and displacement response do demonstrate the two degrees of freedom of the MR hydraulic bushing; where the damped modal natural frequencies are approximately:

$$\omega_1 = 17.3\,\text{Hz} \text{ and } \omega_2 = 18.7\,\text{Hz} \tag{5.6}$$

for the off state (0 A) response shown in blue. Furthermore, as the amount of current increases these frequencies appear to decrease and the peak vibration amplitude increases. This observation is in direct agreement with the MR hydraulic bushing dynamic stiffness nonlinear simulation results presented in Chapter 3 which shows a downward shift of the notch frequencies and increase in dynamic stiffness as the current is increased. Moreover, as shown in the dynamic stiffness simulation results of Chapter 3 amount of damping reduces as the valve current increases which causes the increase in vibration amplitude.

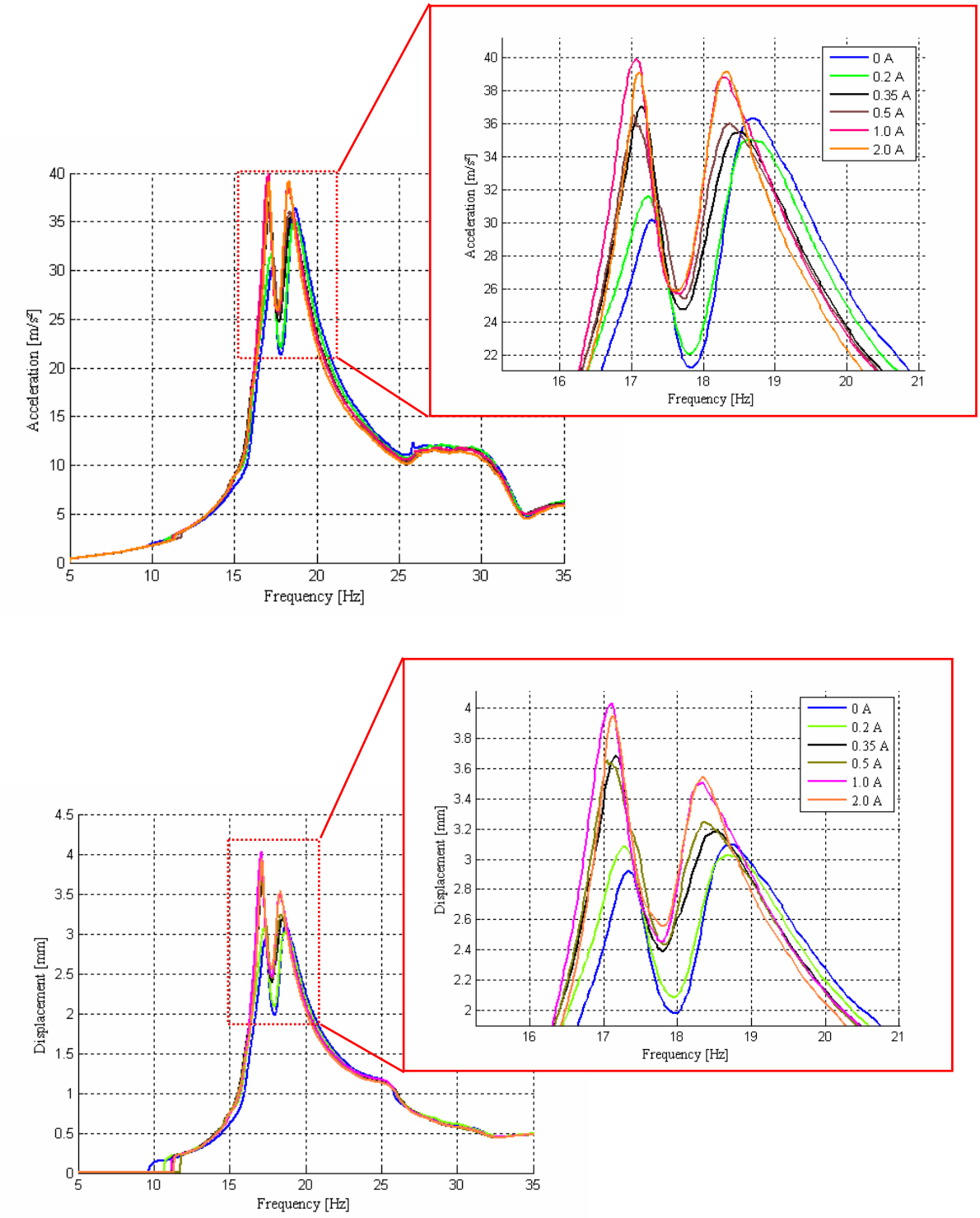

Figure 5-14: Original MR bushing base excitation ($|Y|$ = 0.4 mm) results generated with the 19.3 kg mass and using the roller bearings (top – mass acceleration, bottom – relative displacement)

Once the initial test results were complete to meet GM project deadlines some of the simple features of the MR valve design were refined. These changes to the valve included changing the linear bearings to the brass bushings, reproducing some of the MR valve parts which had been not machined to specifications and were patched together to function properly for the test, as well as refining the solenoid spool design to accommodate wire routing. Re-winding the spool had an impact on the results since the number of turns was reduced to approximately 280, thus increasing the saturation current since the flux is proportional to the current and the number of turns.

$$\varphi \propto NI \tag{5.7}$$

Figure 5-15 illustrates that the response of the bushing seems to saturate around 2-3 A. Aside from scaling the effect of current on the magnetic circuit the changes to the solenoid are negligible since the tests are conducted at steady state electrical conditions.

In the results shown in Figure 5-15 and Figure 5-16 the current is varied from 0 to 3 amperes and the results are shown for three different base excitation inputs: the magnitudes of base oscillation are 0.6, 0.7 and 0.8 mm. Note that in these results the two modes of vibration are not distinguishable due to the large amount of friction.

Varying the current from 0 to 3 A the effective stiffness of the mode of vibration is reduced about 10%, this compares to a 2.6% decrease in the first trial shown in Figure 5-14. This increase in performance can be attributed to the improvements in the MR valve design. In addition, the transferred force results illustrated in Figure 5-17 show the same trends observed in Figure 5-15 and Figure 5-16.

Although the valve design for these tests was to specifications, as was the goal of the second trial, the increased performance is not significant enough to suggest that this design solution is appropriate to solve the cylinder-on-demand isolation requirements.

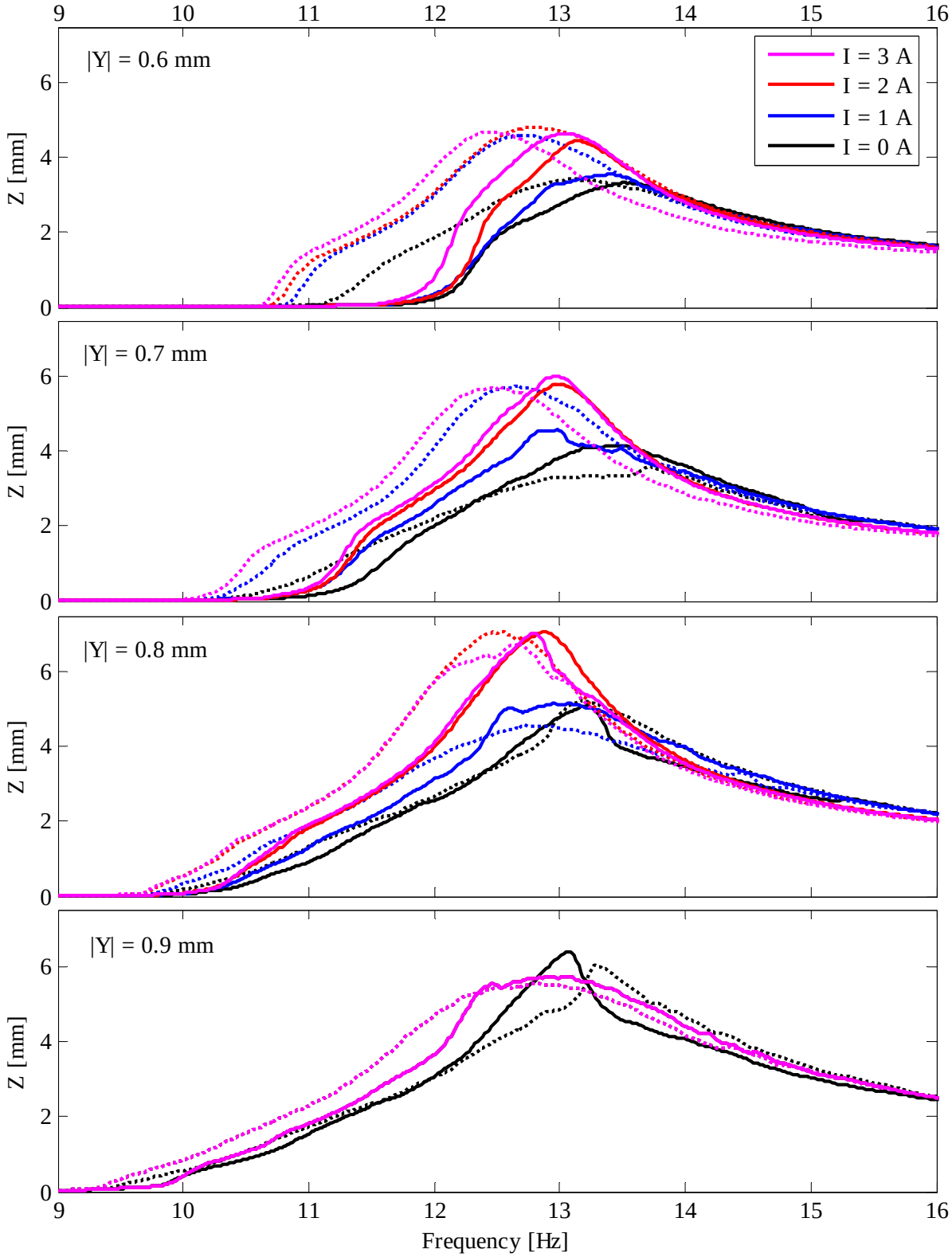

Figure 5-15: MR bushing base excitation relative displacement results generated with the 31.3 kg mass and using the brass bearings (solid – forward sweep, dotted – backward sweep).

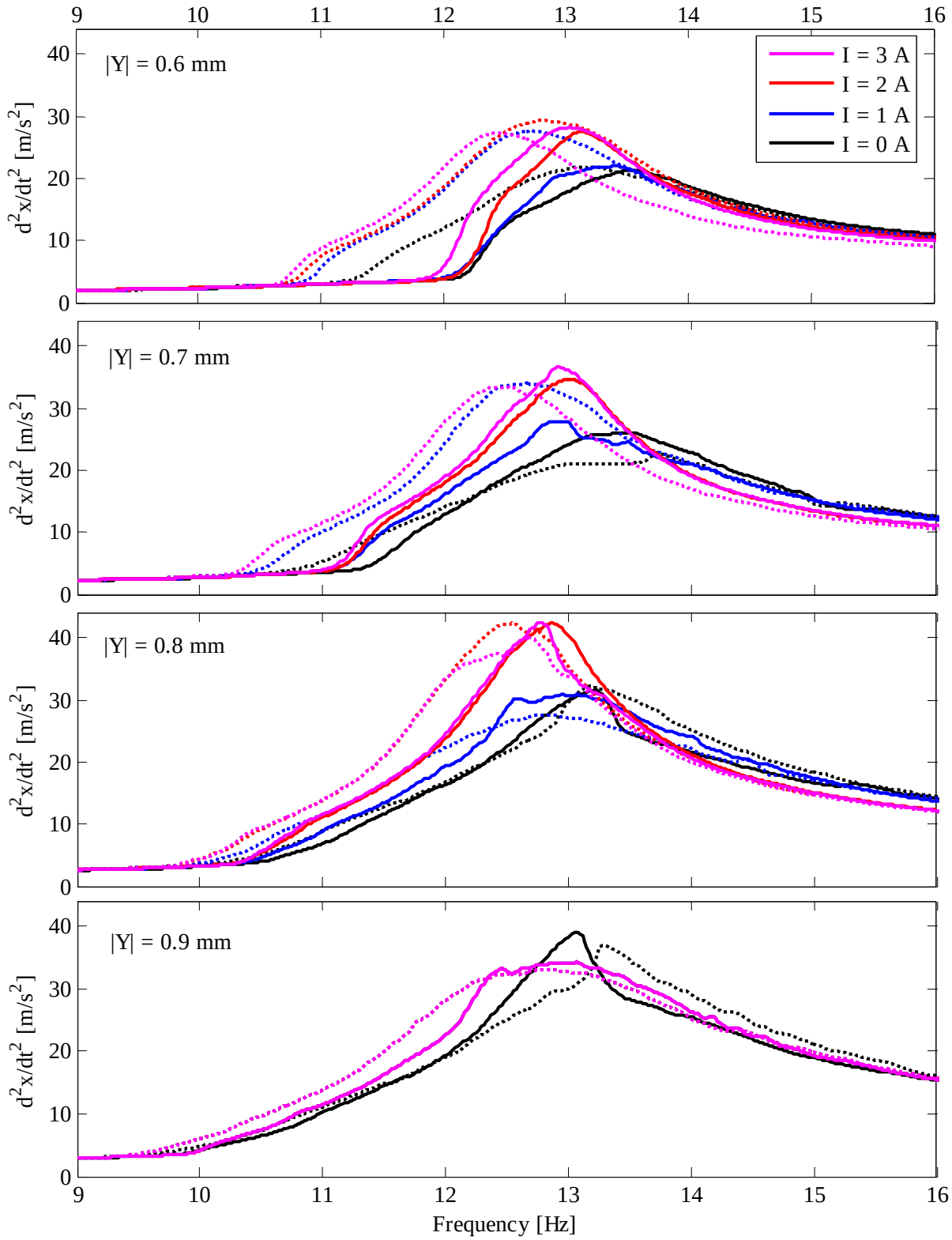

Figure 5-16: MR bushing base excitation mass acceleration results generated with the 31.3 kg mass and using the brass bearings (solid – forward sweep, dotted – backward sweep).

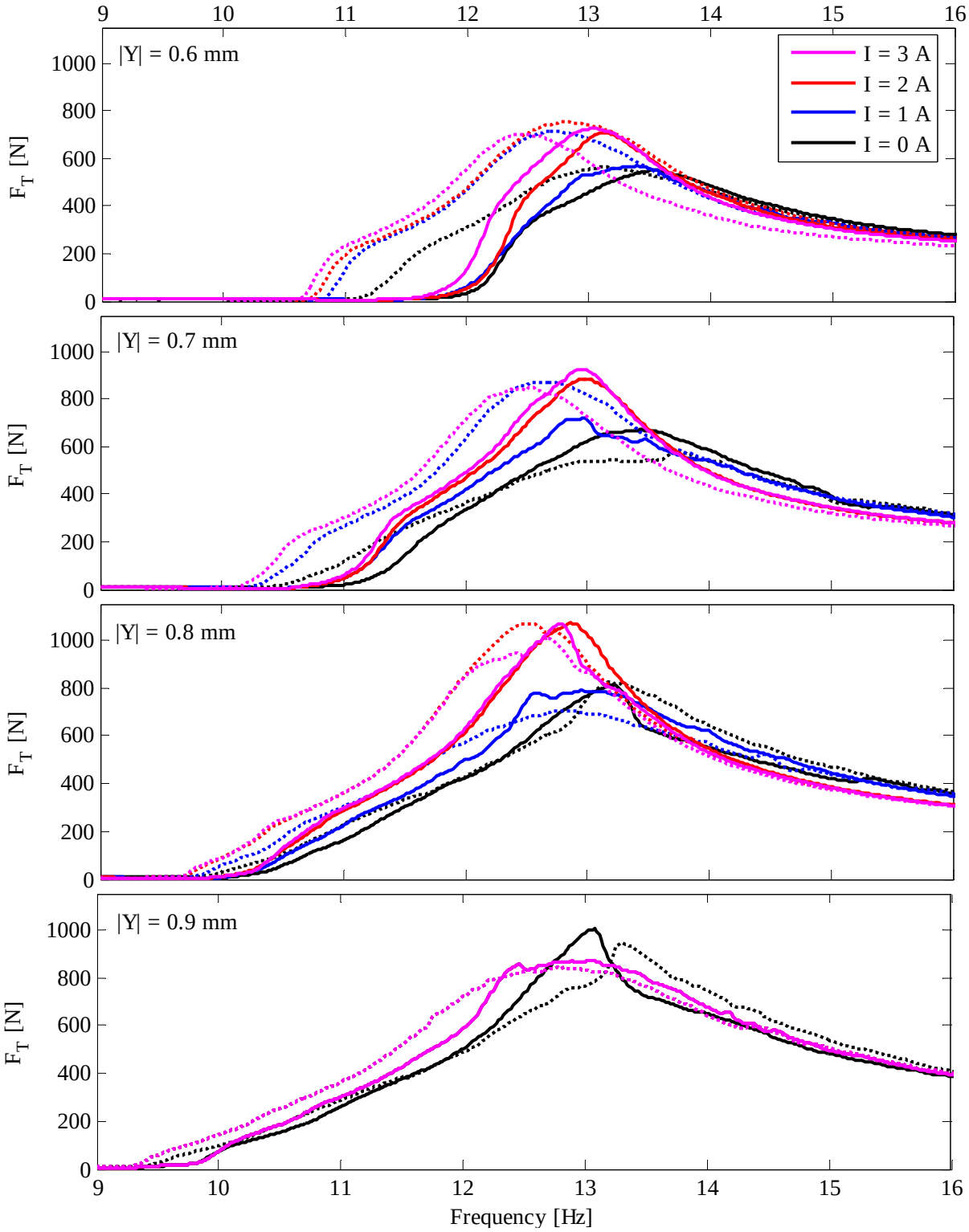

Figure 5-17: MR bushing base excitation transferred force results generated with the 31.3 kg mass and using the brass bearings (solid – forward sweep, dotted – backward sweep).

5.3 Summary

In section 5.2, the theoretical RMS optimization results are shown to be applicable to a real system. Base excitation and rotating unbalance input experiment results show that the minimum of the RMS of absolute acceleration and force transmitted occur at similar damping ratios. These two theoretical results are verified with a single experiment as described in Chapter 4. The experiment results also verify the harmonic forcing RMS optimization curves.

Base excitation experiment results are shown for the purchased bushing, as well as the prototype MR bushing. The performance of the two hydraulic bushings (P/N 90576090 and 90575028) are compared by examining the static stiffness of the rubber as well as the dynamic stiffness. The static stiffness is found to be very similar. The dynamic stiffness is also quite similar and the difference in performance is attributed to the poor dynamic stiffness testing facilities used for bushing P/N 90575028; otherwise, the results show that the bushings are very similar.

Finally, the first and second attempts at producing MR bushing results yield the same performance despite improvement to the MR valve in the second trial. The MR bushing has a relatively small effect on the performance of the base excitation system. It is found that as the current input increases the peak acceleration and displacement also increase. These frequencies of the peaks also shift down by approximately 10% over the full variation of current. This is explained by the decrease in damping associated with the decrease in fluid flowing through the inertia track when the valve is functioning, as per the MR dynamic stiffness simulation results shown in Chapter 3.

Chapter 6
Conclusions and Future Work

The purpose of this thesis is to investigate the application of MR technology in the area of engine isolation. Semi-active engine hydraulic bushings are required to meet new performance requirements associated with cylinder deactivation engines. When the engine control unit (ECU) changes the number of cylinders firing the magnitude of the forcing changes requiring different bushing properties. Also, transient vibrations resulting from torsional loading during the process of activating and deactivation cylinders need to be better controlled with a MR bushing.

6.1 RMS Optimization

The design of engine isolators in general has been approached by examining the frequency response of three fundamental inputs which represent the basic inputs experienced in a vehicle: base excitation from the body or chassis, unbalance forces from the rotating engine components, and harmonic forcing representing the engine combustion forces. Previous researchers found that plotting the RMS acceleration versus RMS displacement of a single DoF oscillator under base excitation for a given stiffness reveals that there exists an optimum damping ratio which minimizes the RMS acceleration. This result was verified experimentally in Chapter 5 of this thesis. It is also documented previously (Section 2.1.2) that adding negative cubic stiffness to a linear oscillator greatly improves the performance in the frequency domain. Cubic damping was found to have very little positive effect on the frequency response relative to cubic stiffness.

Similar to the base excitation optimization study, harmonic forcing and rotating unbalance forcing each were found to have a damping ratio for a given stiffness which would yield a minimum RMS transmitted force. This result was also confirmed experimentally. It is important to note that the base excitation and rotating unbalance systems have common optimum points. Furthermore, cubic damping had little effect on the forced frequency response of the isolator whereas negative cubic

stiffness was found to greatly improve the isolation of harmonic forcing inputs as was found in the base excitation case mentioned above.

The time domain response of the cubic nonlinear system also demonstrated some interesting behavior. While the cubic damping and especially the cubic stiffness were found to have large influence on the frequency response they seemed to have negligible effect on the response to step and impulse inputs as illustrated by the numerical simulation results. The time domain response appears to be dominated by the linear stiffness and damping. This property of slightly cubic nonlinear is not confirmed experimentally; however it suggest that linear stiffness and damping coefficients can be selected to provide optimal time domain response and small amounts of cubic stiffness could be added to improve the frequency response (or steady state performance).

The progress made in area of linear optimization shows how optimum semi-active damping ratios could selected based on the dominance of the input – being either predominantly base excitation, unbalance, or harmonic forcing. Of course, semi-active control is not possible without some ability to sense these states either using accelerometers installed on the bushing, feedback from the ECU, or possibly even tracking the vehicle driver inputs to estimate the vibration conditions under the hood. The cubic nonlinear RMS study shows how feedback could be used to create controlled nonlinearity in a semi-active system and greatly improve performance.

Most importantly, the RMS optimization technique was applied to the design of hydraulic bushings. For a specific case with assumed effective engine mass the RMS optimization of the bushing revealed that the inertia track length of the bushing under study could be tuned (a 20 % decrease in length) to improve the RMS acceleration by approximately 4.4 % and RMS displacement by 5.1 % under base excitations. Also, this tuning of the inertia track would decrease RMS force transmitted by 12 % with a marginal increase in RMS displacement of the engine of 0.7 % in the case of harmonic forcing. Further study is needed to investigate whether this is a practical way to design hydraulic engine bushings.

6.2 MR Bushing

The first step to designing a semi-active hydraulic bushing was to fully investigate the performance and properties of a standard hydraulic bushing. Fortunately, hydraulic bushings are very similar to the commonly documented hydraulic engine mount. This aspect simplified the mathematical modeling of the bushing. The bushing parameters were identified by using various experimental results along with curve fitting algorithms. The resulting mathematical model closely approximated the dynamic stiffness of the bushing for two different amplitudes of vibration assuming that only the fluid resistance changes due to nonlinearity.

A MR valve was designed using a novel highly efficient valve design. This valve was implemented on a current hydraulic bushing. The dynamic stiffness of the MR bushing was simulated numerically using the previously obtained model of the bushing along with the known MR fluid parameters and valve dimensions. This study illustrated that sending current to the valve tended to decrease the amount of damping (by decreasing inertia track flow) and effectively increasing the low frequency dynamic stiffness. The limiting case was found to be when flow was completely choked by the MR valve and the bushing behaved as a single DoF isolator. It is suggested that to improve the bandwidth of the MR bushing the off-state notch frequencies could be increased as illustrated in Figure 6-1. Future studies may investigate this option.

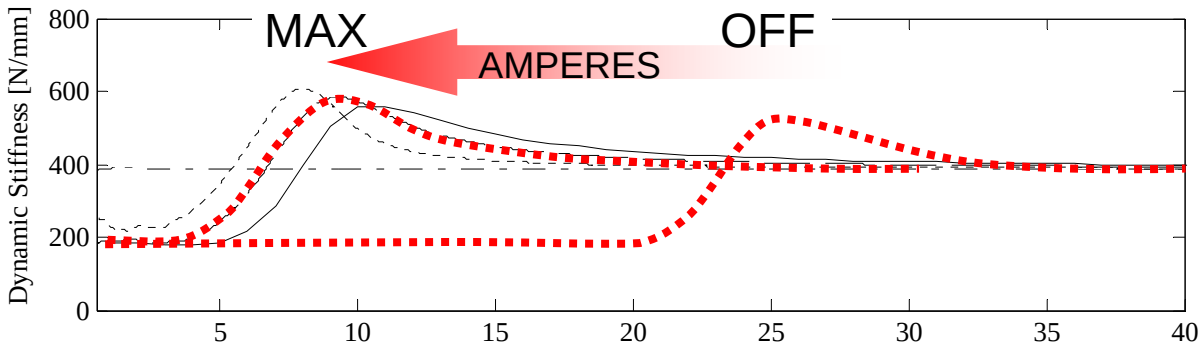

Figure 6-1: Increase of the off-state notch frequency to improve the bandwidth of the MR bushing

Base excitation experiment results using the MR valve illustrate that although the valve appears to be working it has a marginal effect on the acceleration and displacement frequency response. The results agree with the dynamic stiffness simulation result in that the peak response increases in magnitude and occurs at lower frequency as the bushing damping decreases with increasing valve current. Unfortunately, MR bushing dynamic stiffness results could not be generated on the experimental apparatus due to the poor rigidity of the electromagnetic shaker frame. This represents another opportunity for future experimental work.

The integration of the MR device with the hydraulic bushing still requires some development. However, one proposed method is illustrated in Figure 6-2. It is otherwise quite difficult to implement an MR device without consuming additional valuable engine compartment volume.

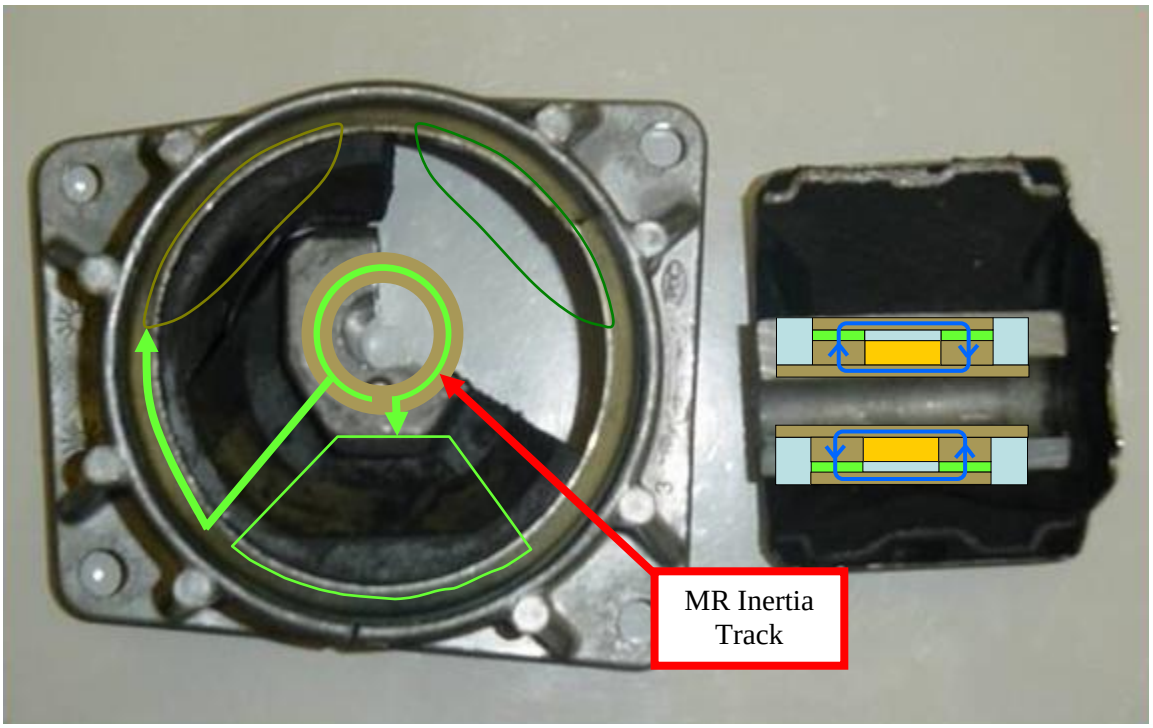

Figure 6-2: Potential implementation of MR valve in a production hydraulic bushing.

Following up on the suggestions presented here will present clear direction for the future of MR hydraulic bushings. Future design work may require more rigorous study of the electromagnetics involved, perhaps using finite element methods to develop the performance of the device. Also, more

detailed mechanical design work is also required to move the existing MR valve design from the prototype to production phase.

If future work finds that the MR valve does not meet the requirements of the cylinder deactivation application it is shown that increasing the compliance of the pumping chamber of the bushing by a factor of 4 could reduce the dynamic stiffness by approximately 50%. This could possibly be achieved by implementing a MR valve used to connect the pumping chamber to a much more compliant chamber. This concept is essentially an active decoupler, where the passive decoupler is found in the common hydraulic engine mount as described in Chapter 2. Note that this application of MR fluid would require a MR valve which is quite different from the valve presented in this work.

However, it should also be noted that since a valve would be required to be normally open (with no current) in this alternative design the bushing would be permanently soft in the event of failure. This is shown to result in extremely high amplitudes of vibration. This effect may also cause this bushing design to consume relatively high amounts of power if the hard, or valve closed, state is the predominant state.

Bibliography

Alkhatib, R., Jazar, G.N., & Golnaraghi, M.F. (2004, August 23). Optimal design of passive linear suspension using genetic algorithm. Journal of Sound and Vibration, 275(3-5), 665-691.

Ahn, Y.K., Ahmadian, M., & Morishita, S. (1999). On the Design and Development of a Magneto-Rheological Mount. Vehicle System Dynamics, 32, 199-216.

Ahmadian, M., & Ahn, Y.K. (1999, March). Performance Analysis of Magneto-Rheological Mounts, Journal of Intelligent Material Systems and Structures, 10, 248-256.

Andrews, F. J. (2002, January). A primer on vibration isolation. Sound and Vibration, 36(1), 42-46.

Ashley, S. (2004, December). Firing on half-cylinders. Scientific American, 291(6), 20-22.

Askeland, D.R. (1996). The Science and Engineering of Materials (3rd S.I. ed.). London: Chapman and Hall.

Baudendistel, T.A., Tewani, S.G., Shores, J.M., Long, M.W., Longhouse, R.E., Namuduri, C.S., & Alexandridis, A.A. (2002). Hydraulic mount with magnetorheological fluid. US Patent 0171186.

Carlson, D.J., Chrzan, M.J., & James, F.O. (1994). Magnetorheological fluid devices. US Patent 5284330.

Choi, S.B., Lee, H.H., Song, H.J., & Park, J.-S. (2002). Vibration Control of a Passenger Car Using MR Engine Mounts. Smart Structures and Material, 4701, 1-8.

Choi, S.B., Song, H.J., Lee, H.H., Lim, S.C., & Kim, H.J. (2003). Vibration control of a passenger vehicle featuring magnetorheological engine mounts. International Journal of Vehicle Design, 33(1-3), 2-16.

Colgate, J.E., Chang, C.-T., Chiou, Y.-C., Liu, W.K., & Keer, L.M. (1995, July 20). Modelling of a hydraulic engine mount focusing on response to sinusoidal and composite excitations. Journal of Sound and Vibration, 184(3), 503-528.

Flower, W.C. (1985). Understanding Hydraulic Mounts for Improved Vehicle Noise, Vibration and Ride Qualities. Surface Vehicle Noise and Vibration Conference Proceedings (pp. 123-132). Traverse City, MI: Society of Automotive Engineers.

Foumani, M.S., Khajepour, A., & Durali, M. (2004). A New High-Performance Adaptive Engine Mount. Journal of Vibration and Control, 10(1), 39-54.

Geisberger, A.A. (2000). Hydraulic Engine Mount Modeling, Parameter Identification and Experimental Validation (MASc. Thesis). Waterloo, ON, CA: University of Waterloo.

Geisberger, A., Khajepour, A., Golnaraghi, F. (2002, January 10). Non-linear modelling of hydraulic mounts: Theory and experiment. Journal of Sound and Vibration, 249(2), 371-397.

Golnaraghi, M.F., & Jazar, G.N. (2001, May). Development and analysis of a simplified nonlinear model of a hydraulic engine mount. Journal of Vibration and Control, 7(4), 495-526.

Golnaraghi, M.F., & Jazar, N.G. (2002). Nonlinear modeling, experimental verification, and theoretical analysis of a hydraulic engine mount. Journal of Vibration and Control, 8(1), 87-116.

Gorodkin, S., Lukianovich, A., & Kordonski, W. (1998, August). Magnetorheological Throttle Valve in Passive Damping Systems. Journal of Intelligent Material Systems and Structures, 9.

Halliday, D., Resnick, R., & Walker, J. (1997). Fundamentals of Physics: Extended (5^{th} ed.). New York: John Wiley and Sons Inc..

Hardie, C., Tait, H., Craig, S., Chase, J.G., Smith, B.W., & Harris, G. (2002). Automated tuning of an engine management unit for an automotive engine. Journal of Automobile Engineering, 216(10), 841-849.

Hong, S.R., Choi, S.B., Jung, W.J., Ham, I.B., & Kim, D.K. (2001). Vibration of an ER Mount Subjected to High Static Loads. Journal of Sound and Vibration, 242(4), 740-748.

Inman, D. J. (2001). Engineering vibration, (2nd ed.). Upper Saddle River, N.J.:Prentice Hall.

Jackson, M.D., & Jones, P. (1976, August 2). Deactivating Compressor-Engine Cylinders Saves Fuel. Oil and Gas Journal, 74(31), 130-133.

Jazar, G.N., & Golnaraghi, M.F. (2002, September). Engine Mounts for Automotive Applications: A Survey. The Shock and Vibration Digest, 34(5), 363-379.

Jazar, G.N., Narimani, A., Golnaraghi, M.F., & Swanson, D.A. (2003). Practical Frequency and Time Optimal Design of Passive Linear Vibration Isolation Mounts. Vehicle System Dynamics, 39(6), 437-466.

Kim, G., & Singh, R. (1993, September). Nonlinear analysis of automotive hydraulic engine mount. Journal of Dynamic Systems, Measurement and Control, Transactions of the ASME, 115(3), 482-487.

Kim, G., & Singh, R. (1995, January 19). Study of passive and adaptive hydraulic engine mount systems with emphasis on non-linear characteristics. Journal of Sound and Vibration, 179(3), 427-453.

Kordonsky, W.I., Gorodkin, S.R., Kolomentsev, A.V., Kuzmin, V.A., Luk'ianovich, A.V., Protasevich, N.A., Prokhorov, I.V., & Zinovii, P.S. (1995). Magnetorheological valve and devices incorporation magnetorheological elements. US Patent 5452745.

Kuzhir, P., Bossis, G., & Bashtovoi, V. (2003, November/December). Effect of the orientation of the magnetic field on the flow of a magnetorheological fluid. I. Plane channel. Journal of Rheology, 47(6), 1373-1384.

Kuzhir, P., Bossis, G., Bashtovoi, V., & Volkova, O. (2003, November/December). Effect of the orientation of the magnetic field on the flow of magnetorheological fluid. II. Cylindrical channel. Journal of Rheology, 47(6), 1385-1398

Lee, Y.-W., & Lee, C.-W. (2002). Dynamic analysis and control of an active engine mount system. Proceedings of the Institution of Mechanical Engineers, Part D: Journal of Automobile Engineering (pp. 921-931), 216(11). Professional Engineering Publishing.

Lin, Y., Luo, W., & Zhang, Y.M. (1990, July). New method for the optimization of a vibration isolation system. Journal of Vibration, Acoustics, Stress, and Reliability in Design, 112,(3), 413-416.

Lord Corporation. (1999). Engineering Note: Designing with MR Fluids, Materials Division (rev. 12).

Madjlesi, R., Schubert, B., Khajepour, A., & Ismail, F. (2003). A new approach in mounting systems optimization. American Society of Mechanical Engineers, Dynamic Systems and Control Division (Publication) DSC, 72(2), 963-970.

Matsuoka, H., Mikasa, T., Nemoto, H., & Gehm, R. (Ed.) (2004, September). Bringing down the noise. Automotive Engineering International, 112(9), 83-87.

Muller, M., Weltin, U., Law, D., Roberts, M.M., & Siebler, T.W. (1994, July). Engine mounts and NVH. Automotive Engineering, 102(7), 19-23.

Narimani, A. (2004). Development of Linear and Nonlinear Isolation Techniques for passive and Semi-Active Application (Ph.D. Dissertation). Waterloo, ON, CA: University of Waterloo.

Narimani, A., & Golnaraghi, M. F. (2004). Nonlinear Isolator Optimization Using RMS Cost Function. International Mechanical Engineering Congress and R&D Expo (Paper No IMECE2004-61314). Anaheim, California: ASME.

Narimani, A., Golnaraghi, M.F., & Jazar, G. N. (2004, February). Sensitivity analysis of the frequency response of a piecewise linear system in a frequency island. Journal of Vibration and Control, 10(2), 175-198.

Nayfeh, A. H. (1981). Introduction to perturbation techniques. New York: Wiley.

Nayfeh, A. H., & Mook, D.T. (1979). Nonlinear Oscillations. New York: Wiley.

Nayfeh, T.A., Emaci, E., & Vakakis, A.F. (1997, August). Application of nonlinear localization to the optimization of a vibration isolation system. AIAA Journal, 35(8), 1378-1386.

Oueini, S.S., Chin, C.-M., & Nayfeh, A.H. (1999, November). Dynamics of a cubic nonlinear vibration absorber. Nonlinear Dynamics, 20(3), 283-295.

Rao, S. S. (2004). Mechanical vibrations (4th ed.). Upper Saddle River, N.J.: Pearson Prentice Hall.

Singh, R., Kim, G., & Ravindra, P.V. (1992). Linear Analysis of Automotive Hydro-Mechanical Mount with Emphasis on Decouple Characteristics. Journal of Sound and Vibrations, 158(2), 219-243.

Shtarkmen, E.M. (1993). Vehicle engine mount. US Patent 5176368.

Vahdati, N., & Ahmadian, M. (2003). Single pumper semi-active fluid mount. Proceedings of the 2003 ASME International Mechanical Engineering Congress (pp. 167-175), 72(1). Washington, DC: American Society of Mechanical Engineers.

Vakakis, A.F., McFarland, D. M., Bergman, L., Manevitch, L., & Gendelman, O. (2003). Passive vibration control through nonlinear energy pumping. Proceedings of the ASME Design

Engineering Technical Conference (pp. 1883-1888), 5. Chicago, IL: American Society of Mechanical Engineers.

Williams, E.W., Rigby, S.G., Sproston, J.L., & Stanway, R. (1993, June). Electrorheological fluids applied to an automotive engine mount. Journal of Non-Newtonian Fluid Mechanics, 47, 221-238.